Effects of Sand Ingestion on the Cooling of Turbine Blade Outer Air Seals

Camron C. Land

Thesis submitted to the faculty of the
Virginia Polytechnic Institute and State University
in partial fulfillment of the requirements for the degree of

Master of Science
in
Mechanical Engineering

Dr. Karen A. Thole, Chair
Dr. Wing F. Ng
Dr. Pavlos P. Vlachos

November 24, 2006
Blacksburg, VA

Keywords: sand ingestion, gas turbine,
impingement, film-cooling

Effects of Sand Ingestion on the Cooling of Turbine Blade Outer Air Seals

Camron C. Land

Abstract

Modern gas turbine engines operate in environments where particle ingestion, especially sand ingestion, can affect the cooling of various turbine parts. The most critical areas are in the combustor and the first stage components of the turbine. Gas temperatures in these areas are the highest compared to other areas and exceed the melting points of the constituent metals. To extend the life of hot section components, internal convective cooling and external film-cooling are required. This study examined the effects of sand ingestion on various cooling geometries. The first part investigated impingement and film-cooling implemented in a double-walled cooling geometry for the purpose of reducing sand size and thereby reducing blockage due to sand ingestion. The second part analyzed the cooling performance of actual turbine blade outer air seals injected with sand.

Results from these studies showed areas of impingement that promote particle fragmentation are advantageous in reducing particle size and reducing blockage due to particle ingestion. Blockage was significantly increased based on the percentage of large particles present in the sand samples. Increasing the pressure ratio and decreasing the sand amount were also shown to reduce blockage.

Preface

Gas turbine engines installed on aircraft are most often exposed to environments containing fine particles such as sand, ash, and dirt during takeoffs and landings. Sufficient cooling of hot section components is critical during these intervals of engine operation. Particle ingestion can block the cooling passages and reduce the coolant flow leading to possible part failure. Previous studies on sand ingestion in cooling passages focused on sand blockage in the cooling passages of turbine blades and also in a simple array of laser-drilled film-cooling holes at room temperatures and at engine temperatures.

The first part of this thesis is a paper that examined sand ingestion in a double-walled liner containing impingement and film-cooling holes. The methodology and parameters for determining the effects of sand ingestion in the double-walled coupon are described. Also presented are the results of the testing performed to determine the amount of flow blockage due to sand for a range of conditions.

The second part of this thesis is a final contract report to be submitted to the sponsor of this work, Pratt & Whitney. The methodology and parameters for determining the effects of sand ingestion in actual blade outer air seals are discussed. The blade outer air seals tested included two V2500 BOAS parts with conventional impingement and film-cooling geometries and a BOAS with two new microcircuit cooling geometries referred to as brick-and-mortar and pedestal. The results of testing on these different BOAS geometries allowed for a comparison of their performance by determining the amount of flow blockage due to sand for a range of conditions.

Acknowledgements

There are many people who have been integral in my life to this point. First and foremost I would like to thank God for sending my Lord and Savior Jesus Christ to Earth to die on the cross and rise again for my sins. I can do everything through Him who gives me strength (Phl. 4:13, NIV). I would like to thank my wife, Katie, for being the love of my life and being by my side for most of this educational journey. I look forward to spending the rest of my life with her. I would like to thank Mom and Dad for supporting me in everything I have ever done. There have been many times over the years when I was not following the right path, and they have never abandoned me. Special thanks go out to my sisters, Ashley and Jenine. They always believed in me and knew I could do great things, and I know they are doing great things also. I would like to thank all of my extended family including Katie's family for all the great times and great times to come. I love you all.

I would like to thank my adviser and mentor, Karen, for everything she has done for me. It has not always been a smooth experience, but I believe I am a better person and engineer for having the privilege of working with her. I wish her the best in all her endeavors. Thank you to all the people in the VTExCCL lab for the wonderful friendships and great memories of my time here at Virginia Tech. Thanks to the extended network of friends also. Finally, I would like to thank my bible study groups and church, Northstar Church, for their continued support and prayer.

This is not an ending but a continuation. As my Cavalier sister would say paraphrasing Thomas Jefferson, "Learning never ends." As my Hokie Dad and sister would say, "Carruthers, Chaz, Mitzy, and Buffy sure have some funny traditions up there in Charlottesville." Fight On Trojans, and Let's Go Hokies!

Table of Contents

List of Tables

List of Figures

Part I:

Considerations of a Double-Wall Cooling Design to Reduce Sand Blockage*

Abstract

Gas turbine engines in use today use innovative cooling techniques to keep metal temperatures down while pushing the main gas temperature as high as possible. Cooling technologies such as film-cooling and impingement cooling are generally used to reduce metal temperatures of the various components in the combustor and turbine sections. As cooling passages become more complicated, ingested particles, especially sand, can block these passages and greatly reduce the life of hot section components.

This study investigates a double-walled cooling geometry with impingement and film-cooling. A number of parameters were simulated to investigate the success of using impingement jets to reduce the size of particles in the cooling passages. Pressure ratios typically ranged between those used for combustor liner cooling and for blade outer air seal cooling whereby both these locations typically use double-walled liners. The results obtained in this study are applicable to more intricate geometries where the need to promote particle break-up exists. Results indicated that ingested sand had a large distribution of particle sizes where particles greater than 150 μm in diameter are primarily responsible for blocking the cooling passages. Results also showed that the blockage from these large particles was significantly influenced and can be significantly reduced by controlling the spacing between the film-cooling and impingement cooling plates.

*Co-authors: Dr. Karen A. Thole, Department of Mechanical and Nuclear Engineering, Penn State
Chris Joe, Advanced Military Turbines CIPT, Pratt & Whitney

Introduction

Gas turbine engines installed on aircraft are increasingly exposed to environments containing fine particles such as sand, ash, and dirt. When these fine particles are ingested into the engine, they can cause many problems at various locations within the engine. Most damage occurs during takeoff and landing at which time large amounts of particles can be ingested over short periods of time when engines are running at or near full power. Sand and other particles on the runway can be entrained into the inlet supplying the engine with its flow. Hamed et al. [1] reported that the formation of an unsteady vortex in front of the engine intake on the runway can entrain sand, dust, ice, and other particles into the engine. The possibility also exists for particles to be ingested at cruising altitude, which was further investigated in studies performed by Kim et al. [2] on aircraft flying through volcanic dust clouds.

Cooling air that flows through parts in the hot section of the turbine engine originates from the last stage of the compressor. The compressor bleed air is used to keep metal temperatures at acceptable levels in the combustor liner, turbine vanes, turbine blades, and turbine blade outer air seals. Common cooling geometries seen in these parts employ both internal convection, such as impingement cooling, and external film-cooling. The issue is compounded by the fact that particles, such as sand, present in the compressor bleed air can block these cooling passages and holes leading to decreased part life.

Previous studies by Dunn et al. [3, 4] and Batcho et al. [5] have indicated that the effects of particle ingestion in an engine include compressor erosion, deposition of materials on hot section components, blockage of combustor fuel nozzles, and blockage of cooling holes. The study reported in this document focuses on how sand can block the cooling passages and holes in a double-walled geometry. A double-walled geometry can be found in a gas turbine in several locations including a combustor liner, turbine blade outer air seal, and inside airfoils.

Similar to the investigation reported by Walsh et al. [6], this study quantified the blockage due to sand ingestion by measuring the reduction in coolant flow through an array of cooling holes at a given pressure ratio. While the study here reports data for a double-walled geometry at room temperature conditions, Walsh et al. [6] investigated the

effects of temperature on the blocking of film-cooling holes placed in a single wall coupon with film-cooling holes. Walsh et al. [6] found that when metal temperatures increased from 882°C to 992°C, there was a minimal increase of flow blockages. When metal temperatures increased from 992°C to 1038°C, however, the flow blockage increased from 5.7% to 7.7%, representing a 2% increase.

A double-walled coupon was used in this study to simulate commonly found cooling geometries. The coupon used had an inlet plate with an array of impingement holes and an exit plate with an array of film-cooling holes. The primary research objective was to determine whether impingement could be beneficial for breaking up particles in cooling passages thereby minimizing sand blockage in the film-cooling holes. The results presented can be expanded to include guidelines for cooling geometries whereby impingement flow can promote particle fragmentation. Many conditions were investigated to confirm the effects of impinging flows including pressure ratio, sand amount, sand distribution, plate spacing, and hole alignment. This paper includes a description of the experimental facility and methodology, sand characterization, and finally the results of the testing performed to determine the amount of flow blockage due to sand for a range of conditions.

Past Relevant Studies

Particles in the main gas path can block cooling holes on the external side due to deposition. This deposition can lead to severe increases in heat transfer coefficients as well as decreased levels of film-coolant. On the internal side of the turbine components, particles can also adhere to the inner walls that lead to flow blockages of the channels as well as film-cooling holes. There are a range of influences that can be considered when investigating the blockages of sand particles in coolant channels. For example, particle fragmentation can occur when particles flow through the engine and impact surfaces, which would lead to a favorable result in terms of reduced blockages. Moreover, the ratio of the flow velocity to the particle size and density, namely given as the Stokes number, can also influence whether the particle is convected by the flow or drops out of the flow and deposits onto the surfaces.

Several studies have been performed that have examined plugging of cooling holes after particles' trajectories after having been ingested into the main gas path of an engine. Hussein and Tabakoff [7] computationally simulated flows through a turbine which showed that the number of particle impacts increased with increasing particle size. They observed that the particles flowing through the main gas path of an axial-flow turbine were reflected from the blunt leading edges of the rotor blade and the nozzle guide vane trailing edge before finally passing through the rotor. They also reported particles being affected by centrifugal forces that convected the particles toward the outer casing. The centrifugal effect was in agreement with studies by Kim et al. [2] who found that lighter particles tend to follow the flow while heavier particles tend to be centrifuged. They conducted experimental tests on volcanic ash ingestion in two different hot section test systems consisting of a combustor and a set of nozzle guide vanes. Kim et al. [2] also found that the showerhead cooling holes located at the leading edge of turbine vanes plugged with dust, which resulted in a decrease in film cooling effectiveness. Batcho et al. [5] observed partial or complete blockage of vane and blade cooling holes in aircraft engines that had been flown through dust clouds. Such plugging can result in the surface temperature of the vanes rising above their melting temperature, leading to hardware damage.

Since the cooling air for the combustor liner and turbine is bled from the last stage of the compressor, particles are continuously interacting with various engine component surfaces. This interaction can cause the particles to become smaller due to the impingement forces as the particles progress through the engine. Dunn et al. [3] performed studies to determine whether there is significant breakup of dust as it moves through the compressor of a gas turbine engine. The level of fragmentation taking place in the fan and compressor that was deduced from collecting particles downstream of the bypass and in the environmental control system was also investigated. Note that the environmental control system bleeds air from the last stage of the compressor to provide air, temperature control, and pressurization for the passengers and crew. As such, the control system air has a similar concentration of particles to that of the bleed air for cooling the combustor and turbine components. Dunn et al. [3] reported in the study that both the particles collected from the fan bypass air and from the environmental control

system were nominally the same size, but significantly smaller in size than the particles that were ingested into the engine. This finding led them to believe that most of the fragmentation occurred in the first few fan and compressor stages. Particle break up was also observed in studies by Mann et al. [8] and Tilly et al. [9], the latter of which confirmed the fragmentation behavior of irregular quartz particles during impact. Sand consists primarily of quartz particles.

It is important to make use of what is already known for the heat transfer of impingement jets since this helps in better understanding how the sand may be reacting in a double-walled liner. This knowledge also helps us to determine whether what we are suggesting, namely utilizing jet impingement for breaking up particles, will negatively influence the expected heat transfer from jet impingement. The particles that pass through the fan and compressor stages can be further broken down into smaller pieces using cooling methods that promote fragmentation. One of these methods for cooling in a turbine engine is jet impingement. According to Uysal et al. [10], the performance of impingement cooling is influenced by flow in the cross direction. The level of crossflow decreases as the spacing between the jet and impinging surfaces increases. The impingement jet, however, becomes weaker as the spacing increases, which also reduces the desired effect of high heat transfer coefficients. Therefore, a tradeoff exists between wall spacing and cooling jet performance. According to Florschuetz et al. [11] and Van Treuren et al. [12], for very narrow distances between the impingement exit and impinging surface, ($S/D_I \sim 1$), crossflow increases the heat transfer as it convects more coolant from upstream. While the double-walled coupon in the current study does not have flow exiting the geometry in the same manner, there are still crossflow effects upstream of the film cooling holes. These crossflow effects are a result of the flow impinging on the film plate surface and changing direction to exit through the film cooling holes. Furthermore, Uysal et al. [10] found the differences in heat transfer among cases with the wall spacing to hole diameter values between 0.73 and 2.2 to be small, and there was only slightly better heat transfer performance observed when $S/D_I = 1.5$. When the wall spacing is narrow, the jet failed to develop a sufficient level of turbulence for heat transfer enhancement at the impingement location. On the other

hand, jet flow with very large wall spacing dissipates excessively and does not penetrate the crossflow, which results in lower heat transfer at the impingement surface.

Ingested sand passes through many areas in an engine with the particle size varying as a result of surface impacts. The sand also blocks cooling passages both internally from the coolant bleed air and externally by deposition from the main gas path. The focus of this study is on reducing sand blockage within gas turbine engine hardware. Promoting particle breakup may achieve this result by altering cooling geometries to increase high velocity surface impacts. This study will provide engine designers knowledge about the factors affecting sand fragmentation and blockage to allow better hardware designs to be developed.

Experimental Facility and Methodology

To characterize the flow blockage in the double-walled coupon due to sand particles, the pressure ratio and cooling air flow rate were measured. The pressure ratio refers to the ratio of the supply coolant pressure to the exit static pressure, as shown in equation 1.1.

$$PR = \frac{P_{0C}}{P_{\infty}} \tag{1.1}$$

The supply coolant pressure was measured upstream of the double-walled coupon while the exit static pressure, the atmospheric pressure in the test laboratory, was measured downstream of the coupon. The coolant flow rate is reported in terms of a flow parameter defined by Hill et al. [13] and given in equation 1.2.

$$FP = \frac{4\dot{m}\sqrt{RT_{0C}}}{\pi P_{\infty} N D^2} \tag{1.2}$$

The supply coolant temperature was measured upstream of the laminar flow element and verified to be at the same total temperature measured upstream of the double-walled coupon. The flow parameter is the ratio of momentum flow rate to pressure force. If a cooling geometry was altered, the flow parameter changed. Any blockage in the double-walled test coupon caused a reduction in flow parameter. The comparison of this reduced flow parameter to the flow parameter with no blockage gave the results presented in this paper.

The combination of impingement cooling and film-cooling is a common cooling technique found in the combustor liner and the turbine blade outer air seal. Figure 1.1 shows the alignment of the impingement holes with respect to the film-cooling holes for two different configurations that were used for the test coupon. For most of the tests in this study, the impingement jets were staggered with respect to the film-cooling jets. A few tests, however, were conducted with the impingement jets aligned with the film-cooling jets to determine if using impingement was advantageous in breaking up particles.

The test coupon consisted of two plates separated by a spacer plate that fixed the distance between the impingement holes and film-cooling holes. Figure 1.2 shows the hole arrangement on both the impingement and film-cooling plates. The impingement plate contained 25 impingement holes with a diameter of 0.51 mm. The holes were made using electrical discharge machining (EDM) at 90° with respect to the surface. The impingement plate was 1.27 mm thick giving a hole length to diameter ratio of L/D_I = 2.5. The spacer plates that were used had thicknesses ranging from 0.79 mm to 3.18 mm, which allowed the spacing to diameter ratio to vary from S/D_I = 1.56 to 6.25. The second plate contained 98 film-cooling holes made using EDM with a diameter of 0.51 mm. The holes were angled at 30° with respect to the surface. The film-cooling plate was 0.89 mm thick giving a hole length to diameter ratio of L/D_F = 2.

Figure 1.3 illustrates the test apparatus for supplying air and sand to the test coupon as well as the location of the measurements made. The coolant air was supplied to the test coupon at an elevated pressure from a compressed air line at room temperature. The pressure was regulated between 2 kPa and 73 kPa. The amount of coolant was controlled by a pressure regulator and a precision control valve that both contained screens to filter any particles. The coolant flow was measured with a laminar flow element (LFE) having a maximum capacity of 0.0014 m^3/s. The laminar flow element was positioned between two pieces of pipe that extended approximately ten diameters upstream and ten diameters downstream of the LFE to ensure that fully developed flow conditions were present during testing.

The instrumentation used to conduct the experiments in this study included pressure transducers, thermocouples, an LFE, and a precision scale to weigh the sand

particles. A Type K nickel-chrome sheathed thermocouple probe was used to monitor the coolant temperature. The area ratio of the plenum cross-section to the impingement holes was sufficiently large (144:1), and therefore the pressure measurements taken inside the plenum, which was upstream of the impingement plate, were treated as the total coolant supply pressure.

Prior to performing tests with injected sand particles, baseline measurements were made to determine the flow parameter and pressure ratio under clean conditions. These baseline measurements covered the full range of possible pressure ratios that were seen during testing with sand particles. Figure 1.4 shows the baseline flow parameter versus pressure ratio for the test coupon. Testing verified that the flow parameter was the same for all spacing and hole alignments.

For the sand injection tests, a small oven was used to first dry the sand at 150°C for a time period of at least four hours to remove any lab humidity effects. Following this drying process, the coolant flow rate to the coupon was set using the precision control valves shown in Figure 1.3. Having reached the desired pressure ratio, the flow parameter was determined and compared to the baseline flow parameter. If the flow did not match the expected flow, it was most likely that there was sand remaining in the coupon from the previous test. If the expected flow was not achieved, the coupon was disassembled and cleaned using compressed air or by passing a small wire through the cooling holes. This process was continued until the baseline flow parameter was achieved for the given pressure ratio.

After successfully cleaning the coupon and setting the desired pressure ratio, the sand was removed from the oven, weighed, and loaded into the airtight section of pipe with the shutoff valve at the sand feed (refer to Figure 1.3). The sand remained in the hot oven until immediately before each test, but it returned to room temperature prior to releasing it into the coupon for testing. The amount of sand selected to flow through the test coupon corresponded to the amount of sand needed to simulate flow blockage levels that occurred in actual engine components. With steady flow conditions achieved, the feed valve was opened to introduce the sand into the coolant flow stream. The sand then flowed through the test coupon in a very short time period being on the order of a couple of seconds. The flow rate and pressure ratio were then again recorded. As a result of the

sand injection, the rate of flow passing through the coupon decreased and the pressure upstream of the test coupon increased as shown in Figure 1.5. Also seen in Figure 1.5 was that after blockage was achieved, it remained steady over time. The percent reduction in flow parameter, %RFP, was then calculated using equation 1.3.

$$\%RFP = \left| \frac{FP_0 - FP}{FP_0} \right|_{PR} \tag{1.3}$$

It is also interesting to note that testing indicated the same blockage results for the same cumulative sand amount. In other words, testing was done by dividing up the total amount of sand into three portions and comparing that with the total amount of sand for one test. The results from cumulatively adding the sand or by injecting the total amount of sand at one time resulted in the same blockage levels.

Uncertainty Analysis

For all of the results presented in this paper, three tests were conducted with the average of these three tests reported as the final value. Using three tests was determined previously by Walsh et al. [6] to give reasonable repeatability of 6.9%. Figure 1.6 shows the baseline flow parameter with the three resulting flow parameters following the introduction of sand for a set of tests. The uncertainty associated with the parameters discussed in this study was estimated using the partial derivative propagation of uncertainty method of Kline et al. [14]. The results of performing the uncertainty calculations are shown in Table 1.1.

The uncertainties were at a given pressure ratio for a low and high value of %RFP. The pressure ratio uncertainties were relatively low and were dominated by the bias uncertainty of the pressure transducer detecting the plenum pressure upstream of the test coupon. The uncertainties of the flow parameter and percent reduction in flow parameter were heavily influenced by the bias uncertainty of the pressure transducer measuring the total pressure directly upstream of the laminar flow element. The uncertainty of the amount of sand injected into the flow was directly dependent on the accuracy of the scale used to weigh the sand. For most tests the amount of sand used was 0.35 ± 0.001g. The higher the value of %RFP was, the lower the percent uncertainty.

Sand Characterization

Many different types of sand were initially tested to determine the effects of sand on blockage in the double-walled test coupon. In the study by Walsh et al. [6], ISO (International Standards Organization) fine test dust and ISO coarse test dust were used to determine flow blockage in a leading edge coupon with an array of film-cooling holes having a diameter of 0.38 mm. Tests performed on the double-walled liner in the current study utilized the same sand from the Walsh et al. [6] study resulting in negligible blockage. The ISO fine sand contained no particles with a diameter over 150 μm, and the ISO coarse sand contained at most 2% of particles over 150 μm by volume.

The sand chosen for the current study was provided by the industry sponsor and was similar to the ISO sands with the exception of a few major differences. The ISO sands did not agglomerate as did the sand used for this study. The range of particles in our sand, including agglomerations, was larger than the range of particles in the ISO sands. Figure 1.7 shows the results of three different sand characterization methods used to determine the percentage of particles in a sample that are below a given sand diameter. With a small applied force, almost all particles over 150 μm could be broken down into smaller particles. Note that these studies used non-sieved and sieved sand samples whereby the sieved sand contained only particles over 150 μm. Tests were specifically conducted with sieved sand to determine the effects of larger particles on blockage.

A Horiba Partica LA-950 laser diffraction analyzer was originally used to characterize the sand, but difficulties emerged from this wet method because the method itself caused a breaking down of particles prior to analysis. The analyzer used a combination of liquid dispersant, circulation, and agitation to inspect the particles, which all caused the sand to reduce to a base size and was not consistent with what entered the test coupon.

The sand was also measured using newer technology in particle size analysis which does not use liquid as the dispersing fluid. The new technology was released as an accessory for the Horiba Partica LA-950 called the Powderjet Dry Feeder. The particles of interest were dropped through a similar measurement cell as the wet method using a vibratory feeder, which used air and a vacuum to disperse the sand. In the wet method, the liquid dispersant was assumed to cause the majority of the sand to break up, so the

dry method was attempted to obtain a more accurate characterization. Unfortunately, the dry method also resulted in the breakdown of particles, and the characterization analysis again did not accurately describe the size of sand particles reaching the test coupon.

Finally, a simple sieve analysis was performed to accurately determine the range of sand particle diameters during testing. The sieve analyses gave the size distribution by using a range of sieves to separate the particles. The separated particles were then weighed and the fraction of particles for a particle diameter range was then calculated based on the weight of a particular sample size. The results of the sieve analysis are shown in Figure 1.7 by percent of particles under the corresponding diameter. Sieves with mesh sizes ranging from 53 μm to 850 μm were stacked in descending order with the largest sieve at the top. Then a sample of sand was weighed and loaded into the top sieve in the stack. The stack was agitated until the sand grains remained in the sieve corresponding to the grains' sizes. The sand present in each sieve was then weighed as well as the sand that passed through all of the sieves. Using the total sample weight, a percentage was calculated from the amount of sand in a single sieve compared to the total. Particles as large as 3800 microns were measured with calipers. This sieve method provided what we believed to be the most accurate characterization of the sand distribution.

Discussion of Results

The goal of this study was to determine an optimal wall spacing to minimize sand blockage in the double-walled test coupon. Many different parameters were investigated including sand amount (weight), sand size, wall spacing, hole alignment, and pressure ratio to determine their relative importance in affecting sand blockage. The results from performing this investigation are now discussed.

Variation of Sand Amount

For the double-walled test coupon, varying amounts of non-sieved sand were injected into the coolant upstream of the test coupon at varying pressure ratios. Within a modern gas turbine engine, pressure ratios below 1.1 are typically available for injecting coolant through the combustor liner. Pressure ratios above 1.1 are typically available for

cooling the first stage turbine blades and outer air seals. Figure 1.8 shows the effect of varying the amount of sand for the case with a staggered hole alignment, a wall spacing of $S/D_I = 3.13$, and non-sieved sand at the full range of pressure ratios. Based on testing with actual engine parts injected with various amounts of sand, a low, medium, and high sand amount by weight were selected. The medium sand amount of 0.35 grams produced results closest to actual part tests performed in congruence with this study.

The results showed that the blockage increased for pressure ratios from 1.02 to 1.1 and then decreased for pressure ratios of 1.1 to 1.7. From examinations of the test coupon, blockage mostly occurred in the impingement holes for pressure ratios below 1.1 leading to the conclusion that the air flow was too low to carry the sand through the coupon and the impingement plate acted as a filter. At pressure ratios above 1.1, it is believed that the sand was entrained in the flow through the impingement holes and caused most of the blockage in the film-cooling holes. Increasing the pressure ratio increased the velocity of the impingement jets on the upstream side of the film-cooling plate and therefore promoted particle fragmentation, which led to lower percent reductions in flow parameter. Figure 1.9 indicates that the percent reduction in flow parameter increased for increasing sand amounts, which was expected. Having verified the effects of varying sand amounts, the medium sand amount was injected for the remainder of the results to follow.

Variation of Sand Diameter Distribution

Sand having different size distributions, as was shown in Figure 1.7, was injected into the coolant upstream of the test coupon at varying pressure ratios. Figure 1.10 shows the effect of varying the sand distribution for the case where 0.35 grams of sand were injected at the full range of pressure ratios into a staggered test coupon. The non-sieved sand in Figure 1.7 contained the full range of sand diameters. The sieved sand sample was produced by passing the sand through a sieve and contained only particles larger than 150 μm. The sieved sand sample caused blockage as high as 80%. The non-sieved sand contained a small percentage of particles above 150 μm in diameter, so there was some blockage with those sand samples. The blockage greatly increased from the sample that had only particles above 150 μm in diameter. For the remaining results presented in this

paper, only the sand with particle diameters over 150 μm was used in testing. The dramatic increase in blockage using this sand led to focusing on the larger sand particles.

Also shown in Figure 1.10 are the results from testing with only the film plate using sieved sand at the full range of pressure ratios. The impingement plate was removed for these tests to observe the effects of the sieved sand without impingement. The results showed that the percent reduction in flow parameter increased at all pressure ratios without the impingement plate which indicates that impingement was beneficial and useful for breaking up particles.

Variation of Plate Spacing

Varying spacer thicknesses were tested for different pressure ratios. Figure 1.11 shows the effect of varying S/D_I for the case with the staggered hole alignment, sand amount of 0.35 grams, and sand with particle sizes of 150 μm and above at the full range of pressure ratios. As seen before, blockage increased for pressure ratios from 1.02 to 1.1 and then decreased for pressure ratios from 1.1 to 1.7. The S/D_I ratio of 3.13 performed considerably better than the others. The reasons for this reduced blockage at $S/D_I = 3.13$ is because the crossflow for the small plate spacings disturbed the advantageous impingement velocities that promoted particle breakup. At large plate spacings, the decreased impingement velocities at the film-cooling plate due to jet spreading caused more blockage due to jets not penetrating to the film-cooling plate.

Figure 1.12 shows the same data as in Figure 1.11 only plotted as a function of plate spacing at a given pressure ratio. A plate spacing existed that reduced the debilitating effects of crossflow and increased the beneficial effects of impingement velocity. Finding the balance between these two effects can also improve heat transfer although no heat transfer measurements were made in the course of this study. Figure 1.13 gives a picture comparison of the upstream side of the film-cooling plate at varying plate spacings. The pictures were taken for the case with a pressure ratio of 1.3, staggered hole alignment, sand amount of 0.35 grams, and sieved sand containing particles above 150 μm. Less sand appeared on the film-cooling plate for an S/D_I of 3.13 which corresponded to the settings that produced the least percent reduction in flow parameter. The location of the impingement holes with respect to the film-cooling holes

was illustrated by the absence of sand directly in the center of sets of four film-cooling holes. The reason for this is because the impingement jet is directed to that area on the film-cooling plate, and the sand is cleared away. The largest accumulations of sand occurred at spots farthest from the center of the impingement holes at the largest and smallest plate spacings meaning that the strength of the impingement jets at those spacings was lessened. The permanent discoloration between the film-cooling holes came from tests performed at engine temperatures for another study.

Variation of Hole Alignment

Varying hole alignments were analyzed for different pressure ratios and S/D_I as shown in Figure 1.1. Figure 1.14 shows the effect of varying the alignment of the holes in the impingement and film cooling plates for $S/D_I = 3.13$, 0.35 grams of sand, and sand with particle sizes of 150 μm and above, all at the full range of pressure ratios. The plate spacing of $S/D_I = 3.13$ was chosen because it outperformed the other spacings tested. The blockage followed the same trend with respect to pressure ratio as observed in every case. The staggered arrangement of holes resulted in lower reduction in flow parameter than the aligned arrangement of holes. The staggered arrangement utilized impingement to reduce the size of the sand particles and reduce blockage.

Figure 15 shows the effect of varying hole alignment for the case with PR = 1.3, 0.35 grams of sand, and sand with particle sizes of 150 μm and above for a range of plate spacings. The effects of pressure ratio were thoroughly established by the previous results, so a single PR = 1.3 was chosen to test the effects of hole alignment. Since the impingement holes were aligned with the film-cooling holes, the particle breakup due to impingement was decreased and the percent reduction in flow parameter increased. A similar trend as in the testing with the staggered arrangement was seen where the $S/D_I = 3.13$ performed better for this range of tests. The curves converge at low and high wall spacings because impingement was proven to be equally non-beneficial in breaking up particles for these cases. These results are consistent with the explanation that at large plate spacings the impingement jets fail to penetrate to the film-cooling plate due to jet spreading and at small plate spacings the impingement jets fail to penetrate to the film-

cooling plate due to crossflow. The location of the impingement holes with respect to the film-cooling holes influenced blockage less at these wall spacings.

Conclusions

Escalating turbine inlet temperatures require good cooling technologies in gas turbine engine combustors and turbines to advance. With those advancements come cooling passages that are becoming smaller and can be more susceptible to blockages from particles ingested into the engine. Sand and dust on runways, during take-off conditions, and particles present in clouds, during in-flight conditions, are the primary sources of particle ingestion for aircraft turbine engines. Blockages from these particles in these cooling passages reduces the effectiveness of cooling by decreasing the coolant flowrate, and subsequently part life can be greatly reduced. In this study a double-walled coupon, representing a generic cooling geometry with impingement holes and film-cooling holes, was tested to determine the effects of flow impingement in breaking up sand particles. Pressure ratio, sand amount, sand distribution, spacing of the double-wall, and hole alignment were all varied to test possible influences on particle fragmentation due to impingement flow.

Greater blockages in the passages were determined as the sand amount was increased to the coupon. These blockages were deduced through measured reductions in a non-dimensional flow rate for a given pressure ratio. The reductions were based on comparing the reduced flow to that of the flow that would be expected for a clean, unblocked part at the same pressure ratio.

For all of the cases that were studied, blockage levels increased as the pressure ratio increased from 1.02 to 1.1. As the pressure ratio was increased beyond 1.1, the blockage levels decreased. Examination of the coupon after each test showed that below a pressure ratio of 1.1, most of the blockage occurred on the upstream side of the impingement plate. Sand particles were essentially filtered from the coolant stream by the impingement holes and were not carried through to the film-cooling holes. Above a pressure ratio of 1.1, sand was readily carried through the impingement holes with some blockage in the impingement holes, but most of the blockage occurred on the upstream side of the film-cooling plate.

By investigating the effects of particle diameters, the concentration of particles above 150 μm had a significant effect on blockage. Sand samples containing a higher concentration of 150 μm diameters caused higher blockage than sand samples that were unfiltered and contained a full range of particle diameters. A sensitivity study was conducted on four different sand samples having different size distributions. Blockage results with two samples that contained sand with diameters less than 150 μm were negligible. The non-sieved sand, which contained a small percentage of particles with diameters greater than 150 μm, resulted in blockages that reduced the flow parameter by 5-25% while the sieved sand, containing only particles above 150 μm in diameter, resulted in blockages that reduced the flow parameter by 40-82%.

For all of the conditions considered, the spacing between the impingement and the film plates resulted in the least particle blockage for a spacing between the plates of 3.13 impingement hole diameters. Visual inspection of the coupon revealed that less sand appeared on the upstream side of the film plate for the best plate spacing compared to the other spacings for a fixed sand amount, flow condition, and hole alignment. The reason for an optimal plate spacing can be best explained by considering that as the plate spacing is small, the crossflow between the holes adversely affects the impingement process thereby not allowing particle break-ups. At large plate spacings, the strength of the impingement jets was decreased also reducing particle fragmentation of the large particle sizes and agglomerations.

The alignment of the impingement holes with respect to the film-cooling holes confirmed the beneficial effects of impingement in breaking up large particles into smaller particles. The staggered arrangement, which allowed impingement on the back side of the film-cooling plate, showed less reduction in the flow parameter relative to the aligned arrangement, where the impingement and film-cooling holes were aligned.

The results from these tests indicated that cooling geometries containing high velocity coolant jets impinging on a solid surface were helpful in breaking down particles into smaller particles. These smaller particles could then be carried through the cooling holes and exhausted into the main gas path without blocking the holes. In cooling geometries such as the double-walled liner used in this study, careful attention should be paid to the design if flow blockage due to sand ingestion is of concern.

Acknowledgements

The authors gratefully acknowledge the sponsors of this work, namely United Technologies Corporation – Pratt & Whitney.

Nomenclature

%RFP	percent reduction in flow parameter
D	diameter
FP	flow parameter
L	cooling hole length
$\dot{m}$	mass flow
N	number of impingement holes
P	pressure
PR	pressure ratio
R	gas constant for air
S	wall spacing
T	temperature

Subscripts

F	film-cooling hole
I	impingement hole
S	sand
0	baseline conditions with no sand
0C	total property of the coolant
∞	freestream conditions

References

[1] Hamed, A., Tabakoff, W., and Wenglarz, R., 2006, "Erosion and Deposition in Turbomachinery," *Journal of Propulsion and Power*, Vol. 22, No. 2, pp. 350-360.

[2] Kim, J., Dunn, M. G., Baran, A. J., Wade, D. P., and Tremba, E. L., 1993, "Deposition of Volcanic Materials in the Hot Sections of Two Gas Turbine Engines," *Journal of Engineering for Gas Turbines and Power*, Vol. 115, pp. 641-651.

[3] Dunn, M. G., Padova, C., and Adams, R. M., 1987, "Operation of Gas Turbine Engines in Dust-Laden Environments," AGARD-Advanced Technology of Aero Engine Components, Paris, France.

[4] Dunn, M. G., Padova, C., Moller, J. C., and Adams, R. M., 1987, "Performance Deterioration of a Turbofan and a Turbojet Engine Upon Exposure to a Dust Environment," *Journal of Engineering for Gas Turbines and Power*, Vol. 109, pp. 336-343.

[5] Batcho, P. F., Moller, J. C., Padova, C., and Dunn, M. G., 1987, "Interpretation of Gas Turbine Response Due to Dust Ingestion," *Journal of Engineering for Gas Turbines and Power*, Vol. 109, pp. 344-352.

[6] Walsh, W. S., Thole, K. A., and Joe, C., 2006, "Effects of Sand Ingestion on the Blockage of Film-Cooling Holes," GT2006-90067.

[7] Hussein, M. F., and Tabakoff, W., 1974, "Computation and Plotting of Solid Particle Flow in Rotating Cascades," *Computers and Fluids*, Vol. 2, No. 1, pp. 1-15.

[8] Mann, D. L., and Warnes, G. D., 1994, "Future Directions in Helicopter Engine Protection System Configuration Turbines," 83rd Symposium, Propulsion and Energetic Panels of Erosion, Corrosion and Foreign Object Damage Effect in Gas Turbine 25-8.

[9] Tilly, G. P., and Sage, W., 1970, "The Interaction of Particles and Material Behaviour in Erosion Process," *Journal of Wear*, Vol. 16, pp. 447-465.

[10] Uysal, U., Li, P.-W., Chyu, M. K., and Cunha, F. J., 2006, "Heat Transfer on Internal Surfaces of a Duct Subjected to Impingement of a Jet Array with Varying Jet Hole-Size and Spacing," *Journal of Turbomachinery*, Vol. 128, pp. 158-165.

[11] Florschuetz, L. W., Berry, R. A., and Metzger, D. E., 1980, "Periodic Streamwise Variations of Heat Transfer Coefficients for Inline and Staggered Arrays of Circular Jets with Crossflow of Spent Air," *Journal of Heat Transfer*, Vol. 102, pp. 132-137.

[12] Van Treuren, K. W., Wang, Z., Ireland, P. T., and Jones, T. V., 1993, "Detailed Measurements of Local Heat Transfer Coefficient and Adiabatic Wall Temperature Beneath and Array of Impinging Jets," *Journal of Turbomachinery*, Vol. 16, pp. 369-371.

[13] Hill, P., and Peterson, C., 1992, *Mechanics and Thermodynamics of Propulsion*, Addison-Wesley Publishing Company: Reading, Massachusetts.

[14] Kline, S. J., and McClintock, F. A., 1953, "Describing Uncertainties in Single-Sample Experiments," *Mechanical Engineering*, Vol. 75, pp. 3-8.

Table 1.1. Parameter Uncertainties

	Low RFP	High RFP	Low RFP	High RFP	Low RFP	High RFP
PR	1.02 ± 0.122%	1.10 ± 0.114%	1.10 ± 0.113%	1.12 ± 0.111%	1.71 ± 0.0734%	1.76 ± 0.711%
FP_0	0.153 ± 2.59%	0.358 ± 1.89%	0.368 ± 1.87%	0.405 ± 1.83%	1.08 ± 1.44%	1.13 ± 1.43%
FP	0.143 ± 2.70%	0.0956 ± 3.72%	0.316 ± 1.94%	0.0734 ± 4.75%	1.02 ± 1.45%	0.295 ± 2.19%
RFP	0.0690 ± 50.7%	0.733 ± 1.52%	0.139 ± 16.6%	0.819 ± 1.13%	0.0531 ± 36.4%	0.739 ± 0.920%

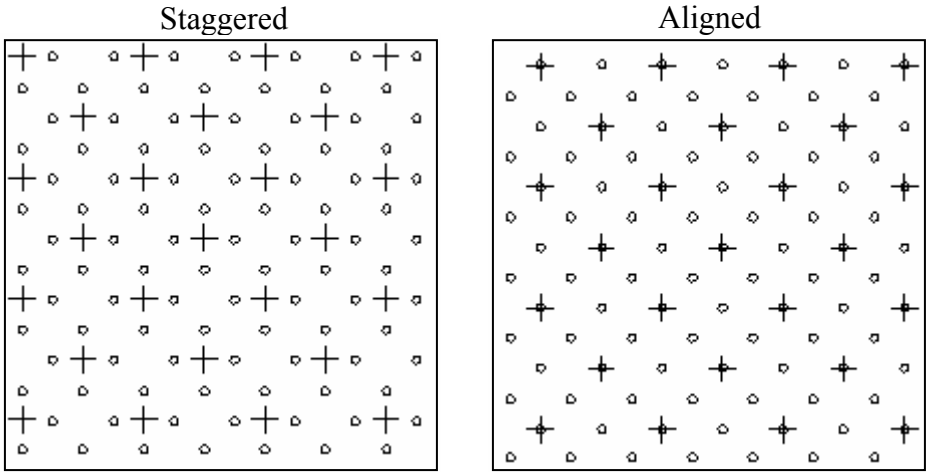

Figure 1.1. The alignment of the impingement jets with respect to the film cooling jets (+ = impingement jets; ° = film-cooling jets).

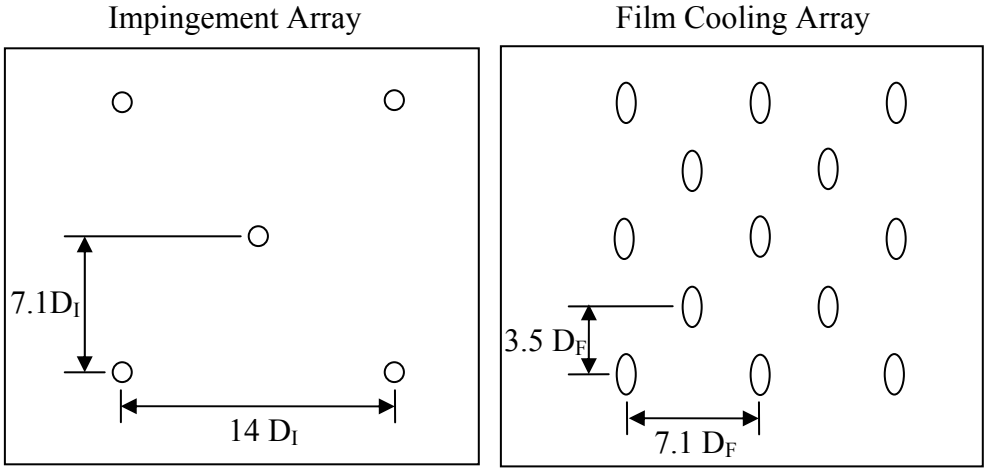

Figure 1.2. The hole layout for the impingement and film cooling arrays.

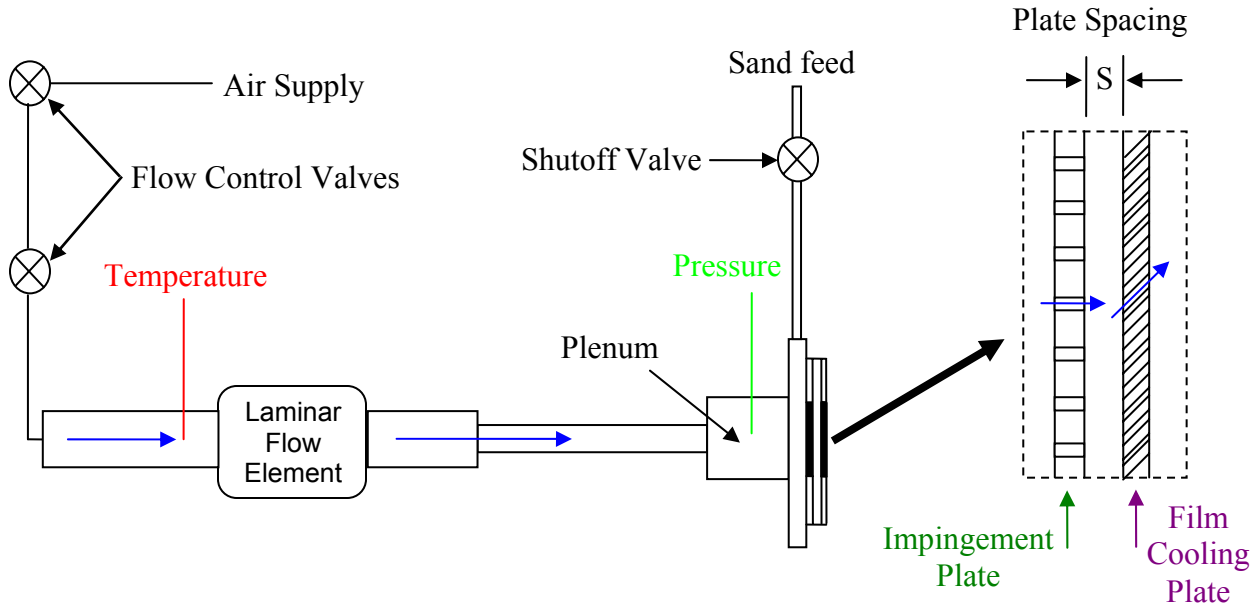

Figure 1.3. Test apparatus for supplying the sand-air mixture to the test coupon.

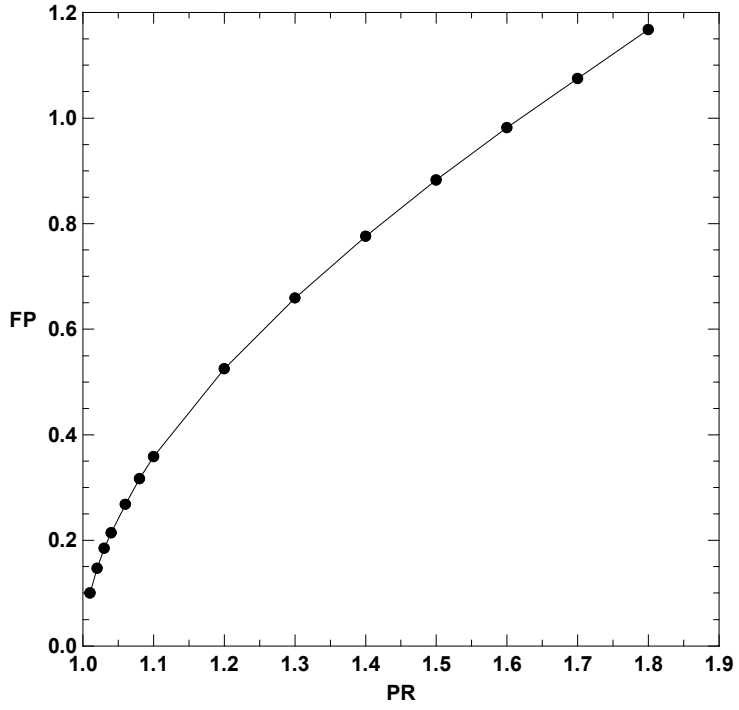

Figure 1.4. Baseline flow parameter versus pressure ratio for all tests using a clean test coupon.

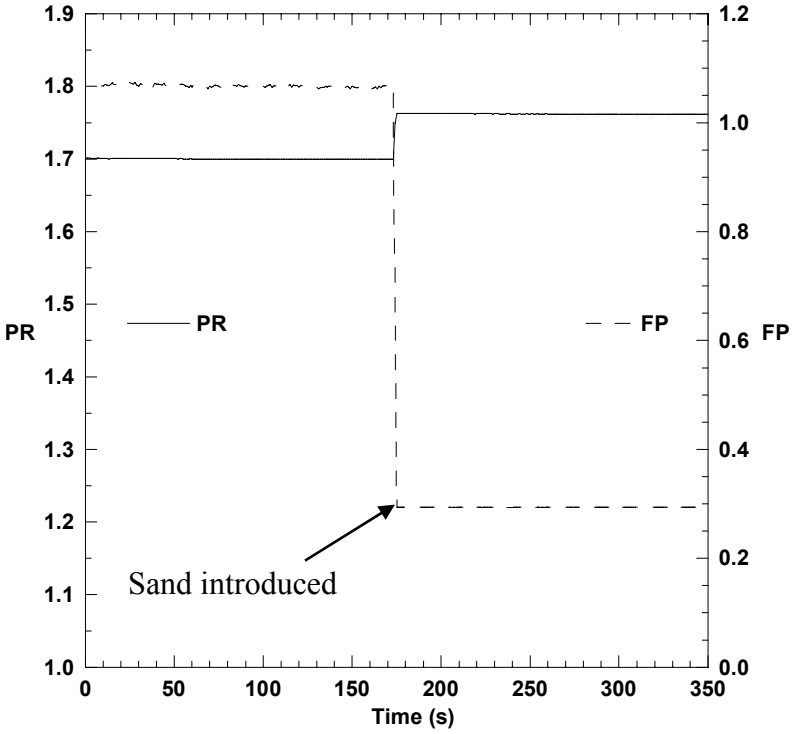

Figure 1.5. Pressure ratio and flow parameter versus time before and after sand is introduced (staggered, S/D_I = 6.25, 0.35 grams, $0<D_S<3800$ µm sand).

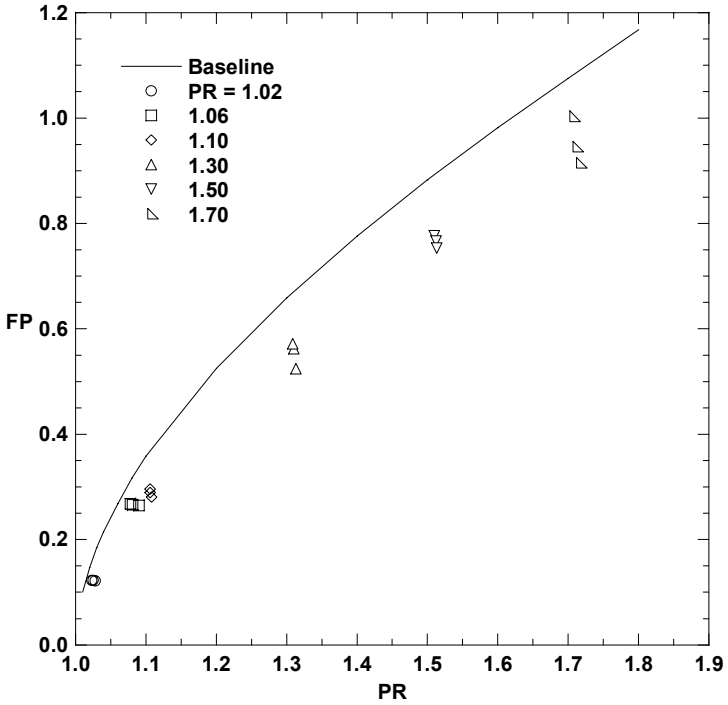

Figure 1.6. Flow parameter baseline and following repeated sand tests versus pressure ratio (staggered, S/D_I = 3.13, 0.35 grams, $0<D_S<3800$ µm sand).

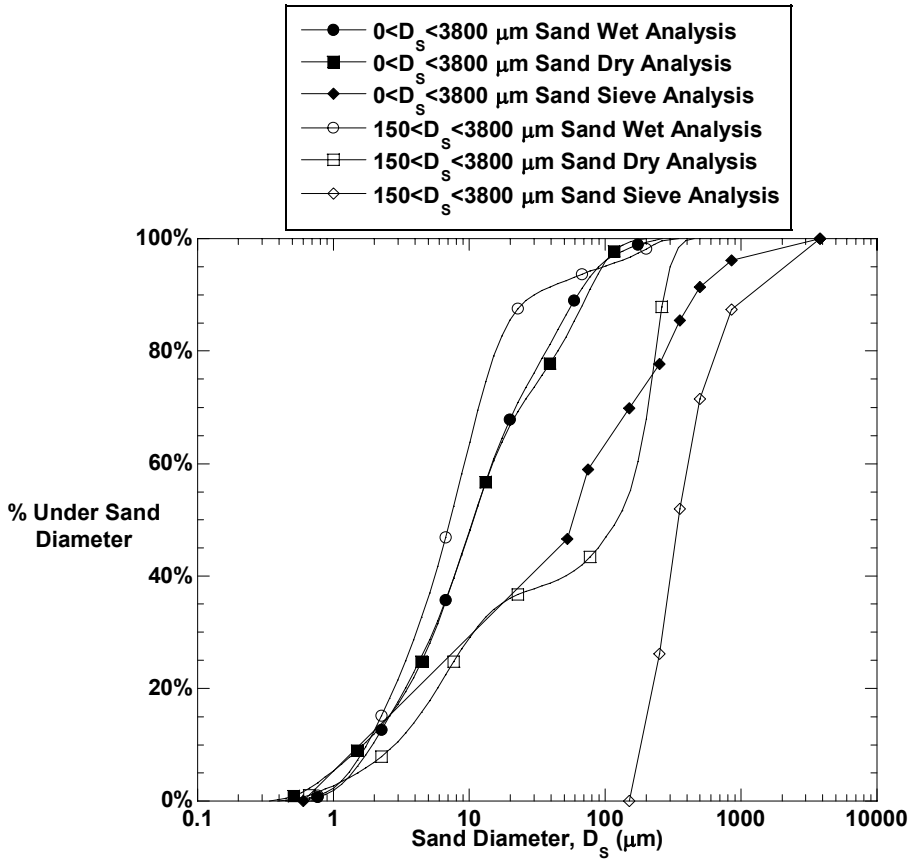

Figure 1.7. Percent of particles under size versus sand diameter for the two test sands analyzed three different ways.

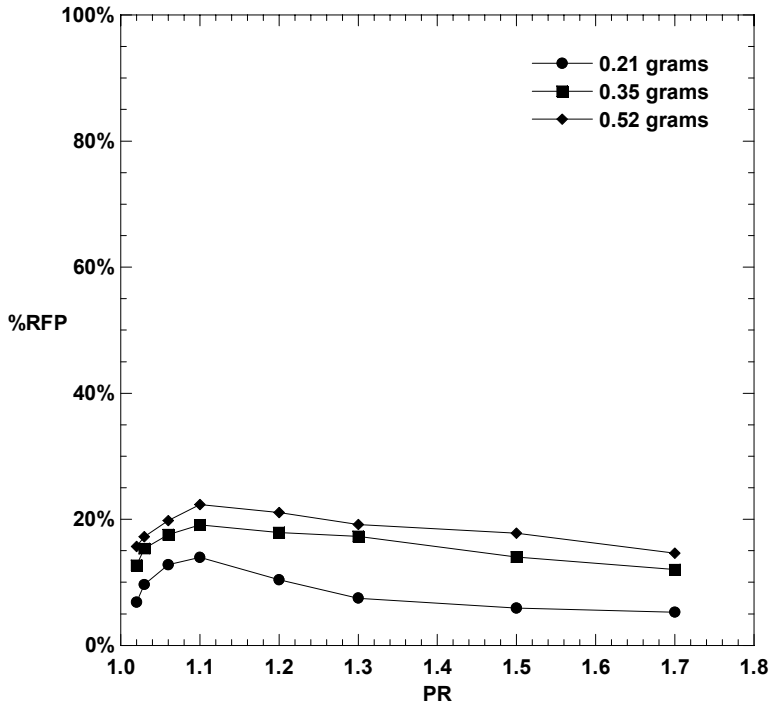

Figure 1.8. Percent reduction in flow parameter versus pressure ratio for varying amounts of sand (staggered, $S/D_I = 3.13$, $0<D_S<3800$ µm sand).

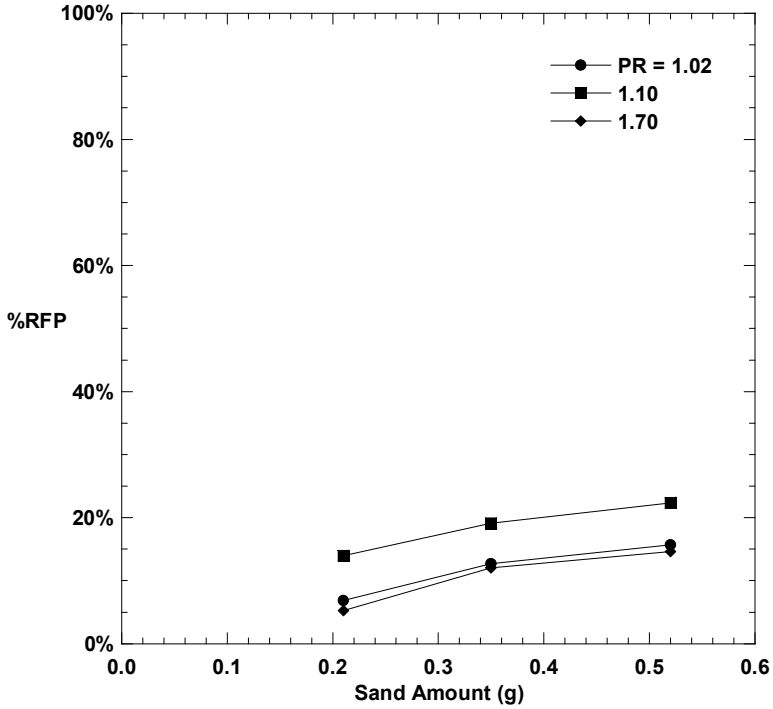

Figure 1.9. Percent reduction in flow parameter versus sand amount for varying pressure ratios (staggered, $S/D_I = 3.13$, $0<D_S<3800$ µm sand).

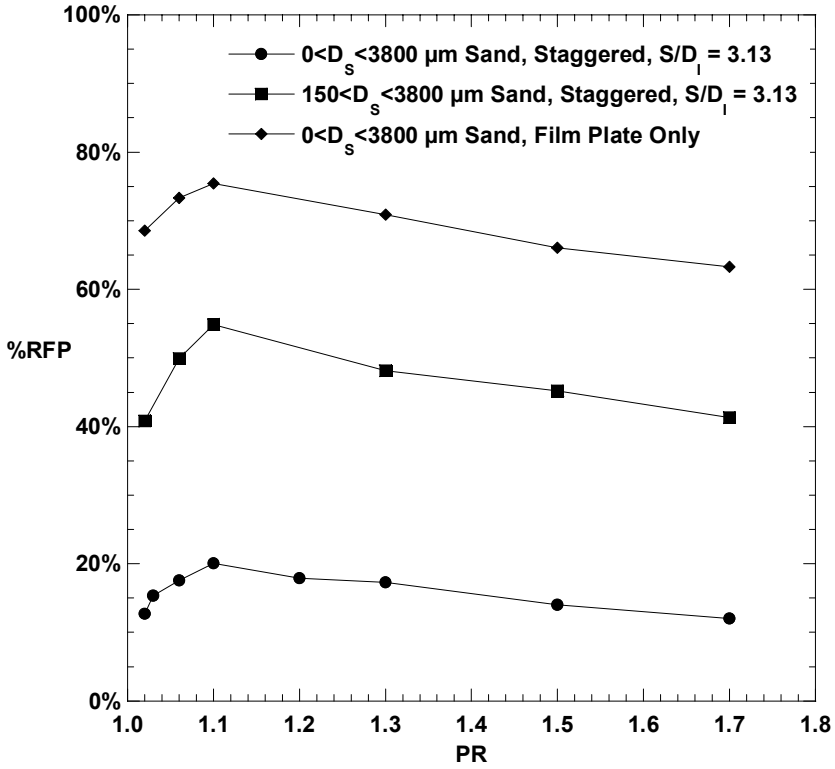

Figure 1.10. Percent reduction in flow parameter versus pressure ratio for varying sand distributions (0.35 grams).

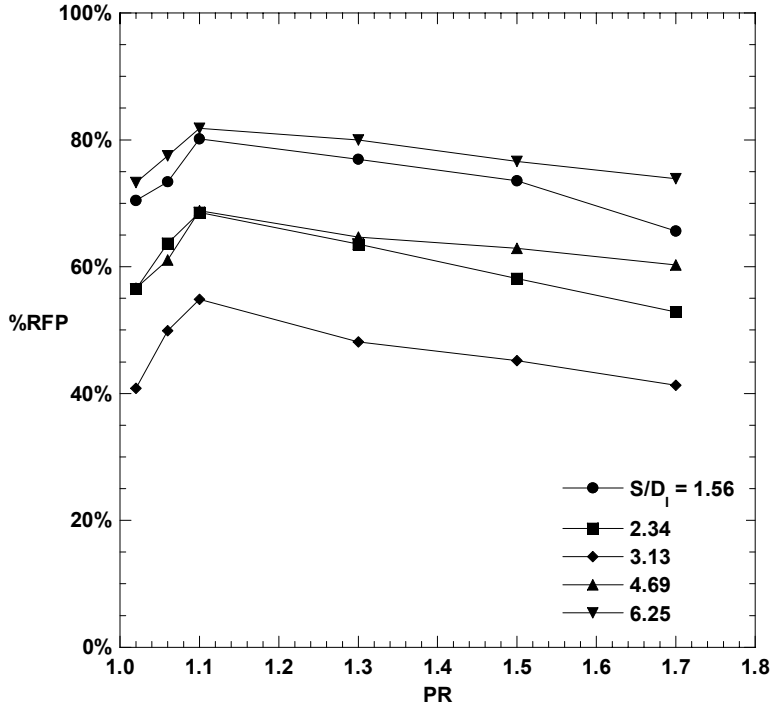

Figure 1.11. Percent reduction in flow parameter versus pressure ratio for varying S/D_I values (staggered, 0.35 grams, $150<D_S<3800$ µm sand).

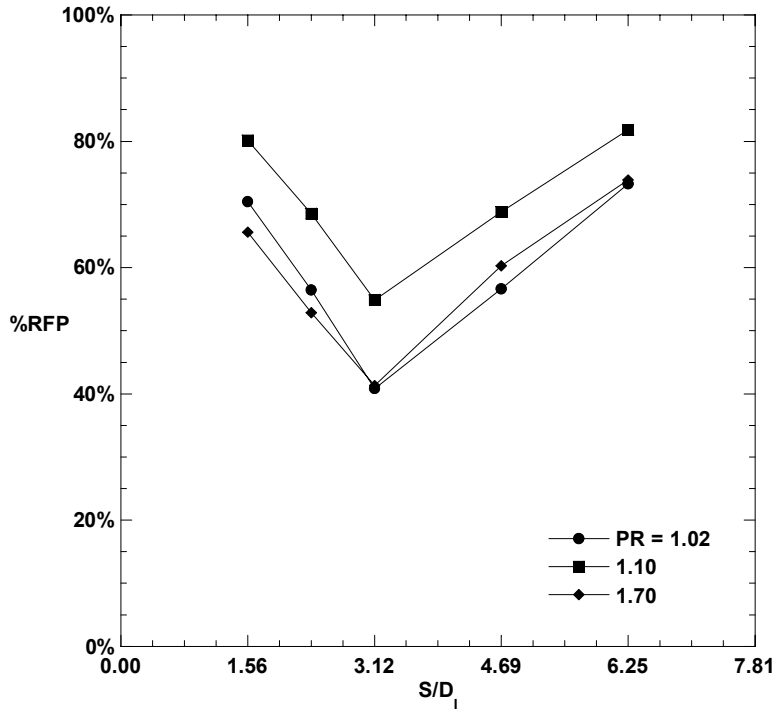

Figure 1.12. Percent reduction in flow parameter versus S/D_I for varying pressure ratios (staggered, 0.35 grams, $150<D_S<3800$ µm sand).

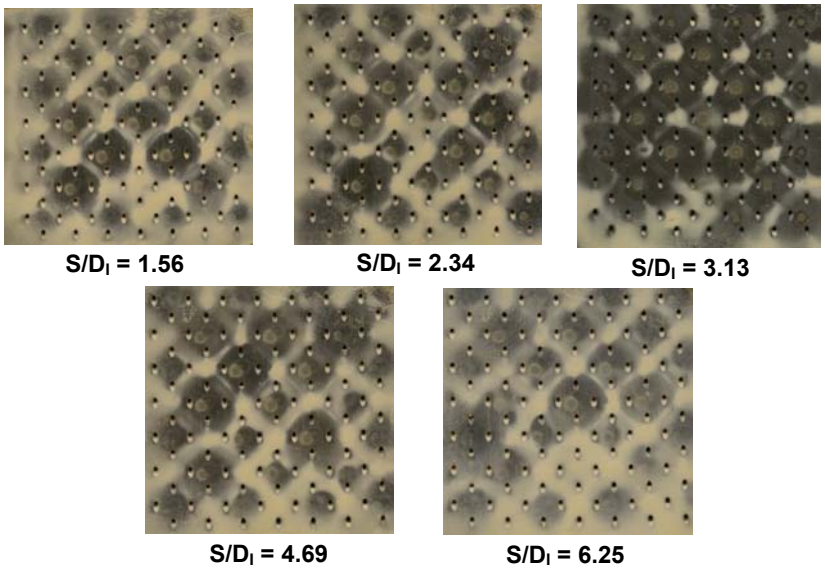

Figure 1.13. Pictures taken on the upstream side of the film-cooling plate at varying S/D_I values (PR = 1.3, 0.35 grams, staggered, $150<D_S<3800$ µm sand).

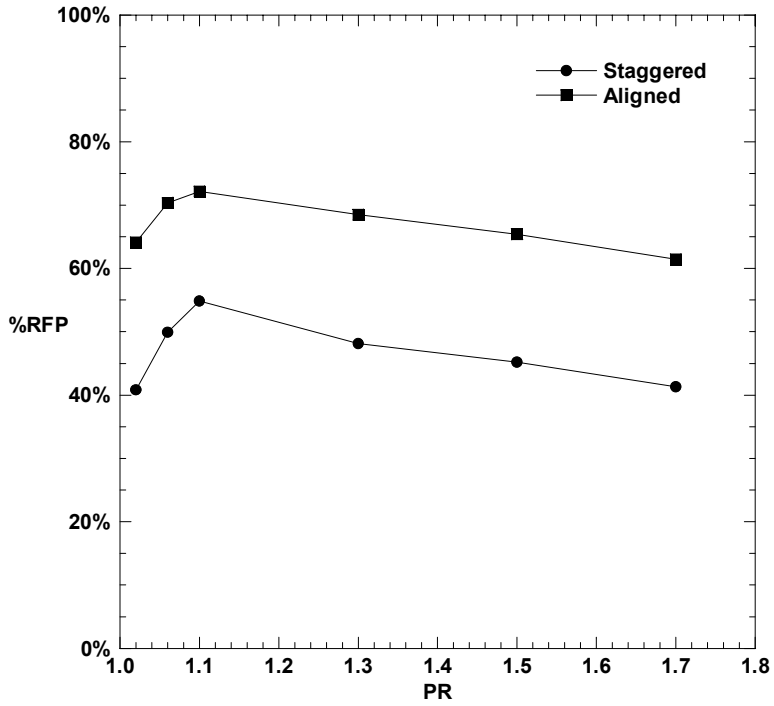

Figure 1.14. Percent reduction in flow parameter versus pressure ratio for varying hole alignments (S/D_I = 3.13, 0.35 grams, 150<D_S<3800 µm sand).

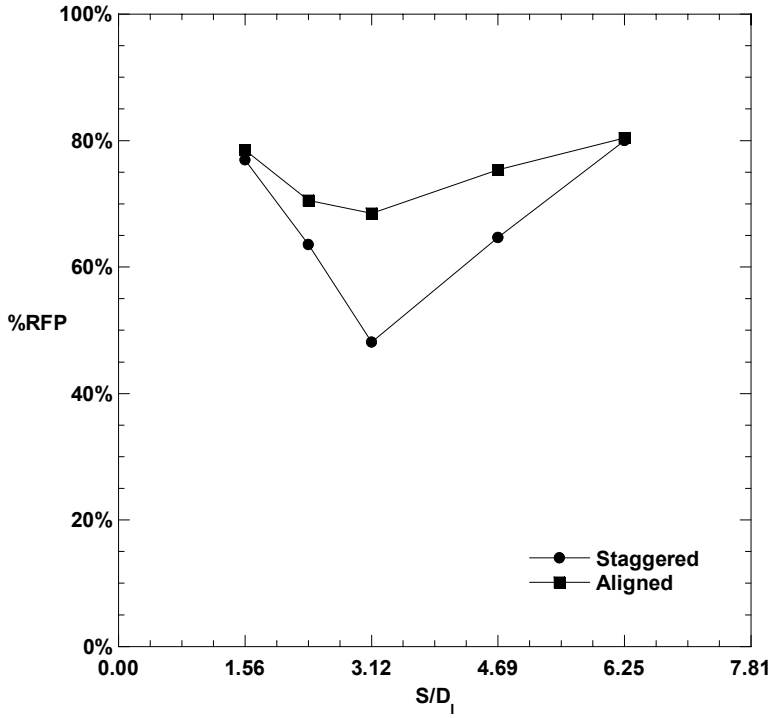

Figure 1.15. Percent reduction in flow parameter versus S/D_I for varying hole alignments (PR = 1.3, 0.35 grams, 150<D_S<3800 µm sand).

Part II:

Sand Blockage Effects on Turbine Blade Outer Air Seals*

Abstract

Gas turbine engines equipped on military aircraft increasingly encounter harsh environments where particle ingestion can occur. The most common occurrence of particle ingestion involves aircraft operating in environments with sand. Sand can block cooling passages in high temperature turbine parts and reduce part life. To keep part temperatures at safe levels below the melting point of the constituent metals, internal convective cooling and external film-cooling are used. The outer air seals on turbine blades use these cooling techniques to keep metal temperatures at acceptable levels. The purpose of this study was to determine how sand reduces the amount of cooling flow in the blade outer air seal for various geometries.

Many different factors were considered while examining the introduction of sand into the coolant flow at room temperature for three different blade outer air seals and eight different cooling geometries. Each outer air seal implemented a forward flow section that cooled the part upstream of the turbine blade and an aft flow section that cooled the part downstream of the turbine blade. Two of the outer air seals used different impingement cooling and film-cooling geometries while the other outer air seal contained two different microcircuit designs, brick-and-mortar and pedestal.

The results from this study provide insight into which outer air seal geometry was least affected by sand ingestion. The primary finding was that the pedestal microcircuit geometry showed less blockage due to ingested sand than the impingement and film-cooling geometries and the brick-and-mortar microcircuit geometry. It is believed that the pedestal geometry promotes particle fragmentation which reduced the sand size. The most important factors that reduced blockage included higher pressure ratios, lower sand amounts, and smaller sand sizes.

*To be submitted to Pratt & Whitney as a final contract report.

Introduction

Military gas turbine engines equipped on aircraft are often exposed to harsh conditions. Sandy environments can be detrimental to engine parts due to erosion and deposition. High turbine inlet temperatures that approach the melting point of sand increase the possibility of these events occurring. These flow temperatures are most critical during takeoff and landing when particles can be ingested into the engine from the ground. The high temperatures exceed the melting temperatures of the first stage turbine components, and therefore these parts must be cooled internally and externally. The focus of this report is on the blade outer air seal (BOAS) for a first stage turbine blade row. Figure 2.1 shows the current BOAS technology using internal impingement cooling and external film-cooling.

New technology has led to the development of innovative cooling techniques called microcircuits that use thin internal passages to promote convective cooling. The BOAS analyzed in this report employs two different microcircuit designs including (1) brick-and-mortar and (2) pedestal arrangements. The brick-and-mortar design, shown in Figure 2.2a, looks like a brick wall where the bricks are solid and the mortar is an open passage where coolant flows. The numerous small passages create a large surface area to promote heat transfer. The pedestal design, shown in Figure 2.2b, has multiple micro cylinders from the floor to the ceiling of the passage. Again, the increased surface area improves heat transfer over previous technology. The passage heights are typically smaller, about 0.010-0.012 inches, than the diameter of a typical film-cooling hole, 0.014 inches.

A field-run V2500 BOAS was provided that had been operated in a sandy environment. Deposition and a reduction in film-cooling hole size were visible on the BOAS that resulted in a reduction in cooling flow of about 16% in the forward flow section and about 5.9% in the aft flow section. The forward flow section refers to the section of the BOAS in which cooling flow exits upstream of where the turbine blade tip makes contact with the BOAS. The aft section has coolant flow that exits downstream of the turbine blade tip. The decrease in flow due to sand was determined by comparing with an unused BOAS with similar dimensions. In all, four BOAS parts were available for testing as listed in Table 2.1. When discussing the BOAS in terms of forward flow

section and aft flow section, the conventional BOAS parts from the V2500 engine will be referred to by the film-cooling hole diameter. The microcircuit BOAS will be described by either microcircuit brick-and-mortar or microcircuit pedestal. The main objective of this paper was to determine how the microcircuit BOAS and the BOAS with 0.019 inch film-cooling holes compared to the new BOAS with 0.014 inch film-cooling holes in terms of blockage due to sand ingestion. To accomplish this, a fixture was developed to hold the BOAS parts and deliver a sand-air mixture. The amount of blockage in the field-run BOAS with 0.014 inch film-cooling holes was determined compared to the new BOAS with 0.014 inch film-cooling holes. Different sand amounts were injected into the new BOAS with 0.014 inch film-cooling holes until the blockage in the field-run BOAS with 0.014 inch film-cooling holes was matched. Using the matched sand quantity, the reduction in flow was determined for the BOAS with 0.019 inch film-cooling holes and the microcircuit BOAS with both the brick-and-mortar and pedestal geometries. The dependence of blockage on sand size was also examined.

In a study conducted congruently with this study, a double-walled liner was tested that had a generic cooling geometry that most closely imitated the cooling geometry in the BOAS parts from the V2500 engine. Both geometries used impingement cooling and film-cooling; however, the arrangement and diameter of the holes were different. Also, the parts from the V2500 engine used fan-shaped film-cooling holes while the double-walled liner used cylindrical film-cooling holes fabricated by electrical discharge machining.

This report focuses on the tests that were performed using the actual engine parts while Part I reported results from generic studies. In the next section, the BOAS hardware (supplied by Pratt & Whitney) is described followed by a description of the test parameters used to compare the cooling geometries. Then a detailed description of the test facility and testing methodology is discussed. A characterization of the sand that was tested is then provided, followed by a discussion of results and conclusions.

BOAS Descriptions

The blade outer air seals used in testing were provided by Pratt & Whitney. Figure 2.3 shows the field-run BOAS with 0.014 inch film-cooling holes. This BOAS had been used in the V2500 engine for some time and had undergone sand ingestion. Deposition was visible on the external side of the BOAS especially at the leading edge. Another prevalent characteristic was the scarring that resulted from contact with the tips of the first stage turbine blades. The cooling passages in the conventional BOAS pieces from the V2500 engine are separated into a forward compartment and an aft compartment. A summary of the hole diameters in the conventional BOAS parts is presented in Table 2.2. The forward compartment contained 0.029 inch diameter impingement holes, 0.014 inch diameter film-cooling holes, and 0.026 and 0.029 inch slashface gap holes. The slashface gap is the area where two outer air seals lay side-by-side. The aft compartment contained 0.020 inch diameter impingement holes, 0.014 inch film-cooling holes, and 0.026 inch slashface gap holes. The new BOAS with 0.014 inch film-cooling holes shown in Figure 2.4 had the same nominal dimensions as the field-run BOAS with 0.014 inch film-cooling holes. The geometry depicting the forward and aft sections of the BOAS with 0.014 inch film-cooling holes are shown in Figure 2.5 and were provided by the project sponsor [1]. The difference between these two BOAS pieces was that the new BOAS with 0.014 inch film-cooling holes had never been installed in an operating engine and therefore all of its cooling passages and holes were clear of particles.

The BOAS with 0.019 inch film-cooling holes in Figure 2.6 also used impingement cooling and film-cooling but had different dimensions than the field-run BOAS with 0.014 inch film-cooling holes and the new BOAS with 0.014 inch film-cooling holes. The geometry depicting the forward and aft sections of the BOAS with 0.019 inch film-cooling holes are shown in Figure 2.7 and were provided by the project sponsor [1]. The forward compartment contained 0.029 inch diameter impingement holes, 0.019 inch diameter film-cooling holes, and 0.026 and 0.029 inch slashface gap holes. The aft compartment contained 0.023 inch diameter impingement holes, 0.019 inch diameter film-cooling holes, and 0.026 inch slashface gap holes.

The microcircuit BOAS is shown in Figure 2.8 and will be referred to in figures as microcircuit brick-and-mortar or microcircuit pedestal. The brick-and-mortar inlets are on the face of the cavity in Figure 2.8(a). The pedestal inlets can be seen on the right edge and top edge of the cavity in Figure 2.8(b). The brick-and-mortar passage exits at the surface in contact with the turbine blade tips can be seen in Figure 2.8(c). The pedestal passages exit in the slashface gap and the leading edge gap.

Matching Flowrates for Microcircuit Studies

Considering the different cooling techniques and geometries tested, the need existed to compare blockage based on a common baseline. The baseline flowrate for the new BOAS with 0.014 inch film-cooling holes was matched in the microcircuit brick-and-mortar and microcircuit pedestal geometries by flowing only certain sections of the brick-and-mortar or pedestal inlets. The conventional BOAS parts had two separate cavities using independent coolant flows. The microcircuit BOAS had nine different cavities using independent coolant flows. The significance of these cavities is discussed here.

The BOAS parts that employed impingement and film-cooling had separate flow sections in relation to the blade row. The flow from the forward cavity for these parts exits into the main gas path upstream of the first stage turbine blade row. A friction mark is visible in Figure 2.3 (b) where the turbine blades made contact with the outer air seal to reduce tip leakage during operation. The flow from the aft cavity exits into the main gas path downstream of the first stage turbine blade row. Due to the location of the cavities, the blockage characteristics were different. As will be discussed later, the forward section of the field-run BOAS with 0.014 inch film-cooling holes had a higher reduction in flow parameter than the aft section. Also different coolant pressure ratios are available for each cavity due to the pressure in an engine upstream of the turbine blade row being higher than the pressure downstream of the turbine blade row. For these reasons, testing was performed separately on both cavities. To restrict the coolant flow to the particular flow section being injected with the sand-air mixture, tape was used to cover the impingement holes in the other flow section.

The microcircuit BOAS has different flow cores that contain either the brick-and-mortar geometry or the pedestal geometry. The inlet areas of the microcircuit BOAS were opened or closed depending upon the amount of flow needed to match the existing BOAS design. This information was provided by the sponsor [2] and is illustrated in Figure 2.9. Table 2.3 gives the flow cores for each microcircuit geometry that were injected with the sand-air mixture to match the flow in the forward and aft flow sections of the new BOAS with 0.014 inch film-cooling holes. Figure 2.10 shows the tape and gasket material used to block inlets to inject the sand-air mixture into the flow cores for the various microcircuit geometries matching the forward and aft flow. The inlets left open for the microcircuit brick-and-mortar forward flow started with the letters AE, AF, AG, and AH. The inlets left unblocked for the microcircuit brick-and-mortar aft flow started with the letters AE and AG. The inlets left unblocked for the microcircuit pedestal forward flow started with the letters Y, AA, AB, and AJ. The inlets left open for the microcircuit pedestal aft flow started with the letters Y and AJ.

Test Parameters

To be consistent with Pratt & Whitney, a dimensional form of the flow parameter called the flow function was used. Removing the area term and the gas constant for air from the flow parameter equation, the flow function is shown in equation 2.1.

$$FF=\frac{\dot{m}\sqrt{T_{0C}}}{P_{\infty}}=f\left(\frac{P_{0C}}{P_{\infty}},\text{geometry},T_{0C}\right)\left[\frac{\text{lbm}/\text{s}\sqrt{\text{R}}}{\text{psia}}\right] \tag{2.1}$$

For cold tests, the flow function is defined using the pressure downstream of the part tested. The total temperature is measured upstream of the part in case the coolant temperature is different from the ambient temperature. The mass flow is determined using a Meriam 50MJ10-9 laminar flow element (LFE). Meriam directed how to calculate the mass flow through the LFE shown in equation 2.2.

$$\dot{m}=\left(B*\Delta P+C*\Delta P^{2}\right)*\frac{\mu_{std}}{\mu_{C}}*\frac{P_{0C}}{P_{std}}*\frac{T_{std}}{T_{0C}}*\rho_{std} \tag{2.2}$$

The coefficients, B and C, are found from a calibration curve for the LFE and used with the differential pressure, ΔP, across the LFE to determine the actual volumetric flow rate. The flow rate was then normalized to the standard pressure and temperature.

Finally the standard volumetric flow rate was multiplied by the density of air at standard conditions to get the mass flow rate. The viscosity of the coolant was found by equation 2.3 using the total temperature of the coolant.

$$\mu_C = \frac{b*T_{0C}^{3/2}}{S+T_{0C}} \tag{2.3}$$

The pressure ratio refers to the ratio of the supply coolant pressure to the exit static pressure, as shown in equation 2.4. The supply coolant pressure was measured upstream of the BOAS while the exit static pressure, the atmospheric pressure in the test laboratory, was measured downstream of the BOAS.

$$PR = \frac{P_{0C}}{P_{\infty}} \tag{2.4}$$

The baseline flow functions were measured for each BOAS and for each forward and aft section. Figures 2.11-2.14 show all of the baseline flow functions for all possible pressure ratios as well as Pratt & Whitney (P&W) predictions. The flow function for the field-run BOAS with 0.014 inch film-cooling holes is also included. Pratt & Whitney did not flow test the parts, however, they did provide analytical estimations of the flow for each section of each part. These estimations were consistently higher than the measured flow at low pressure ratios and lower at high pressure ratios. It is believed that the geometric tolerances in the machining of the parts resulted in the actual flow being different from the analytical flow. Sections of the microcircuit inlets were blocked to mimic the amount of flow in the forward and aft sections of the new BOAS with 0.014 inch film-cooling holes. The BOAS with 0.019 inch film-cooling holes had a higher flow function than the new BOAS with 0.014 inch film-cooling holes for both flow sections. A curve fit was applied to each flow function so comparisons could be made when pressure ratios increased during testing. The curve fit for all of the baseline flow functions were in the form of equation 2.5 and the coefficients are given in Table 2.4.

$$FF_0 = C1 \times PR^3 + C2 \times PR^2 + C3 \times PR + C4 \tag{2.5}$$

In this study it was necessary to describe how the flow function changed due to sand blockage. After sand was ingested, the flow function decreased. To identify the amount of blockage during sand ingestion tests, the percent reduction in flow function (%RFF), defined in equation 2.6, was used. The baseline flow function and post sand

flow function in this equation were evaluated at the same pressure ratio. Appendix A contains sample calculations for the test parameters in this section.

$$\%RFF = \left| \frac{FF_0 - FF}{FF_0} \right|_{PR} \tag{2.6}$$

Experimental Facility and Methodology

Figure 2.15 illustrates the test apparatus for supplying air and sand to the BOAS as well as the location of the measurements that were made. The coolant air was supplied at an elevated pressure from a compressed air line at room temperature. The pressure was regulated between 1.3 psig and 11 psig. The amount of coolant was controlled by a pressure regulator and a precision control valve that both contained screens to filter any particles. To measure temperature, a thermocouple was placed 5 pipe diameters upstream of the laminar flow element (LFE). The coolant flow was measured with an LFE having a maximum capacity of 3.0 SCFM. To ensure that fully developed flow conditions were present at the LFE inlet during testing, the LFE was positioned between two pieces of pipe that extended approximately ten diameters upstream and ten diameters downstream. The pressure measurement upstream of the BOAS was taken inside a piece of square tubing. The sand was injected by way of a gravity feed through a drilled hole in the plate located immediately upstream of the BOAS.

A custom-made rubber gasket was fashioned from gasket material and used for sealing the BOAS. Due to the irregular shape of the BOAS, caulk was also applied on both sides of the gasket to improve the sealing method. A plate with a hole milled in the middle was bolted on top of the BOAS touching the BOAS only at the corners to interfere with the exit flow as little as possible. When bolted, coolant could flow to the BOAS without leaking to the environment.

Instrumentation

The instrumentation used to conduct these experiments included pressure transducers, a thermocouple, and a precision scale. The measurements made with these instruments allowed the coolant mass flow, pressure ratio, coolant temperature, and sand weight to be determined. One pressure measurement needed was the differential pressure

across the laminar flow element. This was detected using a Validyne DP103 diaphragm pressure transducer with a maximum output of 8.9 inches of water. Also needed to determine the mass flow was the coolant temperature and pressure upstream of the LFE. A Type K nickel-chrome sheathed thermocouple probe was used to monitor the coolant temperature while an Omega PX139 pressure transducer with a maximum readable pressure of 30 psig was used to monitor the coolant pressure.

To determine the pressure ratio, two additional pressure transducers were used. A Setra 280E pressure transducer with a maximum pressure of 15 psig was used to determine the pressure in the plenum upstream of the BOAS. The external atmospheric pressure was measured using a Setra 370 digital barometric pressure gauge having a range of 11.6 psia to 16.0 psia. The area ratio of the plenum cross-section to the impingement holes was sufficiently large (71:1 for the largest impingement area), and therefore the pressure measurements taken inside the plenum, upstream of the BOAS, were treated as the total coolant supply pressure.

Testing Methodology

Prior to performing tests with injected sand particles, baseline measurements were made to determine the flow function and pressure ratio under clean conditions shown previously in Figures 2.11 through 2.14.

For the sand injection tests, a small oven was used to first dry the sand at 150°C for a time period of at least four hours. Following this drying process, the coolant flow rate to the coupon was set using the precision control valves shown in Figure 2.15. Having reached the desired pressure ratio, the flow function was determined and compared to the baseline flow function. If the flow did not match the expected flow, it was most likely that there was sand remaining in the BOAS from the previous test and the BOAS was then cleaned using compressed air. This process was continued until the baseline flow function was achieved for the given pressure ratio.

After successfully cleaning the BOAS and setting the desired pressure ratio, the sand was removed from the oven, weighed, and loaded into the airtight section of pipe with the shutoff valve at the sand feed (refer to Figure 2.15). The sand remained in the hot oven until immediately before each test, but it returned to room temperature prior to

releasing it upstream of the BOAS for testing. With steady flow conditions achieved, the feed valve was opened to introduce the sand into the coolant flow stream. The sand then flowed through the BOAS in a very short time period being on the order of a couple of seconds. The flow function and pressure ratio were then again recorded. As a result of the sand injection, the rate of flow passing through the BOAS decreased and the pressure upstream of the test coupon increased as shown in Figure 2.16. Also seen in Figure 2.16 was that after the blockage had occurred, the flow conditions remained steady over time. The %RFF was then calculated using the steady state values of flow function and pressure ratio.

Uncertainty Analysis

For all of the results presented in this study, three tests were conducted with the average of these three tests reported as the final value. Using three tests was determined by Walsh et al. [3] to give reasonable repeatability of 6.9%. Figure 2.17 shows the baseline flow parameter with the three resulting flow parameters following the introduction of sand for a set of tests. The uncertainties associated with the parameters discussed in this study were estimated using the partial derivative propagation of uncertainty method by Kline et al. [4]. The results of performing the uncertainty calculations are shown in Tables 2.5 and 2.6.

Table 2.5 gives the uncertainties for a low and high value of %RFP for the pressure ratios tested with the forward flow sections. Table 2.6 gives the uncertainties with the aft flow sections. The pressure ratio uncertainties were relatively low and were dominated by the bias uncertainty of the pressure transducer detecting the plenum pressure upstream of the BOAS. The uncertainties of the flow function and reduction in flow function were heavily influenced by the bias uncertainty of the pressure transducer measuring the total pressure directly upstream of the laminar flow element. The uncertainty of the amount of sand injected into the flow was directly dependent on the accuracy of the scale used to weigh the sand which was ± 0.0010g. The higher the value of %RFP the lower the percent uncertainty.

Sand Characterization

Initially, many different ways were used to characterize the sand provided by Pratt & Whitney that was used in this study. A Horiba LA-700 Particle Size Analyzer was used to examine the sand samples, however, a problem was encountered with the analyzer which caused all of the sand samples to reduce to a base size. The LA-700 essentially used a combination of liquid dispersant, circulation, and agitation to inspect the particles, and it is believed that this combination process overstressed the samples. Testing required sand samples with large concentrations of large particles to be injected into the coolant flow upstream of the BOAS to determine the effects of sand ingestion on blockage. To further verify the misleading sand diameters, sand samples having different size distributions were made using a series of sieves. While these samples contained particle diameters measurable up to 0.15 inch, no particles larger than 0.0080 inch were detected by the LA-700. With a small applied force, almost all particles over 0.0080 inch could be broken down into smaller grains.

The sand inspection process was repeated using a next generation particle size analyzer from Horiba but it also had the same problems as its predecessor. The Horiba Partica LA-950 Particle Size Analyzer also used liquid dispersant, circulation, and agitation to inspect the particles, which again caused the sand to reduce to a base size. An accessory to the LA-950 called the Powderjet Dry Feeder was ultimately used which operates with air as the dispersing fluid instead of water. In the wet method, the liquid dispersant was assumed to cause the majority of the sand to break up, so the dry method was attempted to obtain a more accurate characterization. Unfortunately, the dry method also resulted in the breakdown of particles, and the characterization analysis again did not accurately describe the size of sand particles reaching the test coupon.

Another issue with using the LA-950 in either the wet or dry mode involved the selection of a refractive index for the sand. While refractive indices are widely documented for most homogeneous materials, it is much more difficult to determine the refractive index for heterogeneous materials such as sand. Using ISO (International Standards Organization) fine and coarse sand samples, a sensitivity study was conducted to determine the variability in sand diameter distribution arising from different refractive indices. The results of varying the real component of the refractive index and eliminating

the imaginary component for the fine sand using the wet mode are shown in Figure 2.18. The results of varying the real component for the coarse sand using the wet mode are shown in Figure 2.19. The real component for the refractive index was assumed to be close to the real component for quartz (SiO_2) since sand is 68-76% quartz. The real component refers to the ratio of the velocity of light in a vacuum to the velocity of light in the material. The refractive index for quartz is 1.45. Due to the additional substances present in sand, the ISO sand supplier (Powder Technology Inc.) used a real component of 1.51 to do their characterizations.

The results of varying the imaginary component of the refractive index and keeping the real component constant for the fine sand using the wet mode are shown in Figure 2.20. The results of varying the imaginary component for the coarse sand using the wet mode are shown in Figure 2.21. Since sand is somewhat opaque, an imaginary component for the refractive index should also be used. Quartz is transparent, so its imaginary component is zero. The imaginary component is the reduction of transmission of optical radiation caused by absorption and scattering of light. Using different imaginary components for the refractive index, the resulting sand characterizations varied dramatically for the same sample of sand.

Considering these problems, a simple sieve analysis was then performed to accurately determine the range of sand particle diameters in the sand provided by Pratt & Whitney used during testing. The sieve analyses gave the size distribution by using a range of sieves to separate the particles. The separated particles were then weighed and the fraction of particles for a particle diameter range was then calculated based on the weight of a particular sample size. The results of the sieve analysis are shown in Figure 2.22 by percent of particles under the corresponding diameter. The sand samples used during testing are referred to by the range of sand particle diameters present. Sieves with mesh sizes ranging from 0.0021 inch to 0.033 inch were stacked in descending order with the largest sieve at the top. Then a sample of sand was weighed and loaded into the top sieve in the stack. The stack was agitated until the sand grains remained in the sieve corresponding to the grains' sizes. The sand present in each sieve was then weighed as well as the sand that passed through all of the sieves. Using the total sample weight, a percentage was calculated from the amount of sand in a single sieve compared to the

total. Particles as large as 0.15 inch were measured with calipers. This sieve method provided what was believed to be the most accurate characterization of the sand distribution. The sand samples used in testing will be referred to by the range of sand diameters present in the sand.

Discussion of Results

The first objective of this study was to establish the amount of blockage in a field-run blade outer air seal by comparing its flow parameter with the flow parameter of a new blade outer air seal having the same nominal geometry. Using this information, the amount of sand needed to mimic the blockage in the field-run BOAS was then determined. These sand amounts were then injected into the different cooling geometries to allow comparisons to be made to the field-run BOAS. Many different parameters were investigated during this study including the sand amount (weight), sand size, cooling geometry, and pressure ratio, as detailed in Table 2.7. Appendix B provides the raw data for every test conducted using the BOAS parts.

Field-Run BOAS Results

As was previously stated, baseline flow function curves were determined for every piece of hardware received from Pratt & Whitney and are shown in Figures 2.11 through 2.14. Three separate goals were achieved from these baseline curves. For the new parts the baseline provided a comparison to determine whether the part was clean after performing a test with sand. The baseline curves also allowed the reduction in flow function to be determined for each sand test. Before any testing was conducted, however, the field-run baseline was used to determine the amount of blockage in the field-run BOAS with 0.014 inch film-cooling holes compared to the new BOAS with 0.014 inch film-cooling holes.

The forward cavity flow function for the field-run BOAS with 0.014 inch film-cooling holes and the new BOAS with 0.014 inch film-cooling holes are shown again in Figure 2.23 along with the target reduction in flow function determined from the two curves. The target reduction in flow function refers to the amount of blockage needed to be matched by injecting sand with the full range of diameters into the coolant upstream of the new BOAS with 0.014 inch film-cooling holes. The flow functions increased

nonlinearly with respect to pressure ratio. The amount of blockage in terms of reduction in flow function ranged from 14% to 17% as seen in Table 2.8. Figure 2.24 shows the baseline flow function curves for the aft flow sections of the field-run BOAS with 0.014 inch film-cooling holes and the new BOAS with 0.014 inch film-cooling holes. Again the flow functions increased nonlinearly. The target reduction in flow function obtained from these curves is also shown. The blockage increased from 5% to 7% in the aft section as again seen in Table 2.8. Since the flow was higher in the forward flow section, loose particles were more likely to flow through the cooling passages and cause blockage.

Sand Map Results

Using the baselines for the field-run BOAS with 0.014 inch film-cooling holes and the new BOAS with 0.014 inch film-cooling holes, tests were conducted to determine the amount of sand needed to match the blockage measured in the field-run BOAS with 0.014 inch film-cooling holes. A wide range of sand amounts was tested to produce a large sand map.

Figure 2.25 shows the sand map for the forward flow section of the new BOAS with 0.014 inch film-cooling holes. The sand amounts ranged from 0.20 grams to 0.60 grams. Tests on the forward flow sections were conducted at initial pressure ratios of 1.1, 1.3, 1.5, and 1.7. Sand amounts producing blockages that most closely matched the field-run BOAS with 0.014 inch film-cooling holes were selected and are shown in Table 2.9. The sand amounts ranged from 0.25 grams at an initial pressure ratio of 1.1 to 0.54 grams at an initial pressure ratio of 1.7. It is important to note that the pressure ratio could rise as much as 0.10 after the introduction of sand and therefore the initial pressure ratios are reported here.

Figure 2.26 shows the sand performance map for the aft flow section of the new BOAS with 0.014 inch film-cooling holes. The sand amounts ranged from 0.010 grams to 0.080 grams. Tests on aft flow sections were conducted at initial pressure ratios of 1.2, 1.4, 1.6, and 1.8. Sand amounts producing blockages that most closely matched the field-run BOAS with 0.014 inch film-cooling holes are shown in Table 2.10. These matched sand amounts ranged from 0.010 grams at an initial pressure ratio of 1.2 to 0.060 grams at an initial pressure ratio of 1.8. The aft flow section required much less sand to match

the blockage in the field-run BOAS with 0.014 inch film-cooling holes. Another important factor was the greatly reduced flow in the aft cavity compared to the forward cavity. In general, less sand was required to cause blockage when coolant flow was decreased.

Comparison of Cooling Geometries

After determining the amount of sand needed to reproduce the blockage in the field-run BOAS with 0.014 inch film-cooling holes, the selected sand amounts were injected into the coolant stream upstream of the other BOAS geometries available for testing. A full range of tests were also conducted using different sand diameter distributions. The effects of sand distribution are discussed later. Figure 2.27 shows the results of testing the forward flow sections of the four different BOAS geometries using sand having a diameter distribution ranging from immeasurably small to 0.15 inch. The first thing to note here is that the pedestal microcircuit geometry was blocked less than the others tested. This was believed to occur because the pedestals acted as areas of impingement where sand particles could be broken down into smaller diameters and passed more easily through the pedestal array. The brick-and-mortar microcircuit design contained corners where sand was more likely to stick thus reducing the coolant flow. The BOAS with 0.019 inch film-cooling holes was expected to block less than the other geometries due to the increased flow in the forward cavity. Compared to the new BOAS with 0.014 inch film-cooling holes however, the BOAS with 0.019 inch film-cooling holes was blocked more. The larger inlet area for the BOAS with 0.019 inch film-cooling holes allowed more sand to enter resulting in higher measured blockages.

Figures 2.28 through 2.30 show the results of testing %RFF using sand having increasingly higher concentrations of large sand diameters in the forward flow sections of the four different BOAS geometries. The pedestal microcircuit geometry blocked nearly the same as the new BOAS with 0.014 inch film-cooling holes. It is believed therefore that the pedestal geometry passed smaller particles better than the other geometries. The BOAS with 0.019 inch film-cooling holes and the brick-and-mortar microcircuit geometry performed consistently worse than the new BOAS with 0.014 inch film-cooling holes and the pedestal geometry. The amount of blockage was relatively constant at the

pressure ratios tested due to the selected sand amounts increasing with increasing pressure ratios. The resulting pressure ratios for the tests conducted on the BOAS with 0.019 inch film-cooling holes were consistently higher than those for the other geometries because the flowrate was higher.

Figure 2.31 shows the results of %RFF testing with the full range of sand diameters on the aft flow sections of the four different BOAS geometries. Again the pedestal microcircuit geometry blocked less than the other geometries. Even with the reduced flow, the sand impinging on the pedestals reduced the particle size allowing the sand to more easily pass through the part. In contrast to the forward cavity, the BOAS with 0.019 inch film-cooling holes blocked less than the new BOAS with 0.014 inch film-cooling holes. The smaller impingement holes on the new BOAS with 0.014 inch film-cooling holes became blocked with sand. The blockage followed the same general trend as the target reduction in flow function, increasing by about 2% from the lowest pressure ratio to the highest pressure ratio.

Varying Sand Diameter Distribution Results

The distribution of sand diameter was deemed to be another important parameter affecting the operation of the various BOAS geometries. Sand samples having different size distributions were injected into the coolant upstream of the BOAS at varying pressure ratios. Figures 2.32 through 2.35 show the effect of varying the sand distribution. The first sand sample contained the full range of sand diameter ranging from immeasurably small to 0.15 inch. The second sand sample contained sand diameters ranging from 0.0021 inch to 0.15 inch. The third sample included sand diameters ranging from 0.0030 inch to 0.15 inch. The last sample consisted of sand having diameters ranging from 0.0059 inch to 0.15 inch.

The trends dependent on sand size distribution were consistent for each of the geometries tested. The sand samples with the full range of particles contained a large concentration (~47%) of particles under 0.0021 inch in diameter. The blockage increased significantly when these smaller particles were removed. The blockage did not increase as much when removing the sand particles for the subsequent sand samples. This was a result of the concentration of particles with diameters between 0.0021 inch and 0.0030

inch (~12%) being relatively similar to the concentration of particles with diameters between 0.0030 inch and 0.0059 inch (~11%). Removing particles in these ranges had a smaller effect on blockage.

Conclusions

The purpose of this section was to test the performance of different blade outer air seals having different cooling geometries when injected with sand. Blockages from sand reduced the effectiveness of cooling by decreasing the coolant flowrate, and subsequently part life can be greatly reduced. The effects of pressure ratio and sand amount were verified by sand maps where a new BOAS with 0.014 inch film-cooling holes was injected with sand to match the blockage in a field-run BOAS with 0.014 inch film-cooling holes. Each geometry had a forward flow section and an aft flow section. The effects of cooling geometry and sand diameter distribution were analyzed in greater detail.

From the sand maps, blockages increased as the sand amount was increased. The amount of blockage was determined by comparing the flow after sand was introduced to the flow for a clean, unblocked part at the same pressure ratio. Also evident from the sand maps, blockage levels decreased with increasing pressure ratios.

Three different BOAS parts were tested to determine their resistance to blockage from sand ingestion. Two parts, the new BOAS with 0.014 inch film-cooling holes and the BOAS with 0.019 inch film-cooling holes, utilized impingement and film-cooling with different hole dimensions. The third BOAS contained two different microcircuit cooling geometries, brick-and-mortar and pedestal. The BOAS with 0.019 inch film-cooling holes had higher flow functions than the new BOAS with 0.014 inch film-cooling holes. Certain inlets in the microcircuit BOAS were blocked to match the flow in the new BOAS with 0.014 inch film-cooling holes.

For the forward and aft flow tests with the full range of sand diameters, the pedestal geometry blocked less than the other geometries by producing lower reductions in flow function. This was likely due to areas of impingement that promoted particle fragmentation. At the other sand diameter distributions tested, the reduction in flow function due to sand ingestion was relatively similar for the different geometries.

The results from these tests indicated that the pedestal microcircuit geometry was an improved design in terms of susceptibility to sand ingestion and subsequent cooling flow reduction over designs currently in use and also the brick-and-mortar microcircuit geometry. Considering the heat transfer benefits of the innovative microcircuit geometries, the characteristics of the pedestal geometry should be employed in other cooling geometries if flow blockage due to sand ingestion is of concern. The brick-and-mortar geometry likely contains areas where particles became lodged. Reducing the number of these areas would likely improve the performance of the brick-and-mortar geometry in terms of blockage due to sand ingestion.

Nomenclature

%RFF	percent reduction in flow function
b	viscosity coefficient
B	LFE calibration constant
C	LFE calibration constant
C1	curve fit coefficient
C2	curve fit coefficient
C3	curve fit coefficient
C4	curve fit coefficient
D	sand diameter
ΔP	differential pressure across the LFE
FF	flow parameter
LFE	laminar flow element
$\dot{m}$	mass flow
P	pressure
PR	pressure ratio
RI	refractive index
S	viscosity constant
T	temperature

Greek

ρ	density
μ	dynamic viscosity

Subscripts

0	baseline conditions with no sand
0C	total property of the coolant
0LFE	property upstream of the LFE
∞	freestream conditions
C	property of the coolant
std	standard conditions

References

[1] Joe, C. and Lutjen, P., 2006, personal communication on January 25, 2006.

[2] Joe, C. and Lutjen, P., 2005, personal communication on December 9, 2005.

[3] Walsh, W. S., Thole K. A., and Joe, C., 2006, "Effects of Sand Ingestion on the Blockage of Film-Cooling Holes," GT2006-90067.

[4] Kline, S. J., and McClintock, F. A., 1953, "Describing Uncertainties in Single-Sample Experiments," *Mechanical Engineering*, Vol. 75, pp. 3-8.

Table 2.1. BOAS Parts Provided by Pratt & Whitney

Part #	Status	Description	Cooling Geometry	Film-Cooling Hole Diameter (in)	Figures
2A3295	Field-Run	V2500	Conventional	0.014	2.3, 2.5
2A3515	New	V2500	Conventional	0.014	2.4, 2.5
2A3886	New	V2500	Conventional	0.019	2.6, 2.7
NA	New	Microcircuit	Brick-and-Mortar and Pedestal	NA	2.8, 2.9

Table 2.2. V2500 BOAS Hole Dimensions

Part #	Flow Cavity	Impingement Hole Diameter (in)	Number of Impingement Holes	Film-Cooling Hole Diameter (in)	Number of Film-Cooling Holes	Slashface Gap Hole Diameter (in)
2A3295	Forward	0.029	18	0.014	44	3x0.026, 4x0.029
2A3295	Aft	0.020	16	0.014	40	2x0.026
2A3515	Forward	0.029	18	0.014	44	3x0.026, 4x0.029
2A3515	Aft	0.020	16	0.014	40	2x0.026
2A3886	Forward	0.029	24	0.019	42	3x0.026, 4x0.029
2A3886	Aft	0.023	16	0.019	28	2x0.026

Table 2.3. Microcircuit BOAS Flow Cores

Microcircuit Geometry	Flow Section	Flow Cores from Figure 2.9
Brick-and-Mortar	Forward	AE, AF, AG, AH
Brick-and-Mortar	Aft	AE, AG
Pedestal	Forward	Y, AA, AB, AJ
Pedestal	Aft	Y, AJ

Table 2.4. Coefficients for Baseline Curve Fits

BOAS	Status	Flow Section	C1	C2	C3	C4
2A3295	Field-Run	Forward	0.005077	-0.02554	0.04707	-0.02581
2A3295	Field-Run	Aft	0.001310	-0.007169	0.01567	-0.009244
2A3515	New	Forward	0.004369	-0.02243	0.04388	-0.02481
2A3515	New	Aft	0.001222	-0.006654	0.01502	-0.008981
2A3886	New	Forward	0.007916	-0.03863	0.07181	-0.03968
2A3886	New	Aft	0.001752	-0.009276	0.02067	-0.01229
Brick-and-Mortar	New	Forward	0.004108	-0.02019	0.04002	-0.02322
Brick-and-Mortar	New	Aft	0.001334	-0.006827	0.01517	-0.009186
Pedestal	New	Forward	0.005684	-0.02710	0.04942	-0.02711
Pedestal	New	Aft	0.001103	-0.005995	0.01385	-0.008369

Table 2.5. Forward Flow Parameter Uncertainties

	Pedestal	Brick-and-Mortar	Pedestal	Brick-and-Mortar
PR	1.10 ± 0.114%	1.11 ± 0.114%	1.71 ± 0.0740%	1.76 ± 0.718%
FF_0 (lbm*R^0.5/s/psia)	0.00206 ± 1.63%	0.00197 ± 1.66%	0.00658 ± 1.04%	0.00704 ± 1.02%
FF (lbm*R^0.5/s/psia)	0.00188 ± 1.69%	0.000904 ± 2.55%	0.00609 ± 1.06%	0.00343 ± 1.29%
RFF	0.0890 ± 17.2%	0.541 ± 2.17%	0.0739 ± 13.3%	0.513 ± 1.22%

Table 2.6. Aft Flow Parameter Uncertainties

	Pedestal	Brick-and-Mortar	Pedestal	Brick-and-Mortar
PR	1.20 ± 0.104%	1.20 ± 0.104%	1.80 ± 0.0693%	1.80 ± 0.0694%
FF_0 (lbm*R^0.5/s/psia)	0.00153 ± 1.86%	0.00150 ± 1.88%	0.00358 ± 1.26%	0.00380 ± 1.22%
FF (lbm*R^0.5/s/psia)	0.00150 ± 1.88%	0.00139 ± 1.97%	0.00346 ± 1.28%	0.00339 ± 1.29%
RFF	0.0191 ± 96.1%	0.0764 ± 23.8%	0.0325 ± 38.1%	0.107 ± 10.8%

Table 2.7. BOAS Test Matrix

BOAS	Flow Section	Condition	PRs	Sand Amounts (g)	Sand Distribution	Figure	Description
2A3295	Forward	Field-Run	1.1-1.8	None	None	2.11, 2.23	Baseline
2A3295	Aft	Field-Run	1.2-1.9	None	None	2.11, 2.24	Baseline
2A3515	Forward	New	1.1-1.8	None	None	2.11, 2.23	Baseline
2A3515	Aft	New	1.2-1.9	None	None	2.11, 2.24	Baseline
2A3886	Forward	New	1.1-1.8	None	None	2.12	Baseline
2A3886	Aft	New	1.2-1.9	None	None	2.12	Baseline
Brick-and-Mortar	Forward	New	1.1-1.8	None	None	2.13	Baseline
Brick-and-Mortar	Aft	New	1.2-1.9	None	None	2.13	Baseline
Pedestal	Forward	New	1.1-1.8	None	None	2.14	Baseline
Pedestal	Aft	New	1.2-1.9	None	None	2.14	Baseline
2A3515	Forward	New	1.1-1.7	0.20-0.60	0<D<0.15 in.	2.25	Sand Map
2A3515	Aft	New	1.2-1.8	0.010-0.080	0<D<0.15 in.	2.26	Sand Map
2A3515	Forward	New	1.1-1.7	0.25-0.54	0<D<0.15 in.	2.25, 2.27, 2.32	Sand Comparison
2A3515	Forward	New	1.1-1.7	0.25-0.54	0.0021<D<0.15 in.	2.28, 2.32	Sand Comparison
2A3515	Forward	New	1.1-1.7	0.25-0.54	0.0030<D<0.15 in.	2.29, 2.32	Sand Comparison
2A3515	Forward	New	1.1-1.7	0.25-0.54	0.0059<D<0.15 in.	2.30, 2.32	Sand Comparison
2A3515	Aft	New	1.2-1.8	0.010-0.060	0<D<0.15 in.	2.26, 2.31	Sand Comparison
2A3886	Forward	New	1.1-1.7	0.25-0.54	0<D<0.15 in.	2.27, 2.33	Sand Comparison
2A3886	Forward	New	1.1-1.7	0.25-0.54	0.0021<D<0.15 in.	2.28, 2.33	Sand Comparison
2A3886	Forward	New	1.1-1.7	0.25-0.54	0.0030<D<0.15 in.	2.29, 2.33	Sand Comparison
2A3886	Forward	New	1.1-1.7	0.25-0.54	0.0059<D<0.15 in.	2.30, 2.33	Sand Comparison
2A3886	Aft	New	1.2-1.8	0.010-0.060	0<D<0.15 in.	2.31	Sand Comparison
Brick-and-Mortar	Forward	New	1.1-1.7	0.25-0.54	0<D<0.15 in.	2.27, 2.34	Sand Comparison
Brick-and-Mortar	Forward	New	1.1-1.7	0.25-0.54	0.0021<D<0.15 in.	2.28, 2.34	Sand Comparison
Brick-and-Mortar	Forward	New	1.1-1.7	0.25-0.54	0.0030<D<0.15 in.	2.29, 2.34	Sand Comparison
Brick-and-Mortar	Forward	New	1.1-1.7	0.25-0.54	0.0059<D<0.15 in.	2.30, 2.34	Sand Comparison
Brick-and-Mortar	Aft	New	1.2-1.8	0.010-0.060	0<D<0.15 in.	2.31	Sand Comparison
Pedestal	Forward	New	1.1-1.7	0.25-0.54	0<D<0.15 in.	2.27, 2.35	Sand Comparison
Pedestal	Forward	New	1.1-1.7	0.25-0.54	0.0021<D<0.15 in.	2.28, 2.35	Sand Comparison
Pedestal	Forward	New	1.1-1.7	0.25-0.54	0.0030<D<0.15 in.	2.29, 2.35	Sand Comparison
Pedestal	Forward	New	1.1-1.7	0.25-0.54	0.0059<D<0.15 in.	2.30, 2.35	Sand Comparison
Pedestal	Aft	New	1.2-1.8	0.010-0.060	0<D<0.15 in.	2.31	Sand Comparison

Table 2.8. Baseline FF and Target %RFF

PR	Baseline FP				%RFF	
	New BOAS with 0.014 Inch Film-Cooling Holes		Field-Run BOAS with 0.014 Inch Film-Cooling Holes			
	Forward	Aft	Forward	Aft	Forward	Aft
1.1	0.00213		0.00181		15.0%	
1.2	0.00312	0.00157	0.00269	0.00150	14.0%	4.65%
1.3	0.00394	0.00199	0.00337	0.00189	14.4%	5.09%
1.4	0.00464	0.00236	0.00395	0.00223	14.9%	5.24%
1.5	0.00529	0.00270	0.00446	0.00255	15.7%	5.59%
1.6	0.00589	0.00302	0.00492	0.00284	16.5%	6.02%
1.7	0.00645	0.00333	0.00535	0.00311	17.0%	6.59%
1.8	0.00699	0.00362	0.00577	0.00337	17.4%	7.01%
1.9		0.00391		0.00363		7.31%

Table 2.9. Forward Cavity Sand Amounts

PR	Sand needed to mimic field-run BOAS	%RFF Target	%RFF Tested
1.1	0.25	15.0%	16.3%
1.3	0.28	14.4%	15.9%
1.5	0.42	15.7%	16.7%
1.7	0.54	17.0%	16.9%

Table 2.10. Aft Cavity Sand Amounts

PR	Sand needed to mimic field-run BOAS	% RFF Target	% RFF Tested
1.2	0.010	4.65%	4.97%
1.4	0.020	5.24%	5.20%
1.6	0.040	6.02%	6.34%
1.8	0.060	7.01%	7.50%

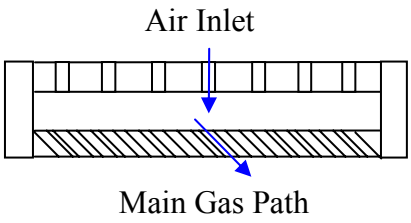

Figure 2.1. Current generic BOAS geometry with impingement cooling and film-cooling.

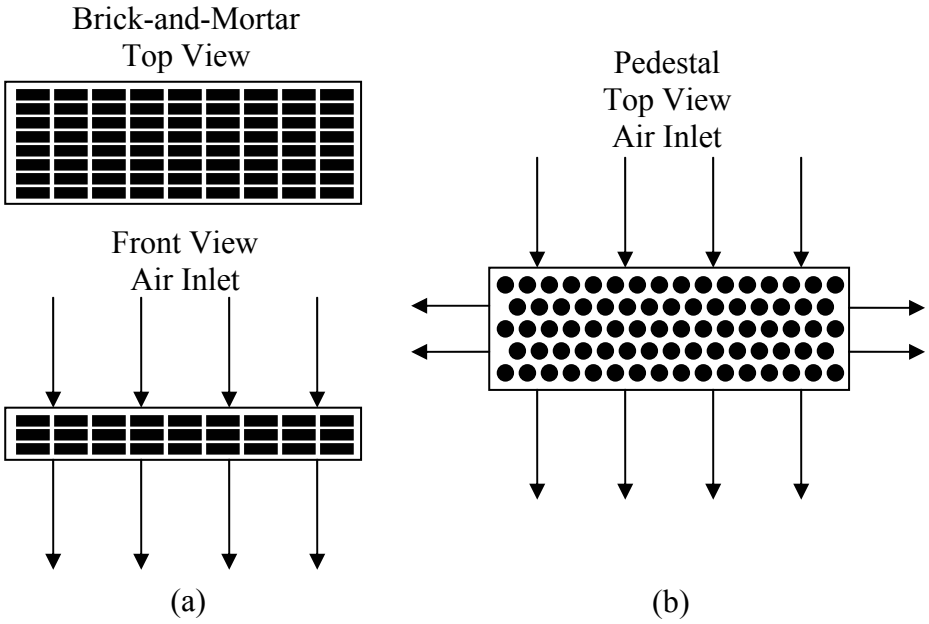

Figure 2.2. Generic brick-and-mortar (a) and pedestal (b) microcircuit geometries.

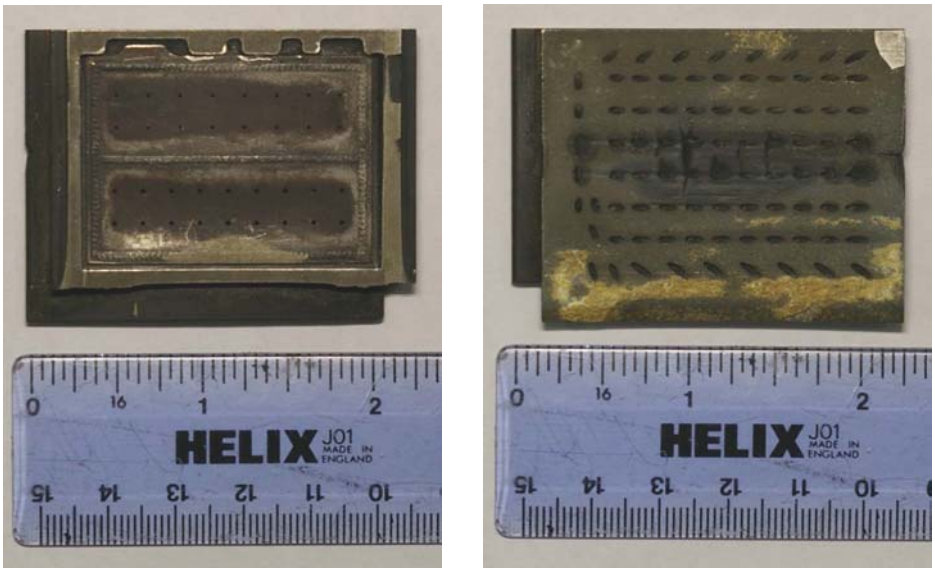

(a) (b)

Figure 2.3. Field-run BOAS with 0.014 inch film-cooling holes inlet (a) and exit (b).

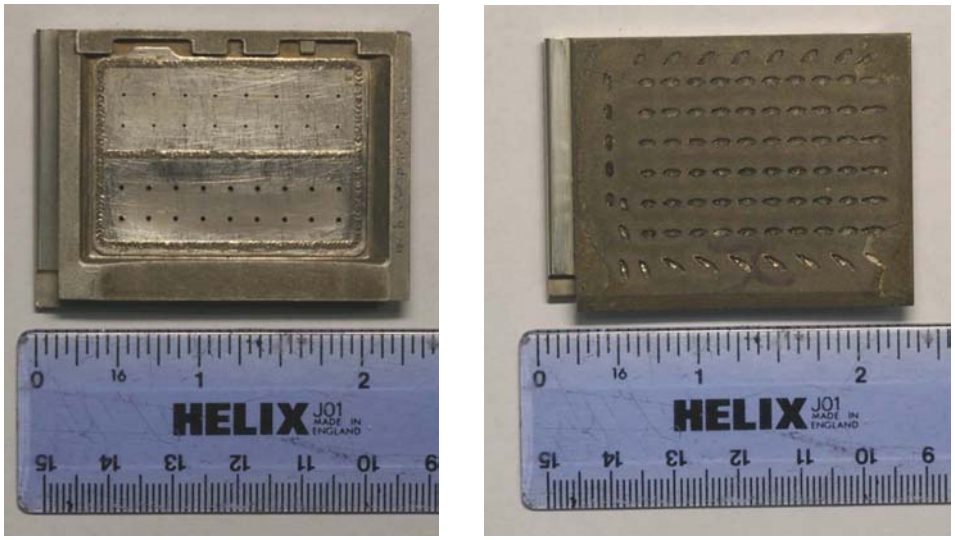

(a) (b)

Figure 2.4. New BOAS with 0.014 inch film-cooling holes inlet (a) and exit (b).

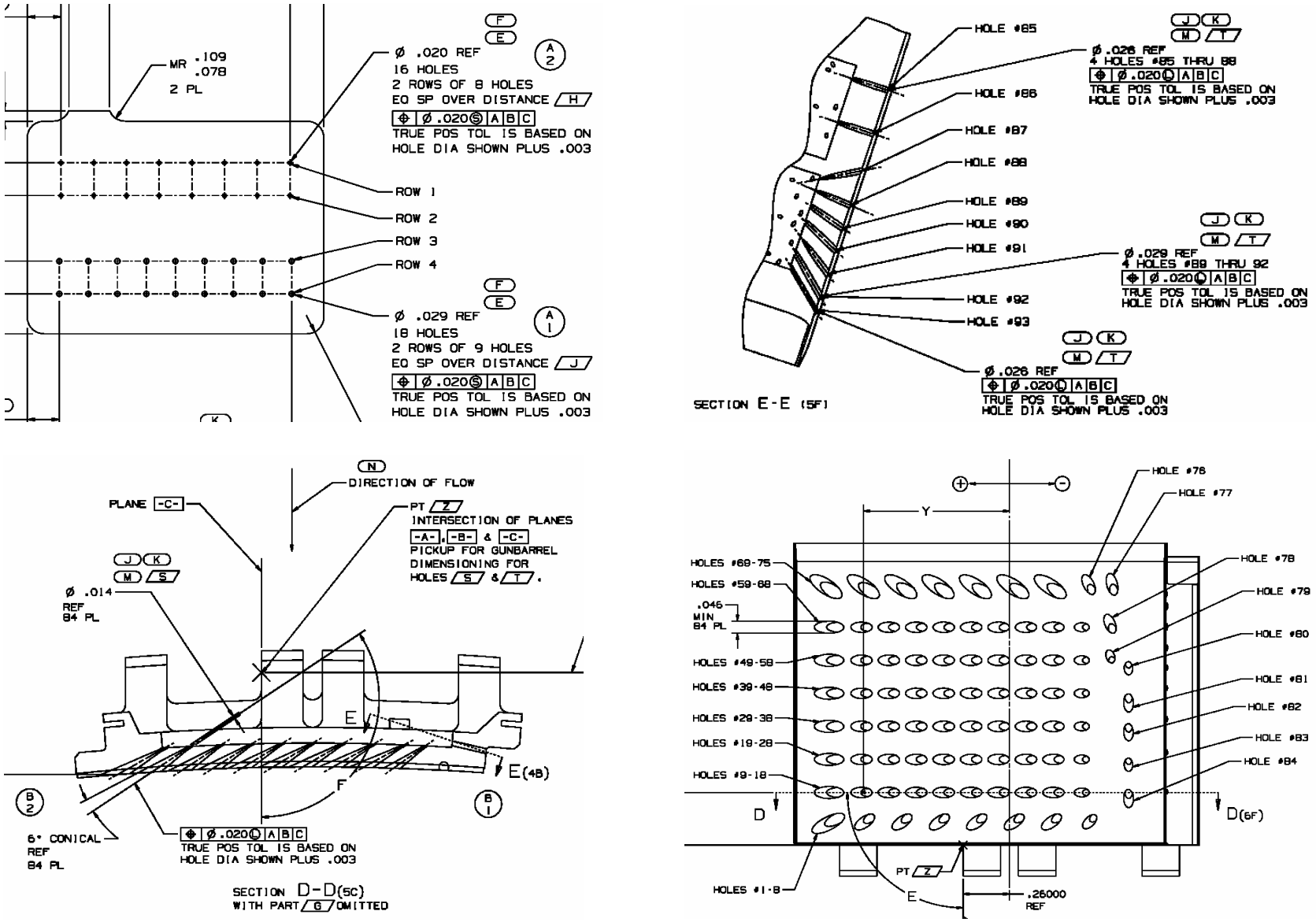

Figure 2.5. Pratt & Whitney schematics of the BOAS parts with 0.014 inch film-cooling holes [1].

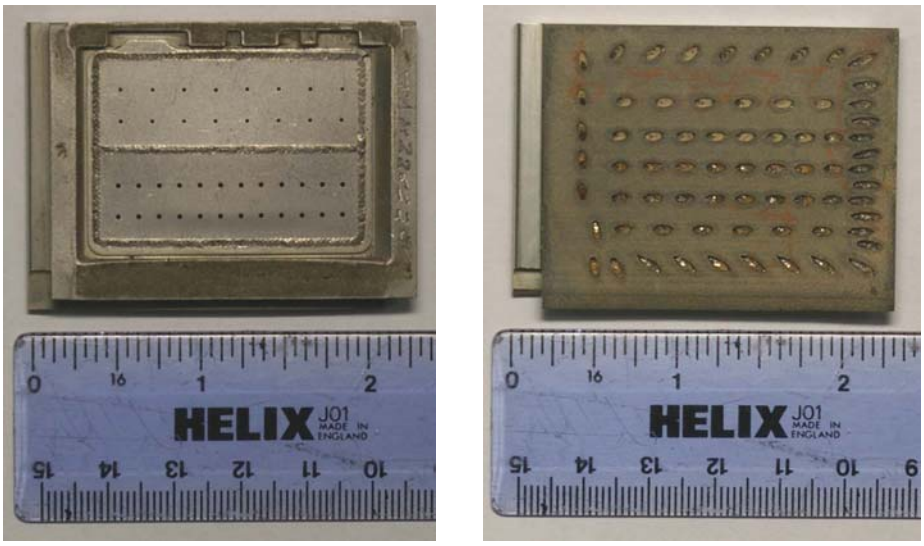

(a) (b)

Figure 2.6. BOAS with 0.019 inch film-cooling holes inlet (a) and exit (b).

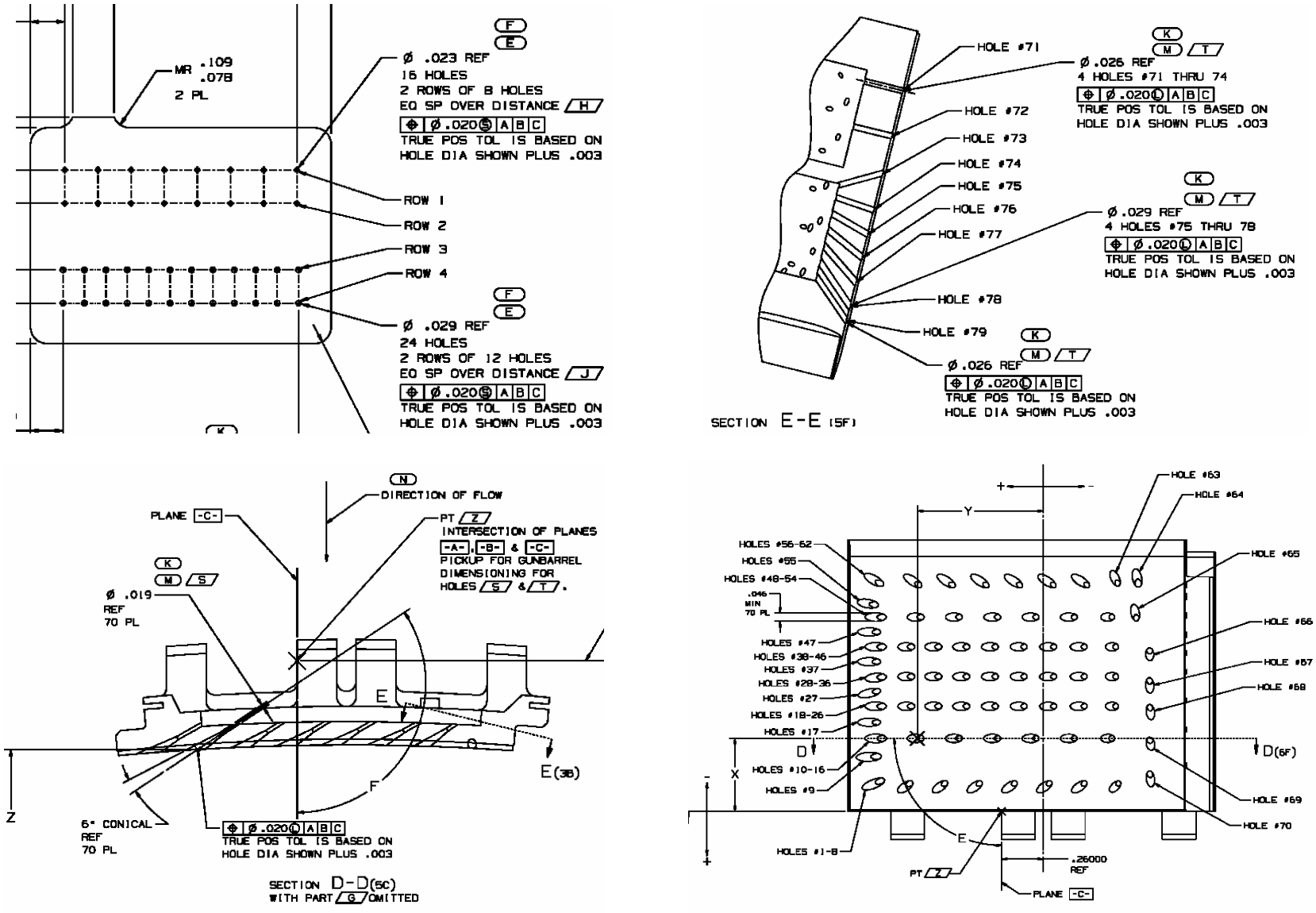

Figure 2.7. Pratt & Whitney schematics of the BOAS with 0.019 inch film-cooling holes [1].

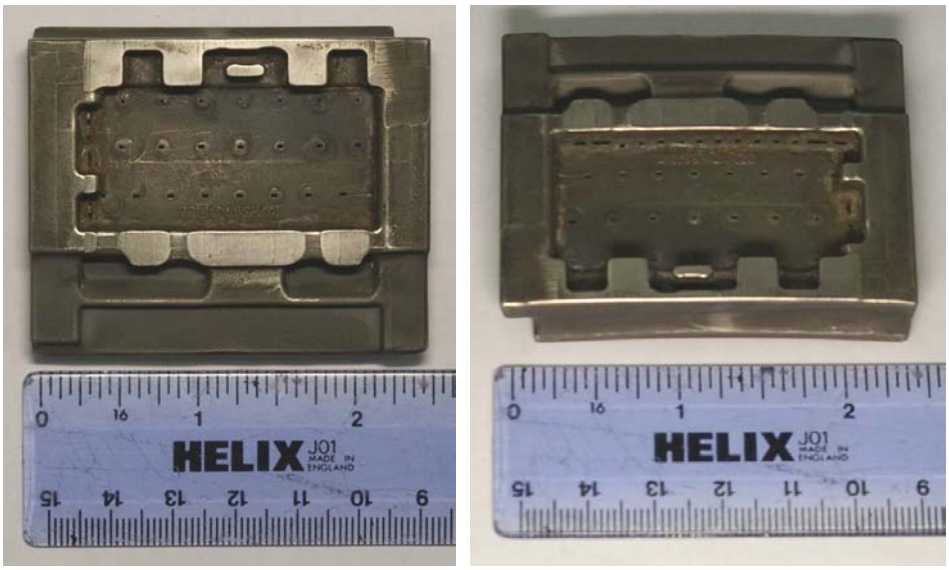

(a) (b)

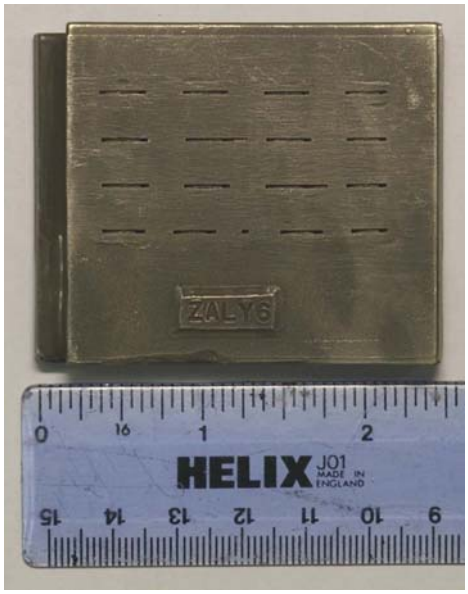

(c)

Figure 2.8. Microcircuit BOAS inlet straight on (a), inlet angled (b), and exit (c).

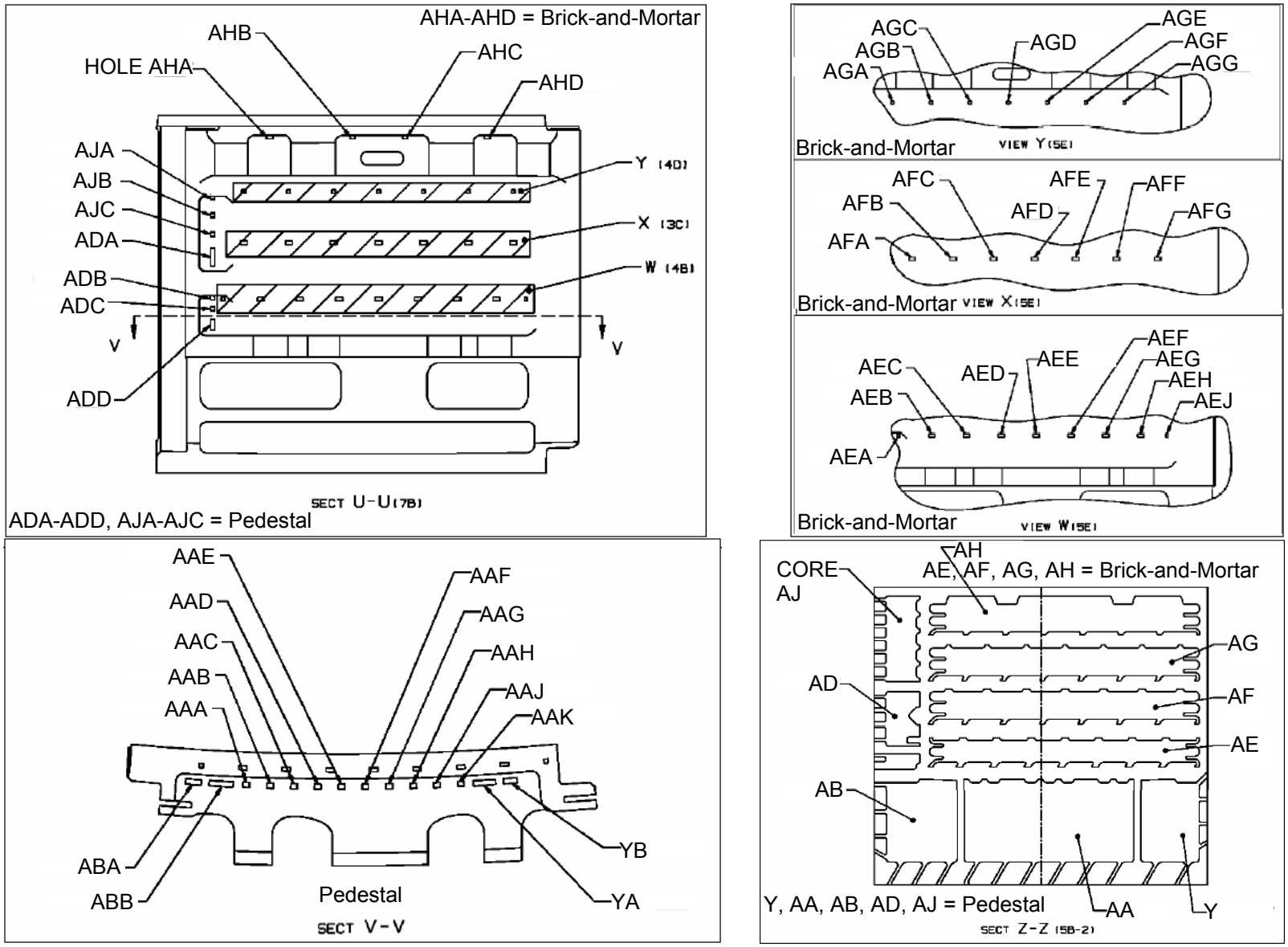

Figure 2.9. Pratt & Whitney schematics of the microcircuit BOAS [2].

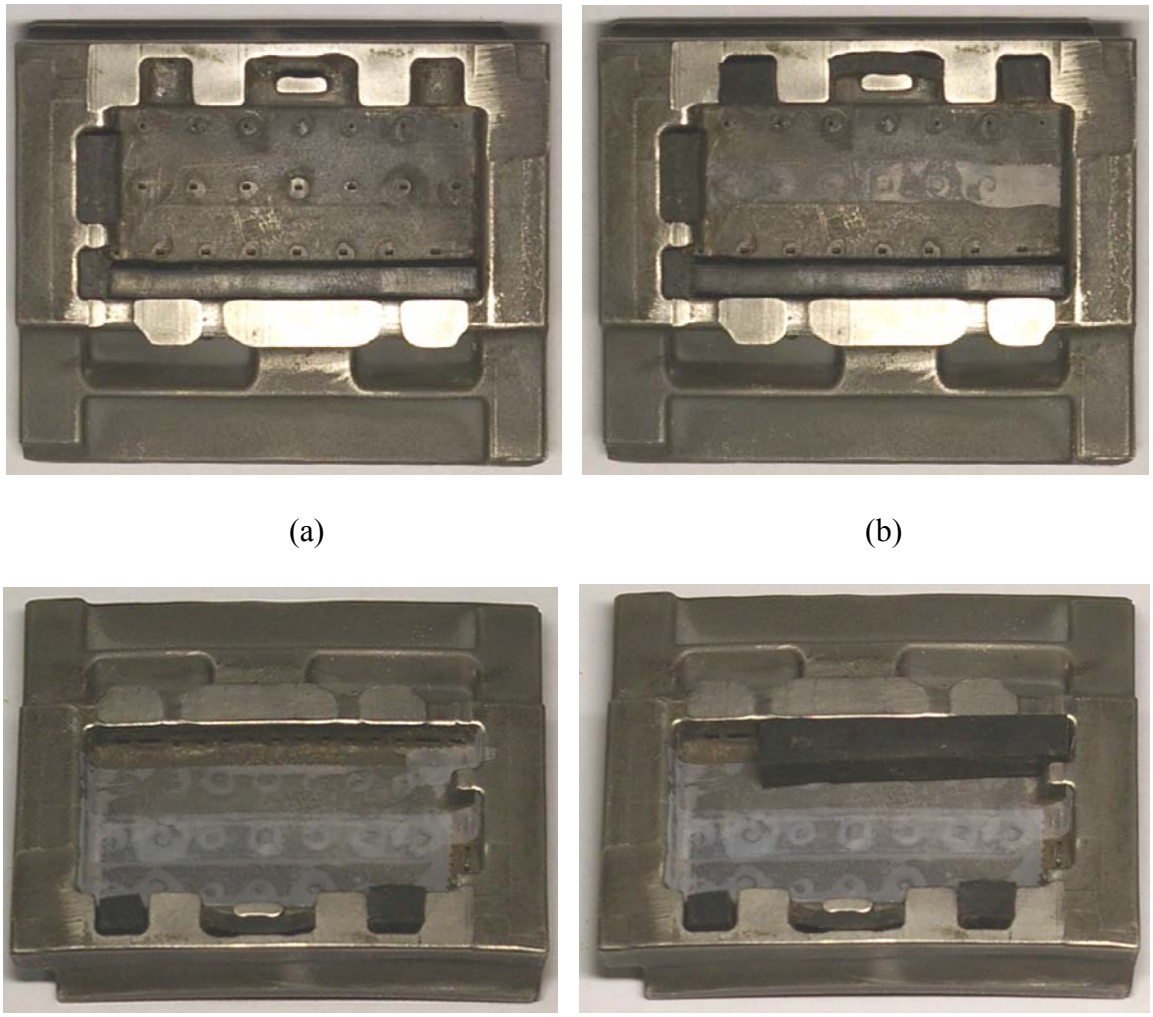

(a) (b)

(c) (d)

Figure 2.10. Tape and gasket material locations for passing coolant through the (a) brick-and-mortar forward, (b) brick-and-mortar aft, (c) pedestal forward, and (d) pedestal aft sections of the microcircuit BOAS.

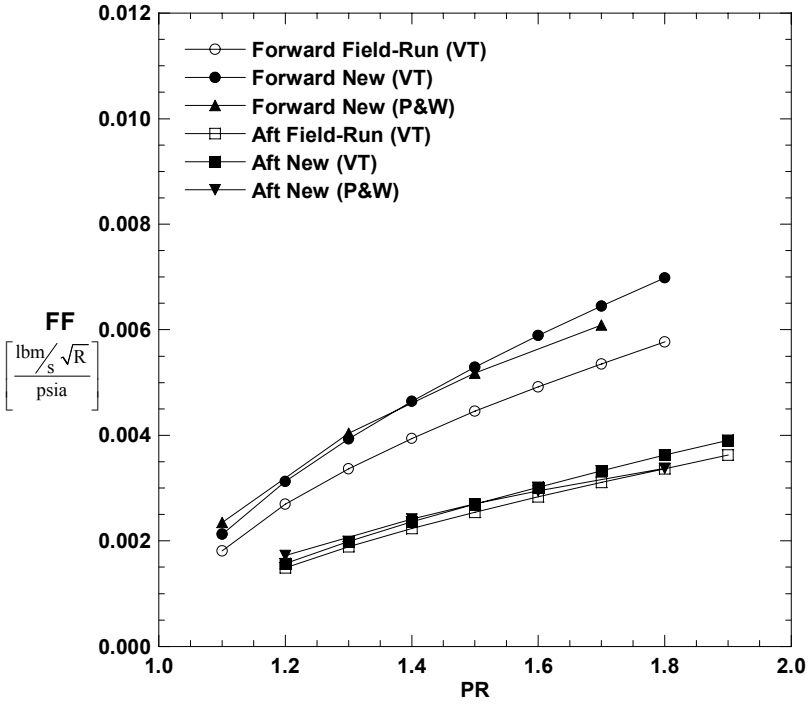

Figure 2.11. Baseline flow function versus pressure ratio including the P&W predictions for the BOAS with 0.014 inch film-cooling holes.

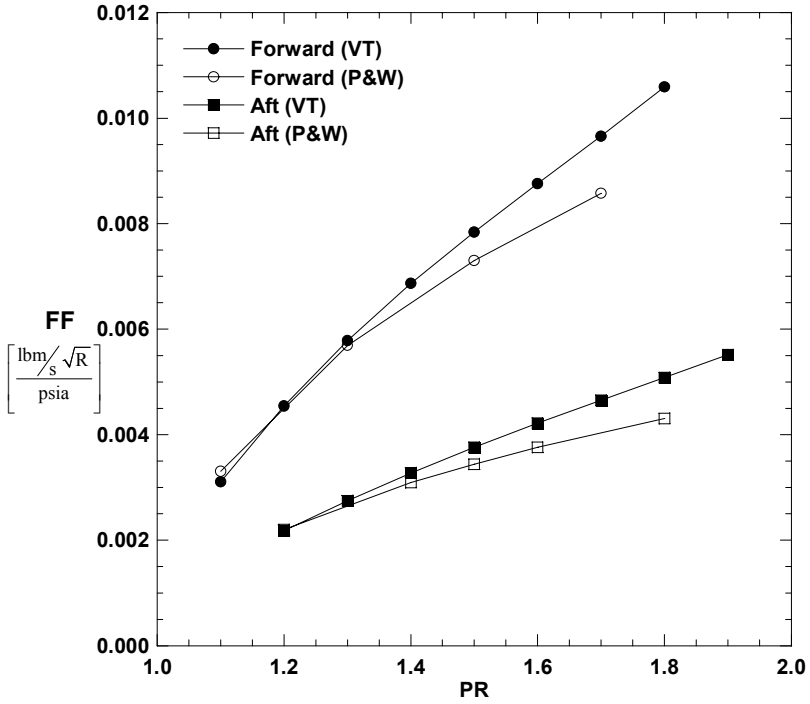

Figure 2.12. Baseline flow function versus pressure ratio including the P&W predictions for the BOAS with 0.019 inch film-cooling holes.

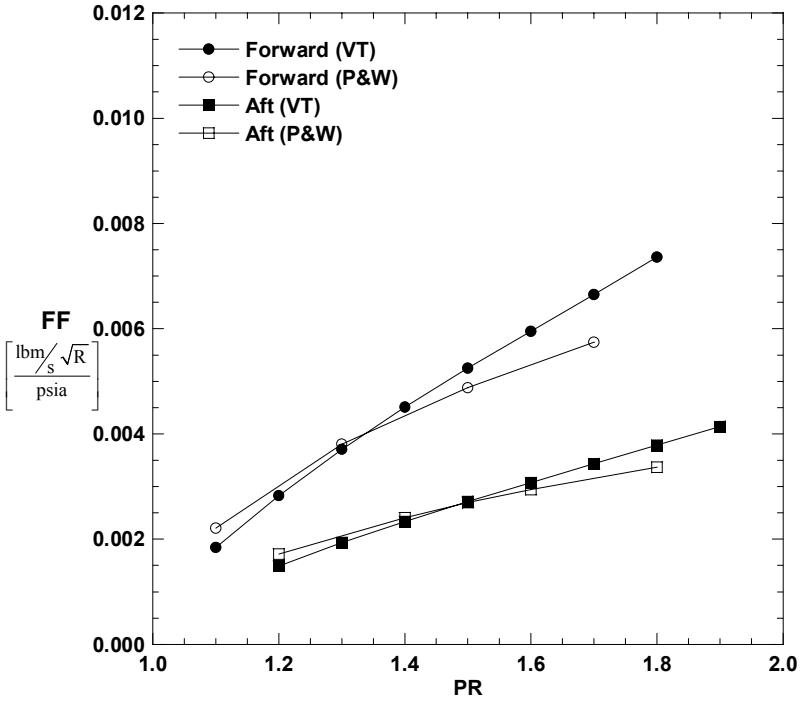

Figure 2.13. Baseline flow function versus pressure ratio including the P&W predictions for the brick-and-mortar geometry of the microcircuit BOAS.

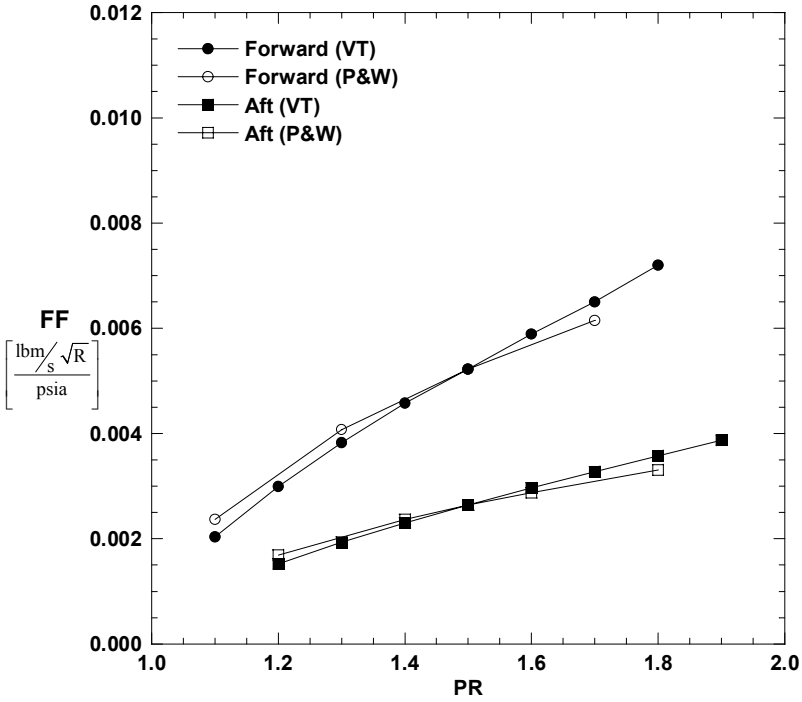

Figure 2.14. Baseline flow function versus pressure ratio including the P&W predictions for the pedestal geometry of the microcircuit BOAS.

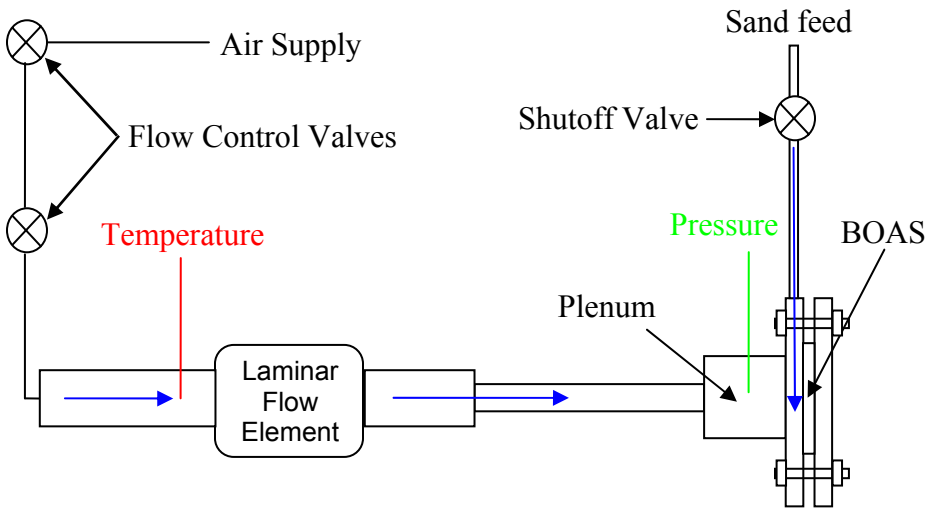

Figure 2.15. Test apparatus for supplying the sand-air mixture to the test coupon.

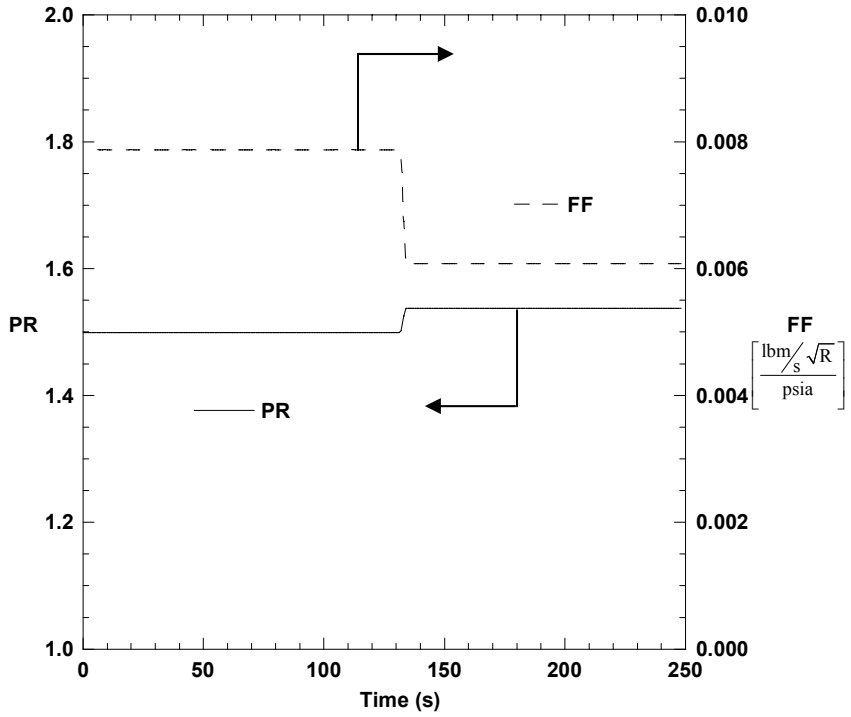

Figure 2.16. Pressure ratio and flow function versus time before and after sand is introduced (BOAS with 0.019 inch film-cooling holes, forward cavity, 0.42 grams, 0<D<0.15 inch sand).

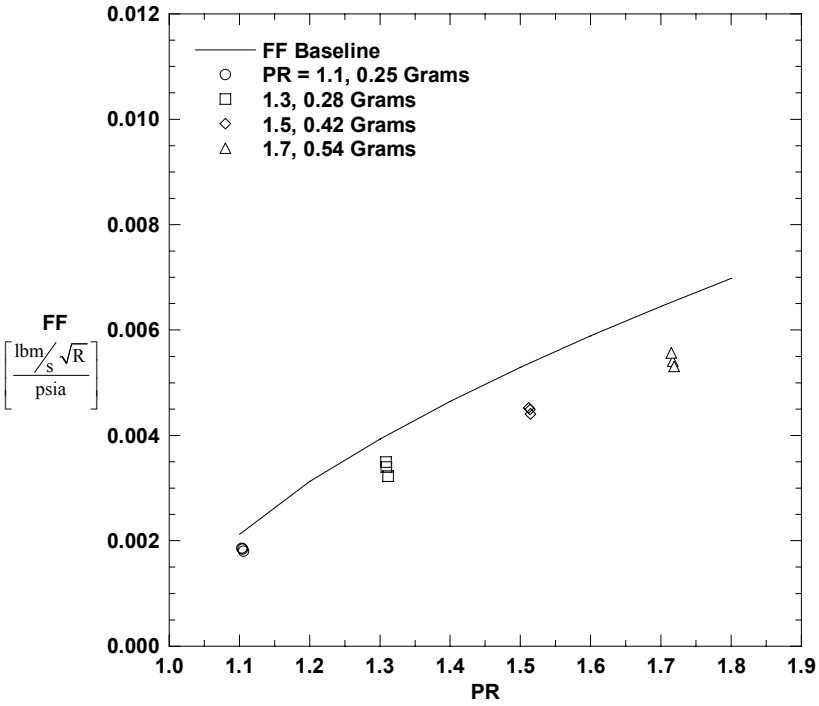

Figure 2.17. Flow parameter baseline and following repeated sand tests versus pressure ratio (new BOAS with 0.014 inch film-cooling holes, 0<D<0.15 inch sand).

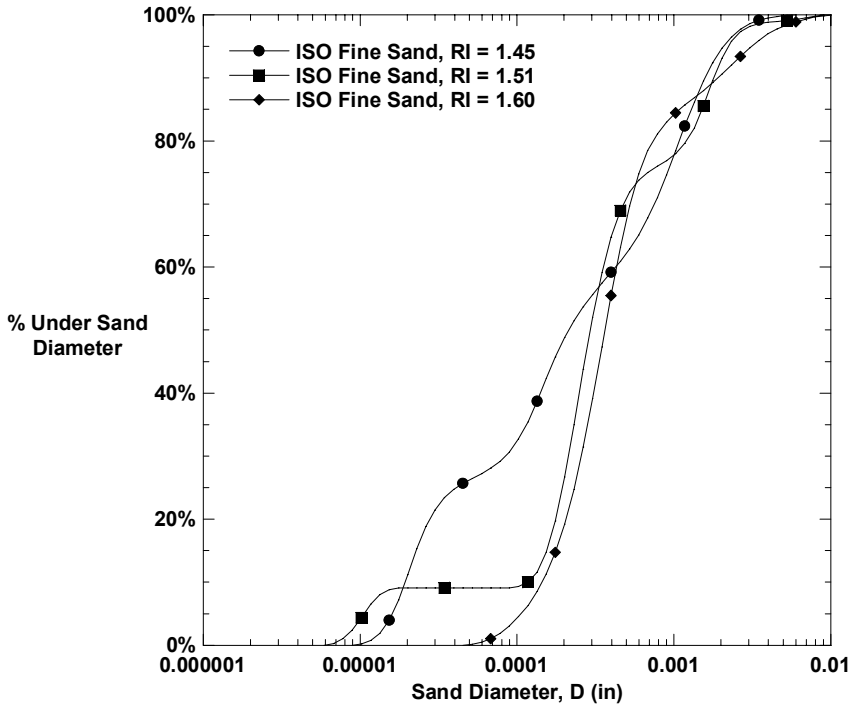

Figure 2.18. Percent of particles under sand diameter versus sand diameter for the ISO fine sand at three different refractive index real values.

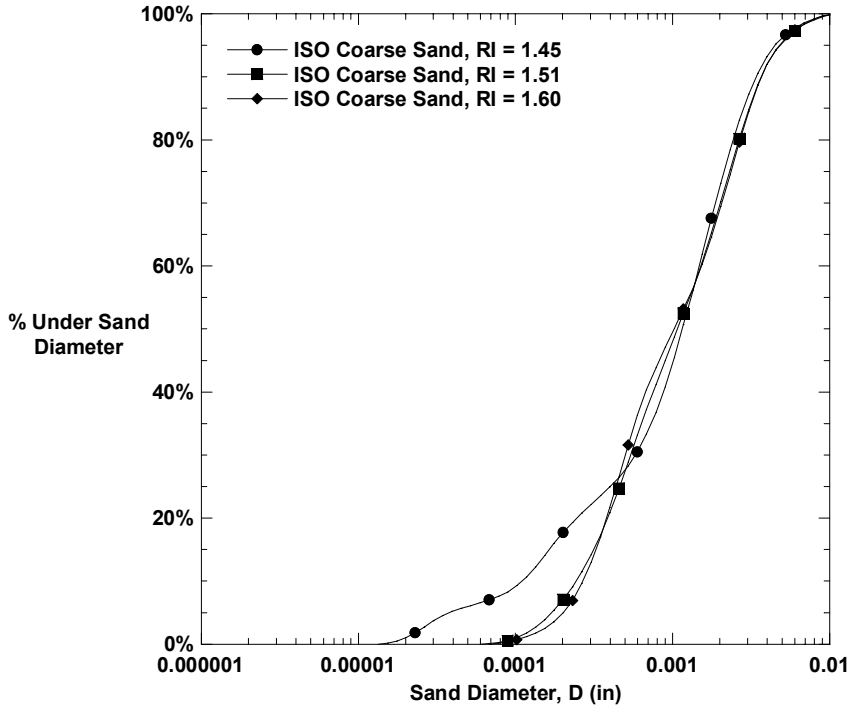

Figure 2.19. Percent of particles under sand diameter versus sand diameter for the ISO coarse sand at three different refractive index real values.

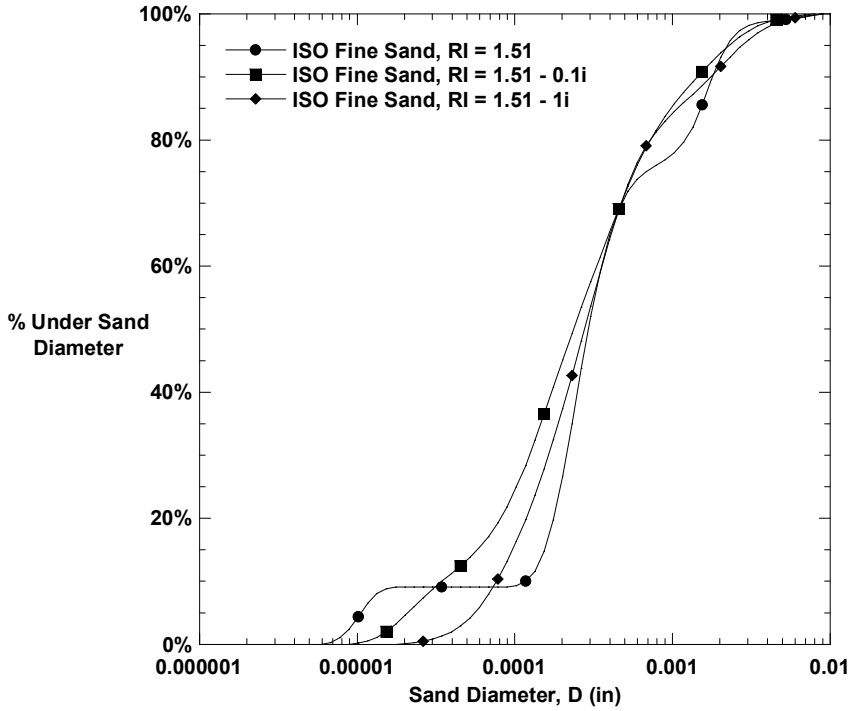

Figure 2.20. Percent of particles under sand diameter versus sand diameter for the ISO fine sand at three different refractive index imaginary values.

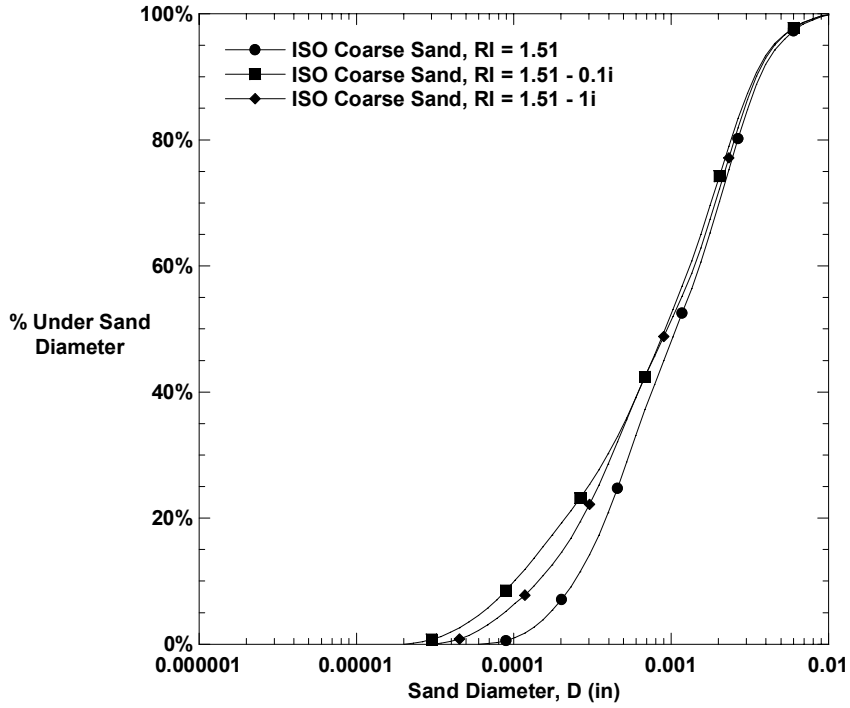

Figure 2.21. Percent of particles under sand diameter versus sand diameter for the ISO coarse sand at three different refractive index imaginary values.

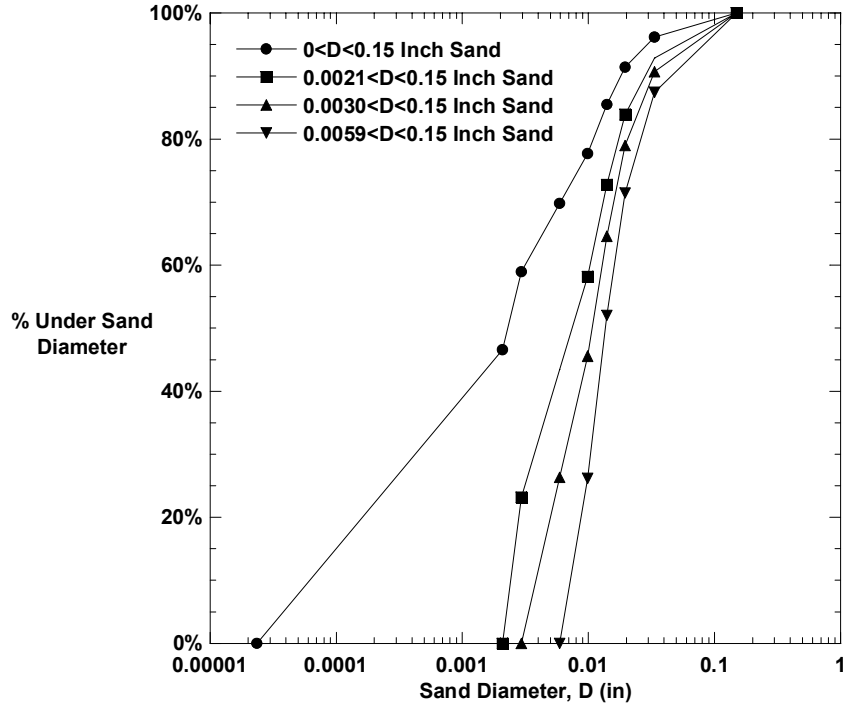

Figure 2.22. Percent of particles under sand diameter versus sand diameter for the four test sands.

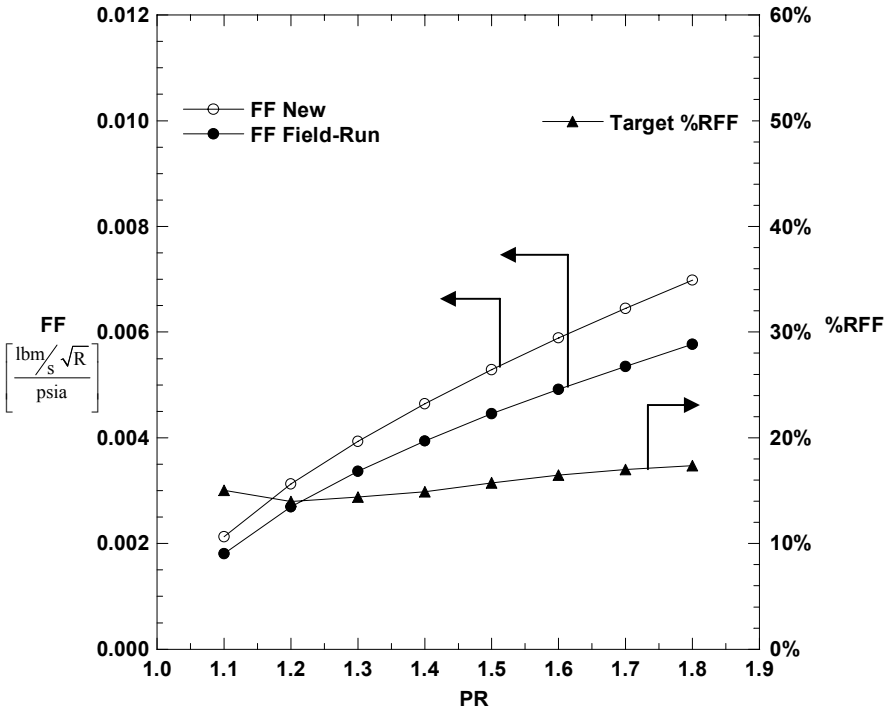

Figure 2.23. Flow function and percent reduction in flow function versus pressure ratio for the forward flow cavity of the new BOAS with 0.014 inch film-cooling holes compared to the field-run BOAS.

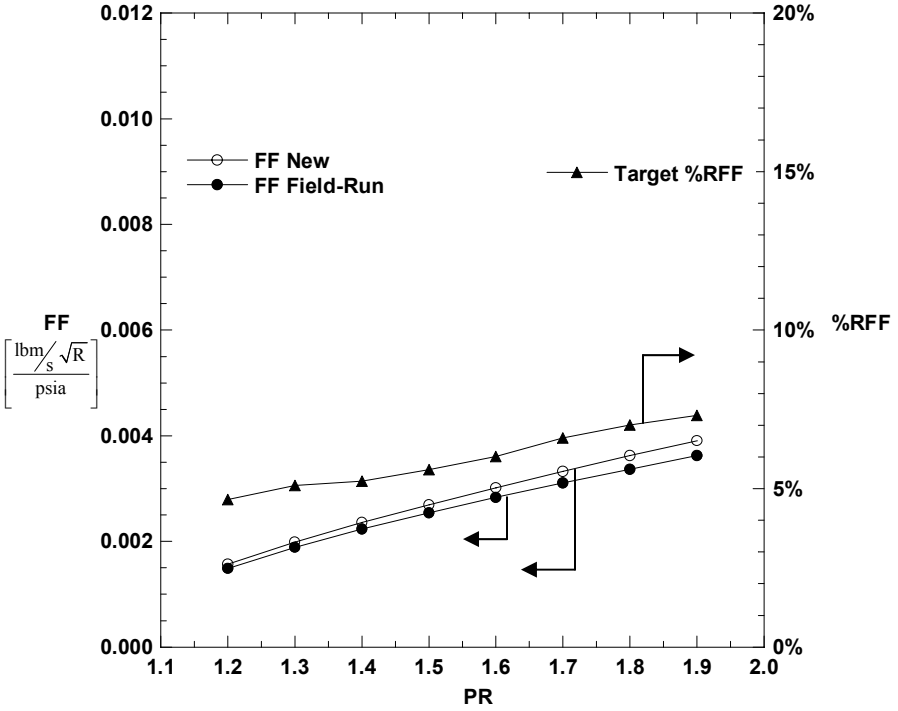

Figure 2.24. Flow function and percent reduction in flow function versus pressure ratio for the aft flow cavity of the new BOAS with 0.014 inch film-cooling holes compared to the field-run BOAS.

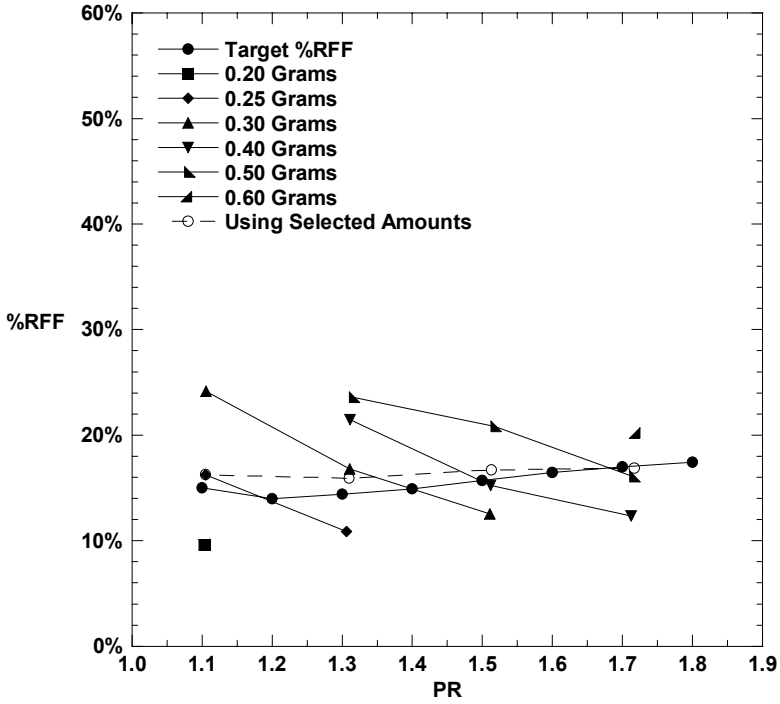

Figure 2.25. Percent reduction in flow function versus pressure ratio for a range of sand amounts (new BOAS with 0.014 inch film-cooling holes, forward flow section, 0<D<0.15 inch sand).

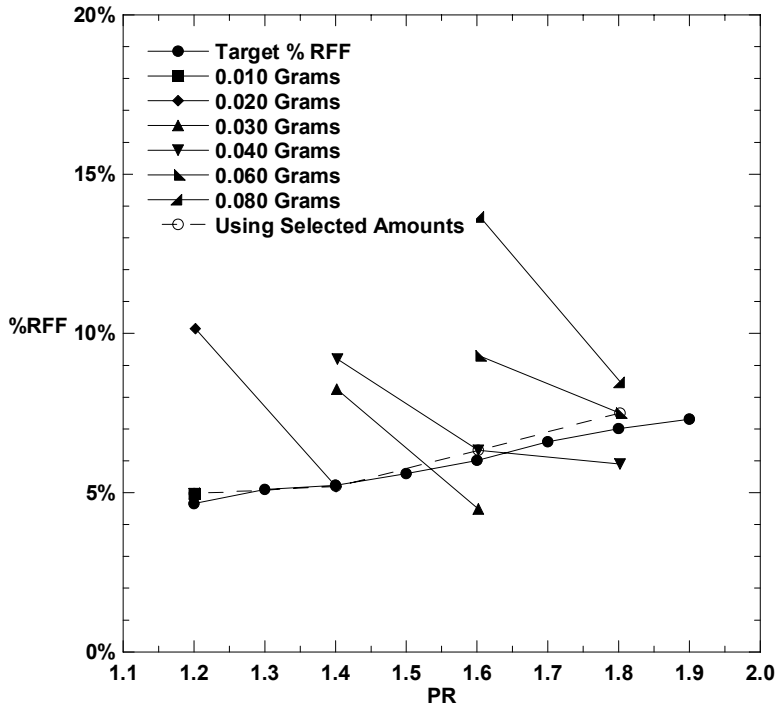

Figure 2.26. Percent reduction in flow function versus pressure ratio for a range of sand amounts (new BOAS with 0.014 inch film-cooling holes, aft flow section, 0<D<0.15 inch sand).

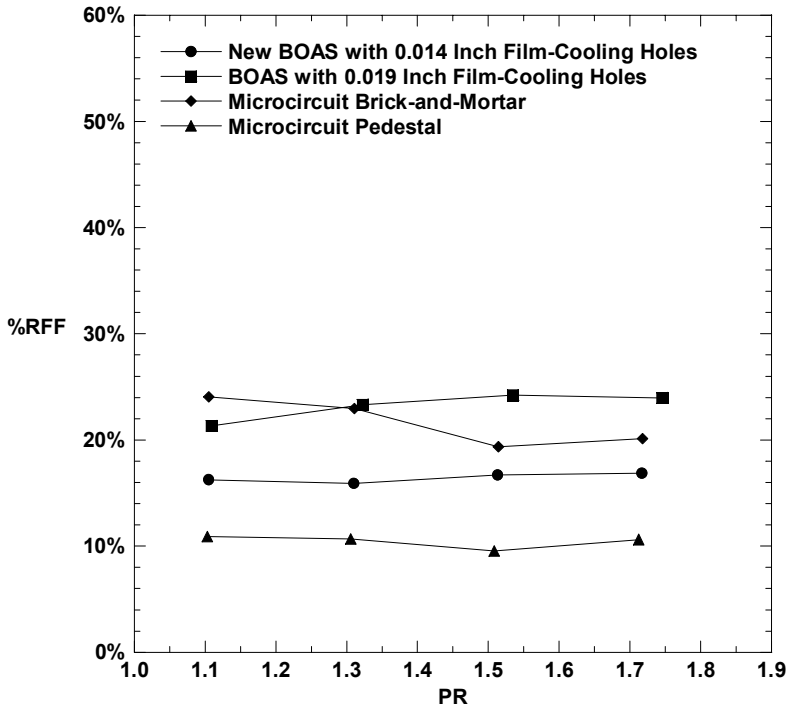

Figure 2.27. Percent reduction in flow function versus pressure ratio for the different BOAS geometries (forward flow section, 0<D<0.15 inch sand).

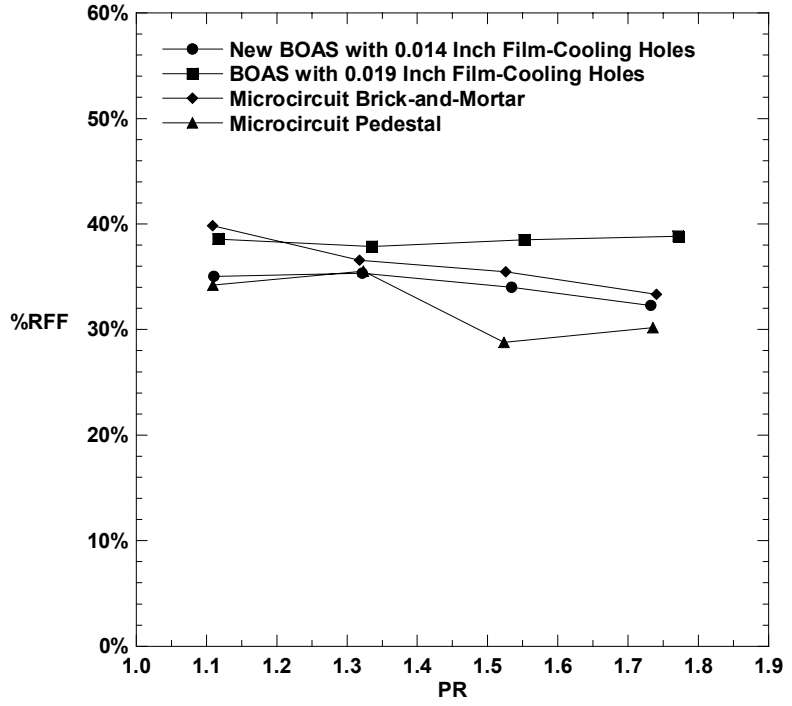

Figure 2.28. Percent reduction in flow function versus pressure ratio for the different BOAS geometries (forward flow section, 0.0021<D<0.15 inch sand).

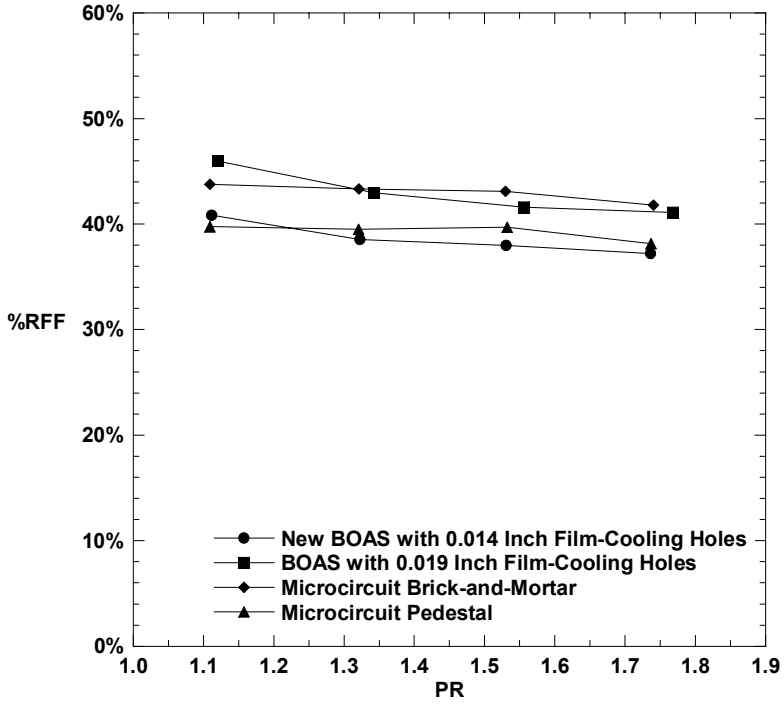

Figure 2.29. Percent reduction in flow function versus pressure ratio for the different BOAS geometries (forward flow section, 0.0030<D<0.15 inch sand).

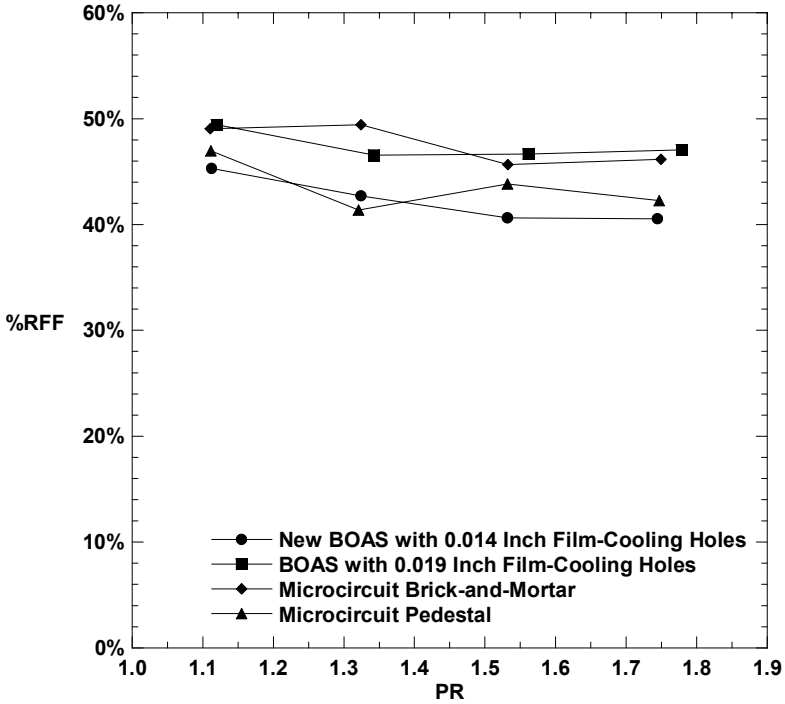

Figure 2.30. Percent reduction in flow function versus pressure ratio for the different BOAS geometries (forward flow section, 0.0059<D<0.15 inch sand).

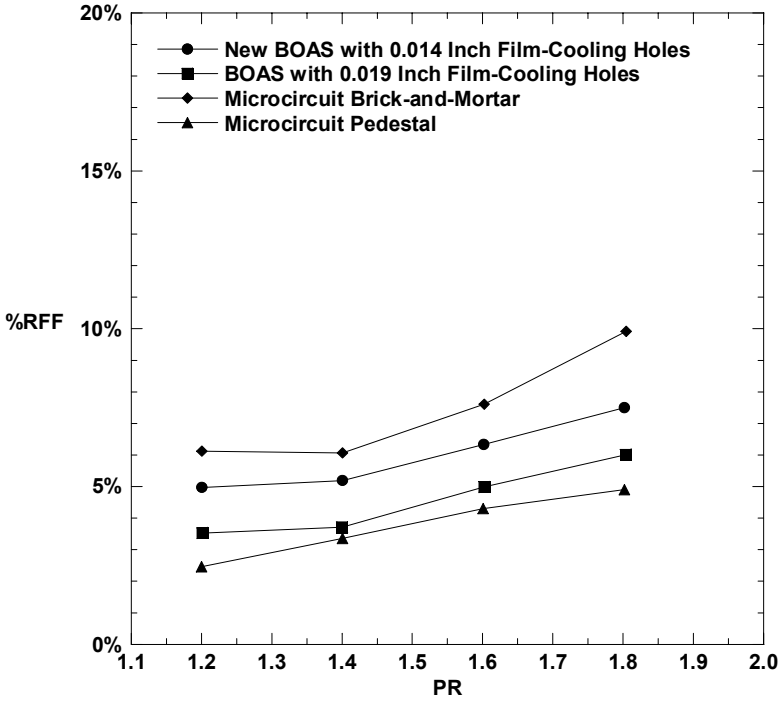

Figure 2.31. Percent reduction in flow function versus pressure ratio for the different BOAS geometries (aft flow section, 0<D<0.15 inch sand).

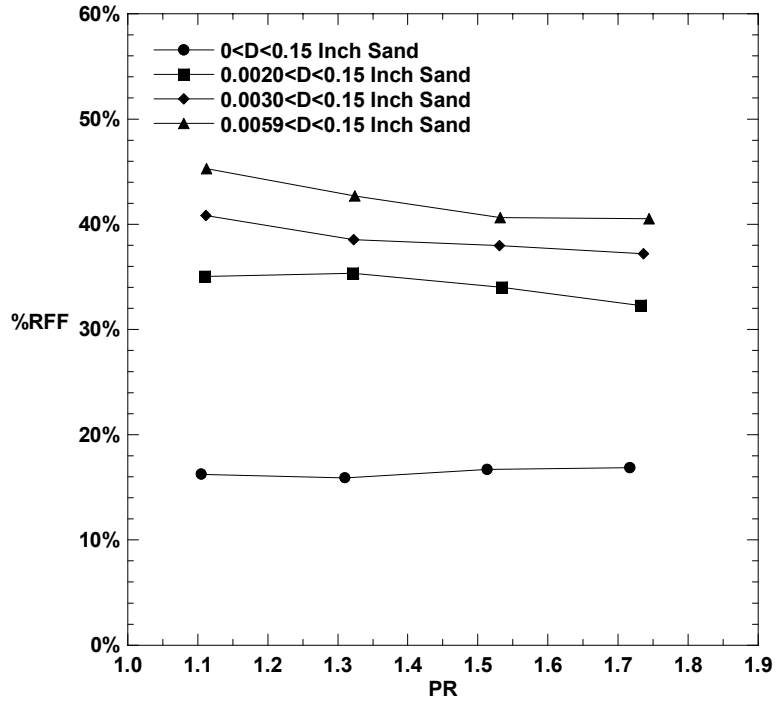

Figure 2.32. Percent reduction in flow function versus pressure ratio for the different sand diameter distributions (new BOAS with 0.014 inch film-cooling holes, forward flow section).

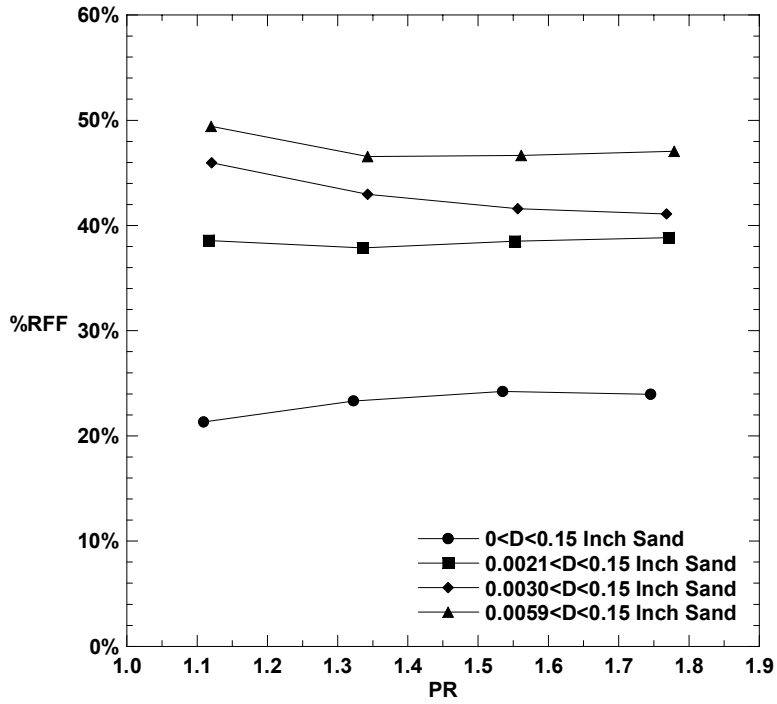

Figure 2.33. Percent reduction in flow function versus pressure ratio for the different sand diameter distributions (BOAS with 0.019 inch film-cooling holes, forward flow section).

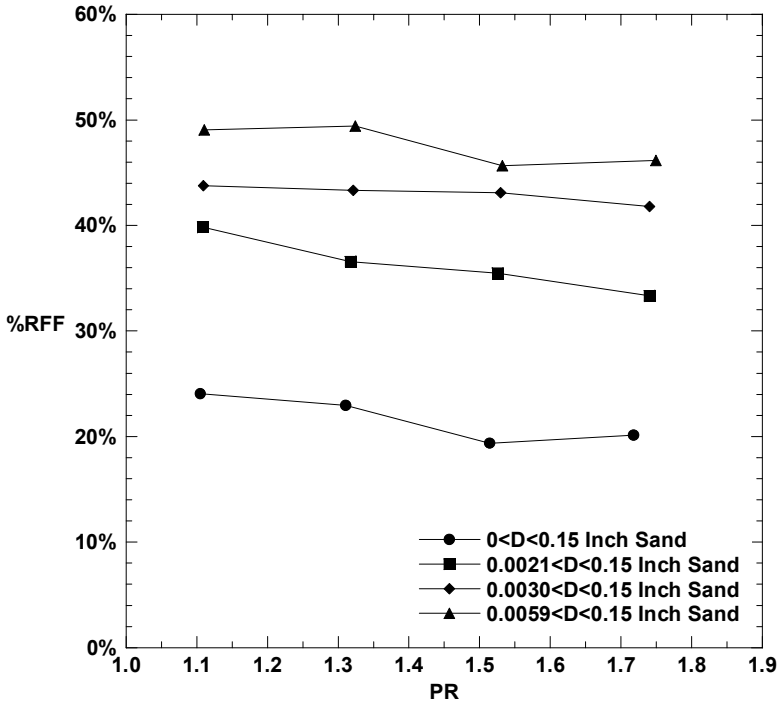

Figure 2.34. Percent reduction in flow function versus pressure ratio for the different sand diameter distributions (microcircuit brick-and-mortar, forward flow section).

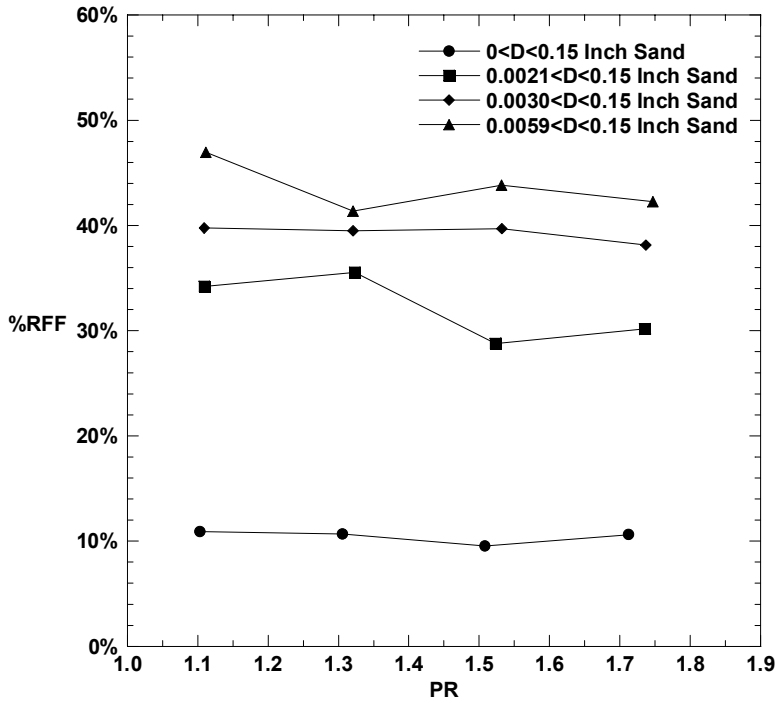

Figure 2.35. Percent reduction in flow function versus pressure ratio for the different sand diameter distributions (microcircuit pedestal, forward flow section).

Appendix A:

Sample Calculations for Part II

Presented in this appendix are sample calculations for Part II of this thesis. Tables A.1-A.5 contain sample calculations for the test parameters from Part II. The sample data are for tests following sand injection for the forward and aft flow sections of the new BOAS with 0.014 inch film-cooling holes, the BOAS with 0.019 inch film-cooling holes, the microcircuit brick-and-mortar BOAS, and the microcircuit pedestal BOAS. The conditions for all of the forward trials are at a starting PR = 1.3 and 0.28 grams of 0-0.15 inch sand. The conditions for all of the aft trials are at a starting PR = 1.4 and 0.020 grams of 0-0.15 inch sand.

Table A.1. Sample Calculation for the Dynamic Viscosity of the Coolant, μ_C

		New BOAS with 0.014 Inch Film-Cooling Holes		BOAS with 0.019 Inch Film-Cooling Holes	
Variable	**Units**	**Forward**	**Aft**	**Forward**	**Aft**
μ_C	micropoise	182.7	183.4	183.2	182.6
b	$\frac{\text{micropoise}}{\text{R}^{0.5}}$	14.58	14.58	14.58	14.58
S	R	110.4	110.4	110.4	110.4
T_{0C}	R	532.8	535.3	534.8	532.5
		Microcircuit Brick-and-Mortar		**Microcircuit Pedestal**	
Variable	**Units**	**Forward**	**Aft**	**Forward**	**Aft**
μ_C	micropoise	182.6	182.3	182.9	182.5
b	$\frac{\text{micropoise}}{\text{R}^{0.5}}$	14.58	14.58	14.58	14.58
S	R	110.4	110.4	110.4	110.4
T_{0C}	R	532.5	531.3	533.4	531.9

Table A.2. Sample Calculation for the Mass Flow, $\dot{m}$

		New BOAS with 0.014 Inch Film-Cooling Holes		BOAS with 0.019 Inch Film-Cooling Holes	
Variable	**Units**	**Forward**	**Aft**	**Forward**	**Aft**
$\dot{m}$	lbm/s	0.002073	0.001295	0.002794	0.001899
B	$\frac{lbm/s}{inH_2O}$	0.4142	0.4142	0.4142	0.4142
ΔP	inH_2O	3.410	2.021	4.640	2.915
C	$\frac{lbm/s}{inH_2O^2}$	-0.004142	-0.004142	-0.004142	-0.004142
μ_{std}	micropoise	181.9	181.9	181.9	181.9
μ_C	micropoise	182.7	183.4	183.2	182.6
P_{0LFE}	psia	18.08	18.95	18.26	19.25
P_{std}	psia	14.70	14.70	14.70	14.70
T_{std}	R	529.7	529.7	529.7	529.7
T_{0C}	R	532.8	535.3	534.8	532.5
ρ_{std}	lbm/ft^3	0.07490	0.07490	0.07490	0.07490
		Microcircuit Brick-and-Mortar		**Microcircuit Pedestal**	
Variable	**Units**	**Forward**	**Aft**	**Forward**	**Aft**
$\dot{m}$	lbm/s	0.001768	0.001312	0.001997	0.001324
B	$\frac{lbm/s}{inH_2O}$	0.4142	0.4142	0.4142	0.4142
ΔP	inH_2O	2.872	1.978	3.308	1.996
C	$\frac{lbm/s}{inH_2O^2}$	-0.004142	-0.004142	-0.004142	-0.004142
μ_{std}	micropoise	181.9	181.9	181.9	181.9
μ_C	micropoise	182.6	182.3	182.9	182.5
P_{0LFE}	psia	18.19	19.33	17.96	19.37
P_{std}	psia	14.70	14.70	14.70	14.70
T_{std}	R	529.7	529.7	529.7	529.7
T_{0C}	R	532.5	531.3	533.4	531.9
ρ_{std}	lbm/ft^3	0.07490	0.07490	0.07490	0.07490

Table A.3. Sample Calculation for the Flow Function, FF

		New BOAS with 0.014 Inch Film-Cooling Holes		BOAS with 0.019 Inch Film-Cooling Holes	
Variable	**Units**	**Forward**	**Aft**	**Forward**	**Aft**
FF	$\frac{\text{lbm } R^{0.5}}{\text{s psia}}$	0.003495	0.002228	0.004735	0.003209
$\dot{m}$	lbm/s	0.002073	0.001295	0.002794	0.001899
T_{0C}	R	532.8	535.3	534.8	532.5
P_∞	psia	13.69	13.45	13.65	13.65
		Microcircuit Brick-and-Mortar		**Microcircuit Pedestal**	
Variable	**Units**	**Forward**	**Aft**	**Forward**	**Aft**
FF	$\frac{\text{lbm } R^{0.5}}{\text{s psia}}$	0.002961	0.002201	0.003384	0.002216
$\dot{m}$	lbm/s	0.001768	0.001312	0.001997	0.001324
T_{0C}	R	532.5	531.3	533.4	531.9
P_∞	psia	13.78	13.74	13.63	13.78

Table A.4. Sample Calculation for the Percent Reduction in Flow Function, %RFF

		New BOAS with 0.014 Inch Film-Cooling Holes		BOAS with 0.019 Inch Film-Cooling Holes	
Variable	**Units**	**Forward**	**Aft**	**Forward**	**Aft**
%RFF		12.67%	5.708%	21.38%	2.063%
FF	$\frac{\text{lbm } R^{0.5}}{\text{s psia}}$	0.003495	0.002228	0.004735	0.003209
FF_0	$\frac{\text{lbm } R^{0.5}}{\text{s psia}}$	0.004003	0.002363	0.006023	0.003276
		Microcircuit Brick-and-Mortar		**Microcircuit Pedestal**	
Variable	**Units**	**Forward**	**Aft**	**Forward**	**Aft**
%RFF		22.04%	5.979%	12.77%	3.640%
FF	$\frac{\text{lbm } R^{0.5}}{\text{s psia}}$	0.002961	0.002201	0.003384	0.002216
FF_0	$\frac{\text{lbm } R^{0.5}}{\text{s psia}}$	0.003798	0.002341	0.003880	0.002299

Table A.5. Sample Calculation for the Pressure Ratio, PR

		New BOAS with 0.014 Inch Film-Cooling Holes		BOAS with 0.019 Inch Film-Cooling Holes	
Variable	**Units**	**Forward**	**Aft**	**Forward**	**Aft**
PR		1.309	1.401	1.321	1.400
P_{0C}	psia	17.92	18.85	18.02	19.12
P_{∞}	psia	13.69	13.45	13.65	13.65
		Microcircuit Brick-and-Mortar		**Microcircuit Pedestal**	
Variable	**Units**	**Forward**	**Aft**	**Forward**	**Aft**
PR		1.310	1.401	1.306	1.400
P_{0C}	psia	18.06	19.24	17.80	19.29
P_{∞}	psia	13.78	13.74	13.63	13.78

Appendix B:

Relevant Data for Part II

Given in this appendix is the relevant data for Part II of this thesis. Tables B.1-B.100 contain the data from all testing conducted using the BOAS parts supplied by Pratt & Whitney.

Table B.1. New BOAS with 0.014 Inch Film-Cooling Holes (2A3515), Forward, 0<D<0.15 Inch Sand, 0.20 Grams, PR 1.1

Run #	P_{atm} (psia)	P_{0C} (psia)	PR	FF (lbm*√R/s/psia)	FF_0 (lbm*√R/s/psia)	%RFF
1	13.66	15.07	1.10	0.00195	0.00217	9.92%
2	13.66	15.08	1.10	0.00200	0.00218	8.38%
3	13.66	15.07	1.10	0.00194	0.00217	10.5%
Average	13.66	15.07	1.10	0.00196	0.00217	9.61%

Table B.2. New BOAS with 0.014 Inch Film-Cooling Holes (2A3515), Forward, 0<D<0.15 Inch Sand, 0.25 Grams, PR 1.3

Run #	P_{atm} (psia)	P_{0C} (psia)	PR	FF (lbm*√R/s/psia)	FF_0 (lbm*√R/s/psia)	%RFF
1	13.66	17.83	1.31	0.00363	0.00397	8.73%
2	13.66	17.85	1.31	0.00357	0.00398	10.3%
3	13.66	17.86	1.31	0.00345	0.00399	13.6%
Average	13.66	17.85	1.31	0.00355	0.00398	10.9%

Table B.3. New BOAS with 0.014 Inch Film-Cooling Holes (2A3515), Forward, 0<D<0.15 Inch Sand, 0.30 Grams, PR 1.1

Run #	P_{atm} (psia)	P_{0C} (psia)	PR	FF (lbm*√R/s/psia)	FF_0 (lbm*√R/s/psia)	%RFF
1	13.71	15.13	1.10	0.00171	0.00218	21.6%
2	13.71	15.21	1.11	0.00162	0.00223	27.4%
3	13.71	15.16	1.11	0.00168	0.00220	23.6%
Average	13.71	15.17	1.11	0.00167	0.00221	24.2%

Table B.4. New BOAS with 0.014 Inch Film-Cooling Holes (2A3515), Forward, 0<D<0.15 Inch Sand, 0.30 Grams, PR 1.3

Run #	P_{atm} (psia)	P_{0C} (psia)	PR	FF (lbm*√R/s/psia)	FF_0 (lbm*√R/s/psia)	%RFF
1	13.71	17.95	1.31	0.00330	0.00401	17.7%
2	13.67	17.93	1.31	0.00334	0.00402	16.9%
3	13.67	17.91	1.31	0.00338	0.00401	15.7%
Average	13.68	17.93	1.31	0.00334	0.00401	16.8%

Table B.5. New BOAS with 0.014 Inch Film-Cooling Holes (2A3515), Forward, 0<D<0.15 Inch Sand, 0.30 Grams, PR 1.5

Run #	P_{atm} (psia)	P_{0C} (psia)	PR	FF (lbm*√R/s/psia)	FF_0 (lbm*√R/s/psia)	%RFF
1	13.67	20.66	1.51	0.00470	0.00536	12.3%
2	13.67	20.62	1.51	0.00486	0.00534	9.08%
3	13.67	20.71	1.51	0.00451	0.00538	16.2%
Average	13.67	20.66	1.51	0.00469	0.00536	12.5%

Table B.6. New BOAS with 0.014 Inch Film-Cooling Holes (2A3515), Forward, 0<D<0.15 Inch Sand, 0.40 Grams, PR 1.3

Run #	P_{atm} (psia)	P_{0C} (psia)	PR	FF (lbm*√R/s/psia)	FF_0 (lbm*√R/s/psia)	%RFF
1	13.73	18.05	1.31	0.00306	0.00405	24.5%
2	13.73	17.99	1.31	0.00317	0.00401	21.0%
3	13.73	17.98	1.31	0.00325	0.00401	18.9%
Average	13.73	18.01	1.31	0.00316	0.00402	21.5%

Table B.7. New BOAS with 0.014 Inch Film-Cooling Holes (2A3515), Forward, 0<D<0.15 Inch Sand, 0.40 Grams, PR 1.5

Run #	P_{atm} (psia)	P_{0C} (psia)	PR	FF (lbm*√R/s/psia)	FF_0 (lbm*√R/s/psia)	%RFF
1	13.72	20.72	1.51	0.00463	0.00536	13.7%
2	13.72	20.74	1.51	0.00457	0.00537	14.8%
3	13.72	20.77	1.51	0.00445	0.00538	17.3%
Average	13.72	20.74	1.51	0.00455	0.00537	15.3%

Table B.8. New BOAS with 0.014 Inch Film-Cooling Holes (2A3515), Forward, 0<D<0.15 Inch Sand, 0.40 Grams, PR 1.7

Run #	P_{atm} (psia)	P_{0C} (psia)	PR	FF (lbm*√R/s/psia)	FF_0 (lbm*√R/s/psia)	%RFF
1	13.68	23.42	1.71	0.00576	0.00651	11.5%
2	13.68	23.45	1.71	0.00564	0.00652	13.5%
3	13.68	23.42	1.71	0.00573	0.00651	12.0%
Average	13.68	23.43	1.71	0.00571	0.00651	12.3%

Table B.9. New BOAS with 0.014 Inch Film-Cooling Holes (2A3515), Forward, 0<D<0.15 Inch Sand, 0.50 Grams, PR 1.3

Run #	P_{atm} (psia)	P_{0C} (psia)	PR	FF (lbm*√R/s/psia)	FF_0 (lbm*√R/s/psia)	%RFF
1	13.76	18.04	1.31	0.00326	0.00402	18.9%
2	13.76	18.14	1.32	0.00296	0.00407	27.4%
3	13.75	18.08	1.32	0.00306	0.00405	24.5%
Average	13.76	18.09	1.31	0.00309	0.00405	23.6%

Table B.10. New BOAS with 0.014 Inch Film-Cooling Holes (2A3515), Forward, 0<D<0.15 Inch Sand, 0.50 Grams, PR 1.5

Run #	P_{atm} (psia)	P_{0C} (psia)	PR	FF (lbm*√R/s/psia)	FF_0 (lbm*√R/s/psia)	%RFF
1	13.74	20.85	1.52	0.00439	0.00540	18.7%
2	13.73	20.85	1.52	0.00429	0.00541	20.6%
3	13.72	20.83	1.52	0.00415	0.00540	23.1%
Average	13.73	20.84	1.52	0.00428	0.00540	20.8%

Table B.11. New BOAS with 0.014 Inch Film-Cooling Holes (2A3515), Forward, 0<D<0.15 Inch Sand, 0.50 Grams, PR 1.7

Run #	P_{atm} (psia)	P_{0C} (psia)	PR	FF (lbm*√R/s/psia)	FF_0 (lbm*√R/s/psia)	%RFF
1	13.72	23.54	1.72	0.00549	0.00652	15.8%
2	13.72	23.54	1.71	0.00557	0.00652	14.6%
3	13.72	23.57	1.72	0.00537	0.00653	17.8%
Average	13.72	23.55	1.72	0.00548	0.00653	16.1%

Table B.12. New BOAS with 0.014 Inch Film-Cooling Holes (2A3515), Forward, 0<D<0.15 Inch Sand, 0.60 Grams, PR 1.7

Run #	P_{atm} (psia)	P_{0C} (psia)	PR	FF (lbm*√R/s/psia)	FF_0 (lbm*√R/s/psia)	%RFF
1	13.66	23.50	1.72	0.00525	0.00655	19.9%
2	13.66	23.53	1.72	0.00502	0.00657	23.6%
3	13.66	23.46	1.72	0.00541	0.00654	17.2%
Average	13.66	23.50	1.72	0.00523	0.00655	20.2%

Table B.13. New BOAS with 0.014 Inch Film-Cooling Holes (2A3515), Forward, 0<D<0.15 Inch Sand, 0.25 Grams, PR 1.1

Run #	P_{atm} (psia)	P_{0C} (psia)	PR	FF (lbm*√R/s/psia)	FF_0 (lbm*√R/s/psia)	%RFF
1	13.66	15.09	1.11	0.00185	0.00219	15.8%
2	13.66	15.08	1.10	0.00186	0.00218	14.6%
3	13.66	15.11	1.11	0.00180	0.00220	18.3%
Average	13.66	15.09	1.11	0.00184	0.00219	16.2%

Table B.14 New BOAS with 0.014 Inch Film-Cooling Holes (2A3515), Forward, 0<D<0.15 Inch Sand, 0.28 Grams, PR 1.3

Run #	P_{atm} (psia)	P_{0C} (psia)	PR	FF (lbm*√R/s/psia)	FF_0 (lbm*√R/s/psia)	%RFF
1	13.69	17.92	1.31	0.00350	0.00400	12.7%
2	13.69	17.93	1.31	0.00340	0.00401	15.2%
3	13.69	17.96	1.31	0.00323	0.00403	19.8%
Average	13.69	17.94	1.31	0.00337	0.00401	15.9%

Table B.15. New BOAS with 0.014 Inch Film-Cooling Holes (2A3515), Forward, 0<D<0.15 Inch Sand, 0.42 Grams, PR 1.5

Run #	P_{atm} (psia)	P_{0C} (psia)	PR	FF (lbm*√R/s/psia)	FF_0 (lbm*√R/s/psia)	%RFF
1	13.70	20.74	1.51	0.00450	0.00538	16.5%
2	13.70	20.74	1.51	0.00441	0.00538	18.1%
3	13.70	20.71	1.51	0.00453	0.00537	15.7%
Average	13.70	20.73	1.51	0.00448	0.00538	16.7%

Table B.16. New BOAS with 0.014 Inch Film-Cooling Holes (2A3515), Forward, 0<D<0.15 Inch Sand, 0.54 Grams, PR 1.7

Run #	P_{atm} (psia)	P_{0C} (psia)	PR	FF (lbm*√R/s/psia)	FF_0 (lbm*√R/s/psia)	%RFF
1	13.72	23.56	1.72	0.00541	0.00653	17.1%
2	13.72	23.52	1.71	0.00557	0.00652	14.6%
3	13.72	23.58	1.72	0.00531	0.00654	18.8%
Average	13.72	23.55	1.72	0.00543	0.00653	16.9%

Table B.17. New BOAS with 0.014 Inch Film-Cooling Holes (2A3515), Aft, 0<D<0.15 Inch Sand, 0.010 Grams, PR 1.2

Run #	P_{atm} (psia)	P_{0C} (psia)	PR	FF (lbm*√R/s/psia)	FF_0 (lbm*√R/s/psia)	%RFF
1	13.44	16.14	1.20	0.00147	0.00157	6.38%
2	13.44	16.15	1.20	0.00154	0.00158	2.72%
3	13.44	16.14	1.20	0.00148	0.00157	5.81%
Average	13.44	16.14	1.20	0.00150	0.00158	4.97%

Table B.18. New BOAS with 0.014 Inch Film-Cooling Holes (2A3515), Aft, 0<D<0.15 Inch Sand, 0.020 Grams, PR 1.2

Run #	P_{atm} (psia)	P_{0C} (psia)	PR	FF (lbm*√R/s/psia)	FF_0 (lbm*√R/s/psia)	%RFF
1	13.44	16.13	1.20	0.00146	0.00158	7.38%
2	13.44	16.16	1.20	0.00142	0.00158	10.5%
3	13.44	16.16	1.20	0.00139	0.00158	12.6%
Average	13.44	16.15	1.20	0.00142	0.00158	10.2%

Table B.19. New BOAS with 0.014 Inch Film-Cooling Holes (2A3515), Aft, 0<D<0.15 Inch Sand, 0.020 Grams, PR 1.4

Run #	P_{atm} (psia)	P_{0C} (psia)	PR	FF (lbm*√R/s/psia)	FF_0 (lbm*√R/s/psia)	%RFF
1	13.45	18.85	1.40	0.00223	0.00236	5.71%
2	13.45	18.84	1.40	0.00225	0.00236	4.77%
3	13.45	18.85	1.40	0.00225	0.00236	4.86%
4	13.66	19.13	1.40	0.00224	0.00236	5.18%
5	13.66	19.15	1.40	0.00222	0.00236	6.24%
6	13.66	19.14	1.40	0.00226	0.00236	4.43%
Average	13.56	18.99	1.40	0.00224	0.00236	5.20%

Table B.20. New BOAS with 0.014 Inch Film-Cooling Holes (2A3515), Aft, 0<D<0.15 Inch Sand, 0.030 Grams, PR 1.4

Run #	P_{atm} (psia)	P_{0C} (psia)	PR	FF (lbm*√R/s/psia)	FF_0 (lbm*√R/s/psia)	%RFF
1	13.44	18.84	1.40	0.00220	0.00236	6.80%
2	13.44	18.83	1.40	0.00221	0.00236	6.36%
3	13.67	19.17	1.40	0.00209	0.00237	11.6%
Average	13.51	18.95	1.40	0.00217	0.00237	8.25%

Table B.21. New BOAS with 0.014 Inch Film-Cooling Holes (2A3515), Aft, 0<D<0.15 Inch Sand, 0.030 Grams, PR 1.6

Run #	P_{atm} (psia)	P_{0C} (psia)	PR	FF (lbm*√R/s/psia)	FF_0 (lbm*√R/s/psia)	%RFF
1	13.46	21.56	1.60	0.00294	0.00303	2.96%
2	13.46	21.56	1.60	0.00288	0.00303	4.96%
3	13.46	21.57	1.60	0.00286	0.00303	5.52%
Average	13.46	21.56	1.60	0.00289	0.00303	4.48%

Table B.22. New BOAS with 0.014 Inch Film-Cooling Holes (2A3515), Aft, 0<D<0.15 Inch Sand, 0.040 Grams, PR 1.4

Run #	P_{atm} (psia)	P_{0C} (psia)	PR	FF (lbm*√R/s/psia)	FF_0 (lbm*√R/s/psia)	%RFF
1	13.53	18.97	1.40	0.00217	0.00236	8.17%
2	13.53	18.98	1.40	0.00218	0.00237	7.94%
3	13.53	18.98	1.40	0.00210	0.00237	11.5%
Average	13.53	18.98	1.40	0.00215	0.00237	9.20%

Table B.23. New BOAS with 0.014 Inch Film-Cooling Holes (2A3515), Aft, 0<D<0.15 Inch Sand, 0.040 Grams, PR 1.6

Run #	P_{atm} (psia)	P_{0C} (psia)	PR	FF (lbm*√R/s/psia)	FF_0 (lbm*√R/s/psia)	%RFF
1	13.43	21.53	1.60	0.00281	0.00303	7.35%
2	13.43	21.51	1.60	0.00284	0.00303	6.19%
3	13.43	21.51	1.60	0.00285	0.00303	6.02%
4	13.55	21.69	1.60	0.00287	0.00303	5.31%
5	13.55	21.70	1.60	0.00286	0.00303	5.63%
6	13.55	21.72	1.60	0.00280	0.00303	7.51%
Average	13.49	21.61	1.60	0.00284	0.00303	6.34%

Table B.24. New BOAS with 0.014 Inch Film-Cooling Holes (2A3515), Aft, 0<D<0.15 Inch Sand, 0.040 Grams, PR 1.8

Run #	P_{atm} (psia)	P_{0C} (psia)	PR	FF (lbm*√R/s/psia)	FF_0 (lbm*√R/s/psia)	%RFF
1	13.46	24.26	1.80	0.00338	0.00363	6.86%
2	13.46	24.24	1.80	0.00348	0.00362	3.98%
3	13.46	24.25	1.80	0.00338	0.00363	6.88%
Average	13.46	24.25	1.80	0.00341	0.00363	5.91%

Table B.25. New BOAS with 0.014 Inch Film-Cooling Holes (2A3515), Aft, 0<D<0.15 Inch Sand, 0.060 Grams, PR 1.6

Run #	P_{atm} (psia)	P_{0C} (psia)	PR	FF (lbm*√R/s/psia)	FF_0 (lbm*√R/s/psia)	%RFF
1	13.54	21.70	1.60	0.00279	0.00303	7.94%
2	13.54	21.70	1.60	0.00275	0.00303	9.23%
3	13.54	21.73	1.60	0.00271	0.00304	10.7%
Average	13.54	21.71	1.60	0.00275	0.00303	9.30%

Table B.26. New BOAS with 0.014 Inch Film-Cooling Holes (2A3515), Aft, 0<D<0.15 Inch Sand, 0.060 Grams, PR 1.8

Run #	P_{atm} (psia)	P_{0C} (psia)	PR	FF (lbm*√R/s/psia)	FF_0 (lbm*√R/s/psia)	%RFF
1	13.43	24.19	1.80	0.00333	0.00363	8.21%
2	13.43	24.20	1.80	0.00330	0.00363	9.10%
3	13.43	24.18	1.80	0.00339	0.00362	6.36%
4	13.53	24.41	1.80	0.00327	0.00363	10.1%
5	13.53	24.39	1.80	0.00339	0.00363	6.52%
6	13.53	24.39	1.80	0.00346	0.00363	4.69%
Average	13.48	24.29	1.80	0.00336	0.00363	7.50%

Table B.27. New BOAS with 0.014 Inch Film-Cooling Holes (2A3515), Aft, 0<D<0.15 Inch Sand, 0.080 Grams, PR 1.6

Run #	P_{atm} (psia)	P_{0C} (psia)	PR	FF (lbm*√R/s/psia)	FF_0 (lbm*√R/s/psia)	%RFF
1	13.45	21.57	1.60	0.00268	0.00303	11.5%
2	13.45	21.60	1.61	0.00257	0.00304	15.4%
3	13.45	21.58	1.60	0.00261	0.00303	14.0%
Average	13.45	21.58	1.60	0.00262	0.00303	13.7%

Table B.28. New BOAS with 0.014 Inch Film-Cooling Holes (2A3515), Aft, 0<D<0.15 Inch Sand, 0.080 Grams, PR 1.8

Run #	P_{atm} (psia)	P_{0C} (psia)	PR	FF (lbm*√R/s/psia)	FF_0 (lbm*√R/s/psia)	%RFF
1	13.46	24.26	1.80	0.00339	0.00363	6.59%
2	13.46	24.28	1.80	0.00334	0.00363	8.14%
3	13.46	24.30	1.81	0.00325	0.00364	10.6%
Average	13.46	24.28	1.80	0.00333	0.00363	8.46%

Table B.29. BOAS with 0.019 Inch Film-Cooling Holes (2A3886), Forward, 0<D<0.15 Inch Sand, 0.25 Grams, PR 1.1

Run #	P_{atm} (psia)	P_{0C} (psia)	PR	FF (lbm*√R/s/psia)	FF_0 (lbm*√R/s/psia)	%RFF
1	13.65	15.14	1.11	0.00261	0.00325	19.5%
2	13.65	15.14	1.11	0.00258	0.00325	20.8%
3	13.65	15.16	1.11	0.00249	0.00327	23.7%
Average	13.65	15.15	1.11	0.00256	0.00326	21.3%

Table B.30. BOAS with 0.019 Inch Film-Cooling Holes (2A3886), Forward, 0<D<0.15 Inch Sand, 0.28 Grams, PR 1.3

Run #	P_{atm} (psia)	P_{0C} (psia)	PR	FF (lbm*√R/s/psia)	FF_0 (lbm*√R/s/psia)	%RFF
1	13.65	18.02	1.32	0.00473	0.00602	21.4%
2	13.65	18.07	1.32	0.00457	0.00606	24.6%
3	13.65	18.06	1.32	0.00460	0.00605	24.0%
Average	13.65	18.05	1.32	0.00463	0.00604	23.3%

Table B.31. BOAS with 0.019 Inch Film-Cooling Holes (2A3886), Forward, 0<D<0.15 Inch Sand, 0.42 Grams, PR 1.5

Run #	P_{atm} (psia)	P_{0C} (psia)	PR	FF (lbm*√R/s/psia)	FF_0 (lbm*√R/s/psia)	%RFF
1	13.64	20.97	1.54	0.00608	0.00819	25.8%
2	13.64	20.93	1.53	0.00617	0.00816	24.4%
3	13.64	20.90	1.53	0.00631	0.00814	22.6%
Average	13.64	20.94	1.53	0.00619	0.00817	24.2%

Table B.32. BOAS with 0.019 Inch Film-Cooling Holes (2A3886), Forward, 0<D<0.15 Inch Sand, 0.54 Grams, PR 1.7

Run #	P_{atm} (psia)	P_{0C} (psia)	PR	FF (lbm*√R/s/psia)	FF_0 (lbm*√R/s/psia)	%RFF
1	13.65	23.84	1.75	0.00747	0.01008	25.9%
2	13.65	23.80	1.74	0.00785	0.01006	22.0%
3	13.65	23.88	1.75	0.00768	0.01011	24.0%
Average	13.65	23.84	1.75	0.00767	0.01008	24.0%

Table B.33. Microcircuit Brick-and-Mortar, Forward, 0<D<0.15 Inch Sand, 0.25 Grams, PR 1.1

Run #	P_{atm} (psia)	P_{0C} (psia)	PR	FF (lbm*√R/s/psia)	FF_0 (lbm*√R/s/psia)	%RFF
1	13.78	15.23	1.11	0.00142	0.00190	24.8%
2	13.78	15.23	1.11	0.00141	0.00190	25.5%
3	13.78	15.21	1.10	0.00147	0.00188	21.8%
Average	13.78	15.22	1.10	0.00144	0.00189	24.0%

Table B.34. Microcircuit Brick-and-Mortar, Forward, 0<D<0.15 Inch Sand, 0.28 Grams, PR 1.3

Run #	P_{atm} (psia)	P_{0C} (psia)	PR	FF (lbm*√R/s/psia)	FF_0 (lbm*√R/s/psia)	%RFF
1	13.78	18.06	1.31	0.00296	0.00380	22.0%
2	13.78	18.06	1.31	0.00298	0.00380	21.6%
3	13.78	18.07	1.31	0.00285	0.00381	25.1%
Average	13.78	18.06	1.31	0.00293	0.00380	22.9%

Table B.35. Microcircuit Brick-and-Mortar, Forward, 0<D<0.15 Inch Sand, 0.42 Grams, PR 1.5

Run #	P_{atm} (psia)	P_{0C} (psia)	PR	FF (lbm*√R/s/psia)	FF_0 (lbm*√R/s/psia)	%RFF
1	13.79	20.90	1.52	0.00434	0.00537	19.2%
2	13.79	20.88	1.51	0.00437	0.00535	18.3%
3	13.79	20.87	1.51	0.00424	0.00535	20.7%
Average	13.79	20.88	1.51	0.00432	0.00536	19.4%

Table B.36. Microcircuit Brick-and-Mortar, Forward, 0<D<0.15 Inch Sand, 0.54 Grams, PR 1.7

Run #	P_{atm} (psia)	P_{0C} (psia)	PR	FF (lbm*√R/s/psia)	FF_0 (lbm*√R/s/psia)	%RFF
1	13.79	23.69	1.72	0.00550	0.00678	18.9%
2	13.79	23.69	1.72	0.00535	0.00678	21.0%
3	13.79	23.71	1.72	0.00539	0.00678	20.6%
Average	13.79	23.70	1.72	0.00541	0.00678	20.1%

Table B.37. Microcircuit Pedestal, Forward, 0<D<0.15 Inch Sand, 0.25 Grams, PR 1.1

Run #	P_{atm} (psia)	P_{0C} (psia)	PR	FF (lbm*√R/s/psia)	FF_0 (lbm*√R/s/psia)	%RFF
1	13.63	15.04	1.10	0.00188	0.00206	8.90%
2	13.63	15.04	1.10	0.00184	0.00206	10.7%
3	13.63	15.06	1.10	0.00180	0.00208	13.1%
Average	13.63	15.05	1.10	0.00184	0.00207	10.9%

Table B.38. Microcircuit Pedestal, Forward, 0<D<0.15 Inch Sand, 0.28 Grams, PR 1.3

Run #	P_{atm} (psia)	P_{0C} (psia)	PR	FF (lbm*√R/s/psia)	FF_0 (lbm*√R/s/psia)	%RFF
1	13.63	17.80	1.31	0.00338	0.00388	12.8%
2	13.63	17.81	1.31	0.00346	0.00388	10.9%
3	13.63	17.78	1.30	0.00354	0.00386	8.31%
Average	13.63	17.80	1.31	0.00346	0.00387	10.7%

Table B.39. Microcircuit Pedestal, Forward, 0<D<0.15 Inch Sand, 0.42 Grams, PR 1.5

Run #	P_{atm} (psia)	P_{0C} (psia)	PR	FF (lbm*√R/s/psia)	FF_0 (lbm*√R/s/psia)	%RFF
1	13.61	20.51	1.51	0.00476	0.00528	9.80%
2	13.61	20.52	1.51	0.00483	0.00529	8.62%
3	13.56	20.46	1.51	0.00476	0.00530	10.2%
Average	13.59	20.50	1.51	0.00478	0.00529	9.54%

Table B.40. Microcircuit Pedestal, Forward, 0<D<0.15 Inch Sand, 0.54 Grams, PR 1.7

Run #	P_{atm} (psia)	P_{0C} (psia)	PR	FFP (lbm*√R/s/psia)	FF_0 (lbm*√R/s/psia)	%RFF
1	13.59	23.23	1.71	0.00609	0.00658	7.39%
2	13.59	23.28	1.71	0.00591	0.00660	10.5%
3	13.59	23.32	1.72	0.00570	0.00662	14.0%
Average	13.59	23.28	1.71	0.00590	0.00660	10.6%

Table B.41. New BOAS with 0.014 Inch Film-Cooling Holes (2A3515), Forward, 0.0021<D<0.15 Inch Sand, 0.25 Grams, PR 1.1

Run #	P_{atm} (psia)	P_{0C} (psia)	PR	FF (lbm*√R/s/psia)	FF_0 (lbm*√R/s/psia)	%RFF
1	13.52	15.00	1.11	0.00155	0.00224	30.8%
2	13.52	15.02	1.11	0.00144	0.00225	36.1%
3	13.52	15.02	1.11	0.00139	0.00225	38.3%
Average	13.52	15.01	1.11	0.00146	0.00225	35.0%

Table B.42. New BOAS with 0.014 Inch Film-Cooling Holes (2A3515), Forward, 0.0021<D<0.15 Inch Sand, 0.28 Grams, PR 1.3

Run #	P_{atm} (psia)	P_{0C} (psia)	PR	FF (lbm*√R/s/psia)	FF_0 (lbm*√R/s/psia)	%RFF
1	13.52	17.88	1.32	0.00263	0.00411	36.0%
2	13.52	17.87	1.32	0.00270	0.00410	34.2%
3	13.52	17.87	1.32	0.00263	0.00410	35.8%
Average	13.52	17.87	1.32	0.00265	0.00410	35.3%

Table B.43. New BOAS with 0.014 Inch Film-Cooling Holes (2A3515), Forward, 0.0021<D<0.15 Inch Sand, 0.42 Grams, PR 1.5

Run #	P_{atm} (psia)	P_{0C} (psia)	PR	FF (lbm*√R/s/psia)	FF_0 (lbm*√R/s/psia)	%RFF
1	13.51	20.77	1.54	0.00355	0.00552	35.7%
2	13.51	20.70	1.53	0.00380	0.00549	30.8%
3	13.51	20.75	1.54	0.00355	0.00551	35.6%
Average	13.51	20.74	1.53	0.00363	0.00550	34.0%

Table B.44. New BOAS with 0.014 Inch Film-Cooling Holes (2A3515), Forward, 0.0021<D<0.15 Inch Sand, 0.54 Grams, PR 1.7

Run #	P_{atm} (psia)	P_{0C} (psia)	PR	FF (lbm*√R/s/psia)	FF_0 (lbm*√R/s/psia)	%RFF
1	13.57	23.53	1.73	0.00429	0.00663	35.3%
2	13.57	23.52	1.73	0.00439	0.00662	33.7%
3	13.57	23.46	1.73	0.00476	0.00660	27.8%
Average	13.57	23.50	1.73	0.00448	0.00662	32.3%

Table B.45. BOAS with 0.019 Inch Film-Cooling Holes (2A3886), Forward, 0.0021<D<0.15 Inch Sand, 0.25 Grams, PR 1.1

Run #	P_{atm} (psia)	P_{0C} (psia)	PR	FF (lbm*√R/s/psia)	FF_0 (lbm*√R/s/psia)	%RFF
1	13.67	15.26	1.12	0.00210	0.00336	37.4%
2	13.67	15.28	1.12	0.00202	0.00339	40.3%
3	13.67	15.26	1.12	0.00208	0.00336	38.0%
Average	13.67	15.26	1.12	0.00207	0.00337	38.6%

Table B.46. BOAS with 0.019 Inch Film-Cooling Holes (2A3886), Forward, 0.0021<D<0.15 Inch Sand, 0.28 Grams, PR 1.3

Run #	P_{atm} (psia)	P_{0C} (psia)	PR	FF (lbm*√R/s/psia)	FF_0 (lbm*√R/s/psia)	%RFF
1	13.67	18.26	1.34	0.00381	0.00619	38.5%
2	13.67	18.24	1.33	0.00393	0.00617	36.4%
3	13.67	18.28	1.34	0.00380	0.00621	38.8%
Average	13.67	18.26	1.34	0.00385	0.00619	37.9%

Table B.47. BOAS with 0.019 Inch Film-Cooling Holes (2A3886), Forward, 0.0021<D<0.15 Inch Sand, 0.42 Grams, PR 1.5

Run #	P_{atm} (psia)	P_{0C} (psia)	PR	FF (lbm*√R/s/psia)	FF_0 (lbm*√R/s/psia)	%RFF
1	13.69	21.29	1.56	0.00500	0.00835	40.2%
2	13.66	21.18	1.55	0.00528	0.00830	36.4%
3	13.66	21.20	1.55	0.00509	0.00832	38.9%
Average	13.67	21.23	1.55	0.00512	0.00833	38.5%

Table B.48. BOAS with 0.019 Inch Film-Cooling Holes (2A3886), Forward, 0.0021<D<0.15 Inch Sand, 0.54 Grams, PR 1.7

Run #	P_{atm} (psia)	P_{0C} (psia)	PR	FF (lbm*√R/s/psia)	FF_0 (lbm*√R/s/psia)	%RFF
1	13.69	24.34	1.78	0.00596	0.01039	42.6%
2	13.69	24.31	1.78	0.00598	0.01036	42.3%
3	13.69	24.09	1.76	0.00697	0.01021	31.7%
Average	13.69	24.24	1.77	0.00631	0.01032	38.9%

Table B.49. Microcircuit Brick-and-Mortar, Forward, 0.0021<D<0.15 Inch Sand, 0.25 Grams, PR 1.1

Run #	P_{atm} (psia)	P_{0C} (psia)	PR	FF (lbm*√R/s/psia)	FF_0 (lbm*√R/s/psia)	%RFF
1	13.58	15.05	1.11	0.00119	0.00192	37.9%
2	13.58	15.08	1.11	0.00110	0.00194	43.2%
3	13.58	15.06	1.11	0.00119	0.00193	38.3%
Average	13.58	15.06	1.11	0.00116	0.00193	39.8%

Table B.50. Microcircuit Brick-and-Mortar, Forward, 0.0021<D<0.15 Inch Sand, 0.28 Grams, PR 1.3

Run #	P_{atm} (psia)	P_{0C} (psia)	PR	FF (lbm*√R/s/psia)	FF_0 (lbm*√R/s/psia)	%RFF
1	13.58	17.88	1.32	0.00265	0.00384	31.1%
2	13.58	17.92	1.32	0.00224	0.00387	42.1%
3	13.58	17.90	1.32	0.00245	0.00386	36.6%
Average	13.58	17.90	1.32	0.00245	0.00386	36.6%

Table B.51. Microcircuit Brick-and-Mortar, Forward, 0.0021<D<0.15 Inch Sand, 0.42 Grams, PR 1.5

Run #	P_{atm} (psia)	P_{0C} (psia)	PR	FF (lbm*√R/s/psia)	FF_0 (lbm*√R/s/psia)	%RFF
1	13.64	20.81	1.53	0.00347	0.00543	36.1%
2	13.64	20.82	1.53	0.00351	0.00544	35.4%
3	13.64	20.81	1.53	0.00354	0.00543	34.8%
Average	13.64	20.81	1.53	0.00351	0.00543	35.5%

Table B.52. Microcircuit Brick-and-Mortar, Forward, 0.0021<D<0.15 Inch Sand, 0.54 Grams, PR 1.7

Run #	P_{atm} (psia)	P_{0C} (psia)	PR	FF (lbm*√R/s/psia)	FF_0 (lbm*√R/s/psia)	%RFF
1	13.64	23.74	1.74	0.00457	0.00694	34.1%
2	13.64	23.77	1.74	0.00452	0.00695	34.9%
3	13.64	23.72	1.74	0.00478	0.00693	30.9%
Average	13.64	23.74	1.74	0.00463	0.00694	33.3%

Table B.53. Microcircuit Pedestal, Forward, 0.0021<D<0.15 Inch Sand, 0.25 Grams, PR 1.1

Run #	P_{atm} (psia)	P_{0C} (psia)	PR	FF (lbm*√R/s/psia)	FF_0 (lbm*√R/s/psia)	%RFF
1	13.50	14.95	1.11	0.00148	0.00211	29.7%
2	13.50	15.00	1.11	0.00138	0.00214	35.5%
3	13.50	15.00	1.11	0.00134	0.00214	37.3%
Average	13.50	14.98	1.11	0.00140	0.00213	34.2%

Table B.54. Microcircuit Pedestal, Forward, 0.0021<D<0.15 Inch Sand, 0.28 Grams, PR 1.3

Run #	P_{atm} (psia)	P_{0C} (psia)	PR	FF (lbm*√R/s/psia)	FF_0 (lbm*√R/s/psia)	%RFF
1	13.51	17.86	1.32	0.00251	0.00400	37.1%
2	13.51	17.88	1.32	0.00270	0.00401	32.6%
3	13.51	17.90	1.33	0.00254	0.00402	36.9%
Average	13.51	17.88	1.32	0.00258	0.00401	35.5%

Table B.55. Microcircuit Pedestal, Forward, 0.0021<D<0.15 Inch Sand, 0.42 Grams, PR 1.5

Run #	P_{atm} (psia)	P_{0C} (psia)	PR	FF (lbm*√R/s/psia)	FF_0 (lbm*√R/s/psia)	%RFF
1	13.57	20.67	1.52	0.00377	0.00539	30.0%
2	13.57	20.63	1.52	0.00405	0.00537	24.6%
3	13.57	20.70	1.53	0.00368	0.00540	31.8%
Average	13.57	20.67	1.52	0.00384	0.00539	28.8%

Table B.56. Microcircuit Pedestal, Forward, 0.0021<D<0.15 Inch Sand, 0.54 Grams, PR 1.7

Run #	P_{atm} (psia)	P_{0C} (psia)	PR	FF (lbm*√R/s/psia)	FF_0 (lbm*√R/s/psia)	%RFF
1	13.60	23.55	1.73	0.00485	0.00673	27.9%
2	13.60	23.64	1.74	0.00468	0.00677	30.9%
3	13.60	23.65	1.74	0.00462	0.00678	31.8%
Average	13.60	23.61	1.74	0.00472	0.00676	30.2%

Table B.57. New BOAS with 0.014 Inch Film-Cooling Holes (2A3515), Forward, 0.0030<D<0.15 Inch Sand, 0.25 Grams, PR 1.1

Run #	P_{atm} (psia)	P_{0C} (psia)	PR	FF (lbm*√R/s/psia)	FF_0 (lbm*√R/s/psia)	%RFF
1	13.76	15.32	1.11	0.00123	0.00228	46.2%
2	13.76	15.28	1.11	0.00140	0.00225	38.0%
3	13.76	15.28	1.11	0.00139	0.00225	38.4%
Average	13.76	15.29	1.11	0.00134	0.00226	40.9%

Table B.58. New BOAS with 0.014 Inch Film-Cooling Holes (2A3515), Forward, 0.0030<D<0.15 Inch Sand, 0.28 Grams, PR 1.3

Run #	P_{atm} (psia)	P_{0C} (psia)	PR	FF (lbm*√R/s/psia)	FF_0 (lbm*√R/s/psia)	%RFF
1	13.74	18.14	1.32	0.00268	0.00409	34.5%
2	13.74	18.23	1.33	0.00235	0.00413	43.2%
3	13.74	18.16	1.32	0.00254	0.00410	38.0%
Average	13.74	18.18	1.32	0.00252	0.00411	38.6%

Table B.59. New BOAS with 0.014 Inch Film-Cooling Holes (2A3515), Forward, 0.0030<D<0.15 Inch Sand, 0.42 Grams, PR 1.5

Run #	P_{atm} (psia)	P_{0C} (psia)	PR	FF (lbm*√R/s/psia)	FF_0 (lbm*√R/s/psia)	%RFF
1	13.74	21.04	1.53	0.00336	0.00549	38.7%
2	13.74	21.00	1.53	0.00342	0.00547	37.6%
3	13.74	21.04	1.53	0.00342	0.00549	37.6%
Average	13.74	21.03	1.53	0.00340	0.00548	38.0%

Table B.60. New BOAS with 0.014 Inch Film-Cooling Holes (2A3515), Forward, 0.0030<D<0.15 Inch Sand, 0.54 Grams, PR 1.7

Run #	P_{atm} (psia)	P_{0C} (psia)	PR	FF (lbm*√R/s/psia)	FF_0 (lbm*√R/s/psia)	%RFF
1	13.74	23.86	1.74	0.00408	0.00664	38.5%
2	13.74	23.81	1.73	0.00431	0.00662	35.0%
3	13.74	23.89	1.74	0.00411	0.00665	38.2%
Average	13.74	23.85	1.74	0.00417	0.00664	37.2%

Table B.61. BOAS with 0.019 Inch Film-Cooling Holes (2A3886), Forward, 0.0030<D<0.15 Inch Sand, 0.25 Grams, PR 1.1

Run #	P_{atm} (psia)	P_{0C} (psia)	PR	FF (lbm*√R/s/psia)	FF_0 (lbm*√R/s/psia)	%RFF
1	13.77	15.45	1.12	0.00188	0.00345	45.4%
2	13.77	15.41	1.12	0.00181	0.00341	46.8%
3	13.77	15.41	1.12	0.00185	0.00341	45.7%
Average	13.77	15.42	1.12	0.00185	0.00342	46.0%

Table B.62. BOAS with 0.019 Inch Film-Cooling Holes (2A3886), Forward, 0.0030<D<0.15 Inch Sand, 0.28 Grams, PR 1.3

Run #	P_{atm} (psia)	P_{0C} (psia)	PR	FF (lbm*√R/s/psia)	FF_0 (lbm*√R/s/psia)	%RFF
1	13.76	18.48	1.34	0.00339	0.00627	45.9%
2	13.76	18.46	1.34	0.00369	0.00625	40.9%
3	13.76	18.48	1.34	0.00363	0.00626	42.0%
Average	13.76	18.47	1.34	0.00357	0.00626	42.9%

Table B.63. BOAS with 0.019 Inch Film-Cooling Holes (2A3886), Forward, 0.0030<D<0.15 Inch Sand, 0.42 Grams, PR 1.5

Run #	P_{atm} (psia)	P_{0C} (psia)	PR	FF (lbm*√R/s/psia)	FF_0 (lbm*√R/s/psia)	%RFF
1	13.76	21.38	1.55	0.00506	0.00834	39.3%
2	13.76	21.48	1.56	0.00455	0.00840	45.8%
3	13.76	21.39	1.55	0.00504	0.00835	39.7%
Average	13.76	21.42	1.56	0.00488	0.00836	41.6%

Table B.64. BOAS with 0.019 Inch Film-Cooling Holes (2A3886), Forward, 0.0030<D<0.15 Inch Sand, 0.54 Grams, PR 1.7

Run #	P_{atm} (psia)	P_{0C} (psia)	PR	FF (lbm*√R/s/psia)	FF_0 (lbm*√R/s/psia)	%RFF
1	13.76	24.35	1.77	0.00615	0.01030	40.3%
2	13.76	24.31	1.77	0.00610	0.01027	40.6%
3	13.76	24.33	1.77	0.00594	0.01029	42.3%
Average	13.76	24.33	1.77	0.00606	0.01029	41.1%

Table B.65. Microcircuit Brick-and-Mortar, Forward, 0.0030<D<0.15 Inch Sand, 0.25 Grams, PR 1.1

Run #	P_{atm} (psia)	P_{0C} (psia)	PR	FF (lbm*√R/s/psia)	FF_0 (lbm*√R/s/psia)	%RFF
1	13.62	15.10	1.11	0.00110	0.00193	43.0%
2	13.62	15.10	1.11	0.00109	0.00193	43.2%
3	13.62	15.13	1.11	0.00107	0.00195	45.0%
Average	13.62	15.11	1.11	0.00109	0.00194	43.8%

Table B.66. Microcircuit Brick-and-Mortar, Forward, 0.0030<D<0.15 Inch Sand, 0.28 Grams, PR 1.3

Run #	P_{atm} (psia)	P_{0C} (psia)	PR	FF (lbm*√R/s/psia)	FF_0 (lbm*√R/s/psia)	%RFF
1	13.59	17.91	1.32	0.00231	0.00386	40.2%
2	13.59	17.97	1.32	0.00214	0.00390	45.0%
3	13.59	17.98	1.32	0.00215	0.00391	44.9%
Average	13.59	17.95	1.32	0.00220	0.00389	43.3%

Table B.67. Microcircuit Brick-and-Mortar, Forward, 0.0030<D<0.15 Inch Sand, 0.42 Grams, PR 1.5

Run #	P_{atm} (psia)	P_{0C} (psia)	PR	FF (lbm*√R/s/psia)	FF_0 (lbm*√R/s/psia)	%RFF
1	13.59	20.81	1.53	0.00308	0.00547	43.7%
2	13.59	20.81	1.53	0.00298	0.00547	45.5%
3	13.59	20.77	1.53	0.00327	0.00545	40.0%
Average	13.59	20.80	1.53	0.00311	0.00546	43.1%

Table B.68. Microcircuit Brick-and-Mortar, Forward, 0.0030<D<0.15 Inch Sand, 0.54 Grams, PR 1.7

Run #	P_{atm} (psia)	P_{0C} (psia)	PR	FF (lbm*√R/s/psia)	FF_0 (lbm*√R/s/psia)	%RFF
1	13.60	23.71	1.74	0.00389	0.00696	44.2%
2	13.60	23.69	1.74	0.00416	0.00695	40.2%
3	13.60	23.60	1.74	0.00406	0.00690	41.1%
Average	13.60	23.67	1.74	0.00404	0.00694	41.8%

Table B.69. Microcircuit Pedestal, Forward, 0.0030<D<0.15 Inch Sand, 0.25 Grams, PR 1.1

Run #	P_{atm} (psia)	P_{0C} (psia)	PR	FF (lbm*√R/s/psia)	FF_0 (lbm*√R/s/psia)	%RFF
1	13.47	14.96	1.11	0.00116	0.00214	45.9%
2	13.47	14.92	1.11	0.00139	0.00211	34.1%
3	13.47	14.95	1.11	0.00130	0.00213	39.3%
Average	13.47	14.94	1.11	0.00128	0.00213	39.8%

Table B.70. Microcircuit Pedestal, Forward, 0.0030<D<0.15 Inch Sand, 0.28 Grams, PR 1.3

Run #	P_{atm} (psia)	P_{0C} (psia)	PR	FF (lbm*√R/s/psia)	FF_0 (lbm*√R/s/psia)	%RFF
1	13.47	17.82	1.32	0.00234	0.00401	41.7%
2	13.47	17.82	1.32	0.00231	0.00401	42.4%
3	13.47	17.74	1.32	0.00259	0.00396	34.5%
Average	13.47	17.79	1.32	0.00241	0.00399	39.5%

Table B.71. Microcircuit Pedestal, Forward, 0.0030<D<0.15 Inch Sand, 0.42 Grams, PR 1.5

Run #	P_{atm} (psia)	P_{0C} (psia)	PR	FF (lbm*√R/s/psia)	FF_0 (lbm*√R/s/psia)	%RFF
1	13.47	20.60	1.53	0.00351	0.00542	35.4%
2	13.47	20.68	1.54	0.00303	0.00546	44.5%
3	13.47	20.64	1.53	0.00330	0.00544	39.3%
Average	13.47	20.64	1.53	0.00328	0.00544	39.7%

Table B.72. Microcircuit Pedestal, Forward, 0.0030<D<0.15 Inch Sand, 0.54 Grams, PR 1.7

Run #	P_{atm} (psia)	P_{0C} (psia)	PR	FF (lbm*√R/s/psia)	FF_0 (lbm*√R/s/psia)	%RFF
1	13.49	23.42	1.74	0.00390	0.00676	42.3%
2	13.49	23.51	1.74	0.00446	0.00680	34.5%
3	13.49	23.37	1.73	0.00421	0.00673	37.5%
Average	13.49	23.43	1.74	0.00419	0.00676	38.1%

Table B.73. New BOAS with 0.014 Inch Film-Cooling Holes (2A3515), Forward, 0.0059<D<0.15 Inch Sand, 0.25 Grams, PR 1.1

Run #	P_{atm} (psia)	P_{0C} (psia)	PR	FF (lbm*√R/s/psia)	FF_0 (lbm*√R/s/psia)	%RFF
1	13.74	15.28	1.11	0.00122	0.00226	45.9%
2	13.74	15.32	1.12	0.00126	0.00229	45.1%
3	13.74	15.26	1.11	0.00124	0.00225	44.8%
Average	13.74	15.29	1.11	0.00124	0.00227	45.3%

Table B.74. New BOAS with 0.014 Inch Film-Cooling Holes (2A3515), Forward, 0.0059<D<0.15 Inch Sand, 0.28 Grams, PR 1.3

Run #	P_{atm} (psia)	P_{0C} (psia)	PR	FF (lbm*√R/s/psia)	FF_0 (lbm*√R/s/psia)	%RFF
1	13.74	18.22	1.33	0.00236	0.00413	43.0%
2	13.74	18.20	1.32	0.00219	0.00412	46.8%
3	13.74	18.17	1.32	0.00253	0.00410	38.4%
Average	13.74	18.20	1.32	0.00236	0.00412	42.7%

Table B.75. New BOAS with 0.014 Inch Film-Cooling Holes (2A3515), Forward, 0.0059<D<0.15 Inch Sand, 0.42 Grams, PR 1.5

Run #	P_{atm} (psia)	P_{0C} (psia)	PR	FF (lbm*√R/s/psia)	FF_0 (lbm*√R/s/psia)	%RFF
1	13.75	21.05	1.53	0.00326	0.00548	40.5%
2	13.75	21.07	1.53	0.00323	0.00549	41.2%
3	13.75	21.07	1.53	0.00329	0.00549	40.1%
Average	13.75	21.07	1.53	0.00326	0.00549	40.6%

Table B.76. New BOAS with 0.014 Inch Film-Cooling Holes (2A3515), Forward, 0.0059<D<0.15 Inch Sand, 0.54 Grams, PR 1.7

Run #	P_{atm} (psia)	P_{0C} (psia)	PR	FF (lbm*√R/s/psia)	FF_0 (lbm*√R/s/psia)	%RFF
1	13.57	23.74	1.75	0.00390	0.00671	41.9%
2	13.57	23.75	1.75	0.00391	0.00671	41.8%
3	13.57	23.65	1.74	0.00414	0.00667	37.9%
Average	13.57	23.71	1.75	0.00398	0.00670	40.5%

Table B.77. BOAS with 0.019 Inch Film-Cooling Holes (2A3886), Forward, 0.0059<D<0.15 Inch Sand, 0.25 Grams, PR 1.1

Run #	P_{atm} (psia)	P_{0C} (psia)	PR	FF (lbm*√R/s/psia)	FF_0 (lbm*√R/s/psia)	%RFF
1	13.77	15.38	1.12	0.00187	0.00337	44.4%
2	13.77	15.44	1.12	0.00172	0.00343	50.0%
3	13.77	15.44	1.12	0.00158	0.00343	53.9%
Average	13.77	15.42	1.12	0.00173	0.00341	49.4%

Table B.78. BOAS with 0.019 Inch Film-Cooling Holes (2A3886), Forward, 0.0059<D<0.15 Inch Sand, 0.28 Grams, PR 1.3

Run #	P_{atm} (psia)	P_{0C} (psia)	PR	FF (lbm*√R/s/psia)	FF_0 (lbm*√R/s/psia)	%RFF
1	13.77	18.47	1.34	0.00350	0.00625	44.0%
2	13.77	18.49	1.34	0.00333	0.00626	46.8%
3	13.77	18.50	1.34	0.00320	0.00627	48.9%
Average	13.77	18.49	1.34	0.00335	0.00626	46.6%

Table B.79. BOAS with 0.019 Inch Film-Cooling Holes (2A3886), Forward, 0.0059<D<0.15 Inch Sand, 0.42 Grams, PR 1.5

Run #	P_{atm} (psia)	P_{0C} (psia)	PR	FF (lbm*√R/s/psia)	FF_0 (lbm*√R/s/psia)	%RFF
1	13.77	21.52	1.56	0.00428	0.00842	49.2%
2	13.77	21.54	1.56	0.00440	0.00843	47.8%
3	13.77	21.44	1.56	0.00477	0.00837	43.0%
Average	13.77	21.50	1.56	0.00448	0.00841	46.7%

Table B.80. BOAS with 0.019 Inch Film-Cooling Holes (2A3886), Forward, 0.0059<D<0.15 Inch Sand, 0.54 Grams, PR 1.7

Run #	P_{atm} (psia)	P_{0C} (psia)	PR	FF (lbm*√R/s/psia)	FF_0 (lbm*√R/s/psia)	%RFF
1	13.77	24.46	1.78	0.00570	0.01037	45.1%
2	13.77	24.48	1.78	0.00558	0.01038	46.2%
3	13.77	24.54	1.78	0.00522	0.01042	49.9%
Average	13.77	24.49	1.78	0.00550	0.01039	47.1%

Table B.81. Microcircuit Brick-and-Mortar, Forward, 0.0059<D<0.15 Inch Sand, 0.25 Grams, PR 1.1

Run #	P_{atm} (psia)	P_{0C} (psia)	PR	FF (lbm*√R/s/psia)	FF_0 (lbm*√R/s/psia)	%RFF
1	13.58	15.10	1.11	0.00090	0.00197	54.1%
2	13.58	15.09	1.11	0.00095	0.00196	51.3%
3	13.58	15.06	1.11	0.00113	0.00193	41.8%
Average	13.58	15.08	1.11	0.00099	0.00195	49.0%

Table B.82. Microcircuit Brick-and-Mortar, Forward, 0.0059<D<0.15 Inch Sand, 0.28 Grams, PR 1.3

Run #	P_{atm} (psia)	P_{0C} (psia)	PR	FF (lbm*√R/s/psia)	FF_0 (lbm*√R/s/psia)	%RFF
1	13.59	17.98	1.32	0.00181	0.00391	53.6%
2	13.59	17.98	1.32	0.00220	0.00391	43.8%
3	13.59	18.02	1.33	0.00193	0.00393	51.0%
Average	13.59	18.00	1.32	0.00198	0.00391	49.4%

Table B.83. Microcircuit Brick-and-Mortar, Forward, 0.0059<D<0.15 Inch Sand, 0.42 Grams, PR 1.5

Run #	P_{atm} (psia)	P_{0C} (psia)	PR	FF (lbm*√R/s/psia)	FF_0 (lbm*√R/s/psia)	%RFF
1	13.64	20.89	1.53	0.00308	0.00547	43.7%
2	13.64	20.89	1.53	0.00302	0.00548	44.8%
3	13.64	20.92	1.53	0.00283	0.00549	48.5%
Average	13.64	20.90	1.53	0.00298	0.00548	45.7%

Table B.84. Microcircuit Brick-and-Mortar, Forward, 0.0059<D<0.15 Inch Sand, 0.54 Grams, PR 1.7

Run #	P_{atm} (psia)	P_{0C} (psia)	PR	FF (lbm*√R/s/psia)	FF_0 (lbm*√R/s/psia)	%RFF
1	13.64	23.78	1.74	0.00389	0.00696	44.1%
2	13.64	23.93	1.76	0.00343	0.00704	51.3%
3	13.64	23.85	1.75	0.00398	0.00699	43.1%
Average	13.64	23.85	1.75	0.00377	0.00700	46.2%

Table B.85. Microcircuit Pedestal, Forward, 0.0059<D<0.15 Inch Sand, 0.25 Grams, PR 1.1

Run #	P_{atm} (psia)	P_{0C} (psia)	PR	FF (lbm*√R/s/psia)	FF_0 (lbm*√R/s/psia)	%RFF
1	13.49	15.00	1.11	0.00121	0.00215	43.8%
2	13.49	14.99	1.11	0.00114	0.00214	46.7%
3	13.49	15.01	1.11	0.00107	0.00216	50.3%
Average	13.49	15.00	1.11	0.00114	0.00215	47.0%

Table B.86. Microcircuit Pedestal, Forward, 0.0059<D<0.15 Inch Sand, 0.28 Grams, PR 1.3

Run #	P_{atm} (psia)	P_{0C} (psia)	PR	FF (lbm*√R/s/psia)	FF_0 (lbm*√R/s/psia)	%RFF
1	13.55	17.90	1.32	0.00220	0.00399	44.9%
2	13.55	17.93	1.32	0.00255	0.00400	36.4%
3	13.55	17.89	1.32	0.00227	0.00398	43.0%
Average	13.55	17.91	1.32	0.00234	0.00399	41.4%

Table B.87. Microcircuit Pedestal, Forward, 0.0059<D<0.15 Inch Sand, 0.42 Grams, PR 1.5

Run #	P_{atm} (psia)	P_{0C} (psia)	PR	FF (lbm*√R/s/psia)	FF_0 (lbm*√R/s/psia)	%RFF
1	13.55	20.74	1.53	0.00314	0.00543	42.2%
2	13.55	20.80	1.54	0.00297	0.00546	45.7%
3	13.55	20.74	1.53	0.00306	0.00543	43.6%
Average	13.55	20.76	1.53	0.00306	0.00544	43.8%

Table B.88. Microcircuit Pedestal, Forward, 0.0059<D<0.15 Inch Sand, 0.54 Grams, PR 1.7

Run #	P_{atm} (psia)	P_{0C} (psia)	PR	FF (lbm*√R/s/psia)	FF_0 (lbm*√R/s/psia)	%RFF
1	13.60	23.75	1.75	0.00412	0.00683	39.6%
2	13.60	23.76	1.75	0.00364	0.00684	46.7%
3	13.60	23.76	1.75	0.00407	0.00683	40.5%
Average	13.60	23.76	1.75	0.00394	0.00683	42.3%

Table B.89. BOAS with 0.019 Inch Film-Cooling Holes (2A3886), Aft, 0<D<0.15 Inch Sand, 0.010 Grams, PR 1.2

Run #	P_{atm} (psia)	P_{0C} (psia)	PR	FF (lbm*√R/s/psia)	FF_0 (lbm*√R/s/psia)	%RFF
1	13.73	16.48	1.20	0.00213	0.00219	2.60%
2	13.73	16.48	1.20	0.00213	0.00219	2.69%
3	13.73	16.51	1.20	0.00208	0.00220	5.31%
Average	13.73	16.49	1.20	0.00211	0.00219	3.53%

Table B.90. BOAS with 0.019 Inch Film-Cooling Holes (2A3886), Aft, 0<D<0.15 Inch Sand, 0.020 Grams, PR 1.4

Run #	P_{atm} (psia)	P_{0C} (psia)	PR	FF (lbm*√R/s/psia)	FF_0 (lbm*√R/s/psia)	%RFF
1	13.65	19.12	1.40	0.00321	0.00328	2.06%
2	13.65	19.12	1.40	0.00313	0.00328	4.52%
3	13.65	19.12	1.40	0.00313	0.00328	4.54%
Average	13.65	19.12	1.40	0.00315	0.00328	3.71%

Table B.91. BOAS with 0.019 Inch Film-Cooling Holes (2A3886), Aft, 0<D<0.15 Inch Sand, 0.040 Grams, PR 1.6

Run #	P_{atm} (psia)	P_{0C} (psia)	PR	FF (lbm*√R/s/psia)	FF_0 (lbm*√R/s/psia)	%RFF
1	13.66	21.88	1.60	0.00411	0.00422	2.49%
2	13.66	21.91	1.60	0.00391	0.00423	7.62%
3	13.66	21.88	1.60	0.00402	0.00422	4.86%
Average	13.66	21.89	1.60	0.00401	0.00422	4.99%

Table B.92. BOAS with 0.019 Inch Film-Cooling Holes (2A3886), Aft, 0<D<0.15 Inch Sand, 0.060 Grams, PR 1.8

Run #	P_{atm} (psia)	P_{0C} (psia)	PR	FF (lbm*√R/s/psia)	FF_0 (lbm*√R/s/psia)	%RFF
1	13.69	24.73	1.81	0.00462	0.00511	9.62%
2	13.67	24.63	1.80	0.00491	0.00509	3.47%
3	13.67	24.66	1.80	0.00484	0.00510	4.96%
Average	13.68	24.67	1.80	0.00479	0.00510	6.02%

Table B.93. Microcircuit Brick-and-Mortar, Aft, 0<D<0.15 Inch Sand, 0.010 Grams, PR 1.2

Run #	P_{atm} (psia)	P_{0C} (psia)	PR	FF (lbm*√R/s/psia)	FF_0 (lbm*√R/s/psia)	%RFF
1	13.74	16.49	1.20	0.00142	0.00150	5.53%
2	13.74	16.49	1.20	0.00142	0.00150	5.19%
3	13.74	16.50	1.20	0.00139	0.00150	7.64%
Average	13.74	16.49	1.20	0.00141	0.00150	6.12%

Table B.94. Microcircuit Brick-and-Mortar, Aft, 0<D<0.15 Inch Sand, 0.020 Grams, PR 1.4

Run #	P_{atm} (psia)	P_{0C} (psia)	PR	FF (lbm*√R/s/psia)	FF_0 (lbm*√R/s/psia)	%RFF
1	13.74	19.24	1.40	0.00220	0.00234	5.98%
2	13.74	19.24	1.40	0.00218	0.00234	6.84%
3	13.74	19.24	1.40	0.00221	0.00234	5.41%
Average	13.74	19.24	1.40	0.00220	0.00234	6.07%

Table B.95. Microcircuit Brick-and-Mortar, Aft, 0<D<0.15 Inch Sand, 0.040 Grams, PR 1.6

Run #	P_{atm} (psia)	P_{0C} (psia)	PR	FF (lbm*√R/s/psia)	FF_0 (lbm*√R/s/psia)	%RFF
1	13.74	22.01	1.60	0.00291	0.00309	5.71%
2	13.74	22.03	1.60	0.00282	0.00309	8.70%
3	13.74	22.02	1.60	0.00283	0.00309	8.42%
Average	13.74	22.02	1.60	0.00285	0.00309	7.61%

Table B.96. Microcircuit Brick-and-Mortar, Aft, 0<D<0.15 Inch Sand, 0.060 Grams, PR 1.8

Run #	P_{atm} (psia)	P_{0C} (psia)	PR	FF (lbm*√R/s/psia)	FF_0 (lbm*√R/s/psia)	%RFF
1	13.74	24.79	1.80	0.00339	0.00380	10.7%
2	13.74	24.80	1.80	0.00341	0.00380	10.3%
3	13.59	24.53	1.80	0.00347	0.00381	8.78%
Average	13.69	24.70	1.80	0.00343	0.00380	9.92%

Table B.97. Microcircuit Pedestal, Aft, 0<D<0.15 Inch Sand, 0.010 Grams, PR 1.2

Run #	P_{atm} (psia)	P_{0C} (psia)	PR	FF (lbm*√R/s/psia)	FF_0 (lbm*√R/s/psia)	%RFF
1	13.78	16.53	1.20	0.00148	0.00153	3.30%
2	13.78	16.53	1.20	0.00150	0.00153	1.91%
3	13.78	16.54	1.20	0.00149	0.00153	2.20%
Average	13.78	16.54	1.20	0.00149	0.00153	2.47%

Table B.98. Microcircuit Pedestal, Aft, 0<D<0.15 Inch Sand, 0.020 Grams, PR 1.4

Run #	P_{atm} (psia)	P_{0C} (psia)	PR	FF (lbm*√R/s/psia)	FF_0 (lbm*√R/s/psia)	%RFF
1	13.78	19.29	1.40	0.00222	0.00230	3.64%
2	13.78	19.32	1.40	0.00227	0.00231	1.70%
3	13.78	19.30	1.40	0.00219	0.00230	4.74%
Average	13.78	19.30	1.40	0.00223	0.00230	3.36%

Table B.99. Microcircuit Pedestal, Aft, 0<D<0.15 Inch Sand, 0.040 Grams, PR 1.6

Run #	P_{atm} (psia)	P_{0C} (psia)	PR	FF (lbm*√R/s/psia)	FF_0 (lbm*√R/s/psia)	%RFF
1	13.78	22.07	1.60	0.00282	0.00297	5.06%
2	13.78	22.06	1.60	0.00281	0.00297	5.13%
3	13.78	22.06	1.60	0.00289	0.00297	2.72%
Average	13.78	22.06	1.60	0.00284	0.00297	4.30%

Table B.100. Microcircuit Pedestal, Aft, 0<D<0.15 Inch Sand, 0.060 Grams, PR 1.8

Run #	P_{atm} (psia)	P_{0C} (psia)	PR	FF (lbm*√R/s/psia)	FF_0 (lbm*√R/s/psia)	%RFF
1	13.77	24.80	1.80	0.00346	0.00358	3.24%
2	13.77	24.82	1.80	0.00339	0.00358	5.26%
3	13.59	24.51	1.80	0.00336	0.00358	6.22%
Average	13.71	24.71	1.80	0.00340	0.00358	4.91%